High Energy and Power Density Nanotube-Enhanced Ultracapacitor Design, Modeling, Testing, and Predicted Performance
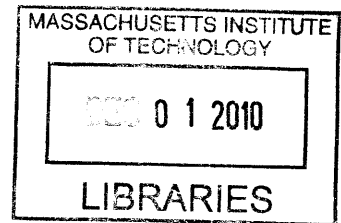
by

Riccardo Signorelli

Submitted to the Department of Electrical Engineering and Computer Science
in partial fulfillment of the requirements for the degree of

Doctor of Philosophy
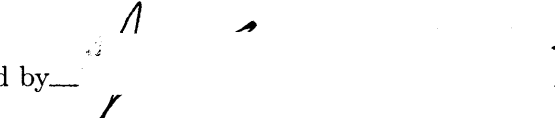
at the

MASSACHUSETTS INSTITUTE OF TECHNOLOGY

June 2009

Author_____
Department of Electrical Engineering and Computer Science
May 20, 2009

Certified by____
Joel Schindall
Bernard M. Gordon Professor of the Practice
Thesis Supervisor

Certified by____
John Kassakian
Professor of Electrical Engineering
Thesis Supervisor

Accepted by___
Terry P. Orlando
Chairman, Department Committee on Graduate Students

High Energy and Power Density Nanotube-Enhanced Ultracapacitor Design, Modeling, Testing, and Predicted Performance

by

Riccardo Signorelli

Abstract

Today's batteries are penalized by their poor cycleability (limited to few thousand cycles), shelf life, and inability to quickly recharge (limited to tens of minutes). Commercial ultracapacitors are energy storage systems that solve these problems by offering more than one million recharges with little capacitance degradation, recharge times on the order of few seconds, and unlimited shelf life. However, today's ultracapacitors are limited by their low energy stored per unit of volume and weight (5% that of a lithium ion battery), and their high cost (ten times greater than that of lithium ion batteries) per unit of energy stored.

This thesis presents vertical carbon nanotubes-based electrodes designed to achieve, when packaged into an ultracapacitor cell, a four to seven times higher power density (7.8 kW/l) and a five times higher energy density (31 Wh/l) than those of activated carbon-based ultracapacitors. Models to predict the energy density, power density, and efficiency of an ultracapacitor cell using vertical carbon nanotube electrodes of a given morphology are described.

The synthesis of carbon nanotube electrodes fabricated on thin conducting substrates of tungsten and aluminum that have the target nanotube average diameters and lengths is described along with insights on the thermodynamics of the nanotube growth reaction. The low pressure chemical vapor deposition reactor used to fabricate nanotube electrodes on conducting substrates is described.

Electrochemical measurements of electrodes are presented to corroborate electrochemical modeling leading to the performance prediction of carbon nanotube-based ultracapacitors. Finally, some key remaining questions to further advance the understanding of nanotubes as electrode materials for ultracapacitor are presented.

Acknowledgments

This thesis is the result of an exciting six year research within the vibrant MIT energy community. This period of professional studies has been for me extremely pleasant, motivational, and enriching thank to a number of mentors, friends, and companies. Many of them, through their support, helped me shape a vision and a path to contribute to solve, through paradigm-shifting energy storage technologies, the energy challenges that afflict our beloved Country, the United States of America, and our society. They also helped me find the strength to relentlessly proceed toward the accomplishment of my professional and personal goals. This includes:

- My advisors Professor John Kassakian and Professor Joel Schindall. I would like to thank them for offering me the opportunity to work on this extremely exciting project during my Doctorate. I would like to thank Professor Kassakian for the confidence that he had since the beginning in my ability to deliver results within this project. Moreover, I would like to thank Professor Kassakian for his valuable mentorship and support. His rigorous, deliberate, and thorough writing style, thinking, and research approach have been models for me and have led me to grow into a better researcher. I would like to thank Professor Schindall for his open door policy, for having been always available throughout my Ph.D. His advice and visionary prospective, from his outstanding thirty year industrial career as an executive, much contributed to my professional growth. Furthermore, I would like to thank Professor Schindall for the responsibility and freedom I was given to technically lead this research project for which he secured continued level of funding. In addition, I would like to thank Professor Schindall's Family (his wife Alice, and his daughters Julie and Katie) for their kind hospitality and support throughout the years of my Doctorate.

- My thesis committee members Professor Sadoway and Professor Mildred Dresselhaus. I would like to thank Professor Sadoway for being, to me, very inspirational and for his profound technical comments on a variety of electrochemical and metallurgical aspects of my research. Also, I would like to thank Professor Sadoway for welcoming me as a part of his dynamic research group. I would like to thank Professor Dresselhaus and her group for being very supportive in helping me, during my first years of research, to become familiar with carbon nanotubes and other carbon systems. Moreover, I would like to thank Professor Dresselhaus for her precious support that led to a significant improvement of my thesis.

- My former advisors Professor Alessandro Gandelli and Professor Mircea Driga. I would like to thank professor Gandelli for having been to me a valuable mentor for the past twelve years and for the important role he had throughout my academic career in Italy and in the US. I would like to thank Professor Driga for having being extremely supportive of me for this past nine years since I first arrived to the United States and for offering me the opportunity to work with his research group when I first came to the United States.

Contents

List of Figures

List of Tables

Thesis Motivation and Outline

1.1 Introduction to Ultracapacitors

Today's batteries, which store energy through a heterogeneous charge transfer mechanism (faradaic reaction), are limited by their cycleability (only a few thousand full charge and discharge cycles), shelf life, and ability to quickly recharge.

Ultracapacitors store energy in the electric field within a double layer of charge at the electrode/electrolyte interface, rather than through a faradaic reaction. Because of their energy storage mechanism, ultracapacitors already solve many of the issues associated with batteries by achieving more than one million recharges with little to no capacitance degradation, recharge times in the order of seconds, and an unlimited shelf life. The drawbacks of today's ultracapacitors, though, are their low energy stored per unit of volume and weight (only 5% that of a lithium ion battery) and their high costs (typically ten times higher than those of lithium ion batteries).

1.2   Motivation

This thesis began six years ago with the realization of a way to increase the huge potential that ultracapacitors have as high power, long life, and robust energy storage devices. By investigating the structure and components of ultracapacitors, we realized that by replacing the activated carbon electrode structure with an array of carbon nanotubes it might be possible to increase the energy density of these device as much as five to seven times. Later we also confirmed that this carbon nanotube electrode structure could lead to a power density four to seven times higher than current ultracapacitors. These significant improvements might lead to a device that could provide a power density twenty times higher than high power batteries at higher efficiency, that can be cycled indefinitely without the need to be derated, that can store more than five times the energy of a conventional ultracapacitor (up to thirty percent that of a lithium ion battery), while reducing the cost relative to existing ultracapacitors.

In the next few years, the further development and commercialization of this carbon nanotube-based ultracapacitor has the prospect of benefitting a variety of products and applications which are today constrained by the limitations imposed by commercial energy storage systems. It would be particularly beneficial to many existing applications where a combination of high energy density, power density, longevity, cycle-ability, low cost of ownership over a twenty years life, and reliability are critical.

1.3   Accomplishments of our Research

During our research, presented in this thesis, we made contributions to the design of electrodes that might lead to a higher efficiency, five times higher energy density, and four to seven times higher power density than those of activated carbon-based ultracapacitors. In addition, we developed models to predict the capacitance, energy density, power density, and charge discharge efficiency for a packaged ultracapacitor cell based on carbon nanotube electrodes of a given morphology. These models were validated by our electrochemical measurements of carbon nanotubes and of activated carbon electrodes, which were used as a baseline.

Furthermore, we also made important progress towards the fabrication of our target carbon nanotube electrodes. That is, we designed and build a reactor for the fabrication of nanotube electrodes, we optimized a procedure to fabricate nanotube electrodes on thin conducting substrates, and we achieved the growth of nanotubes having the right lengths and average diameters but that still present a three times lower surface density than our target (this density was though improved by an order of magnitude during the course of 12 months). The two remaining challenges to the development of our target electrodes are the fabrication of nanotube layers having a higher surface density of nanotubes and a higher capacitance for a given nanotube surface area.

1.4   Outline

This thesis describes six years work on the design, fabrication, assembly, characterization, and modeling of an innovative double layer capacitor based on electrodes using vertical carbon nanotubes as an active layer material. This work was carried out at the Laboratory for Electromagnetic and Electronic Systems in collaboration with a number of other key MIT laboratories and groups, such as Professor Sadoway and his group, Professor Dresselhaus' group, MTL, and the CMSE electron microscopy laboratory.

Chapter 2 describes the structure and the operating principle of ultracapacitors. The chapter broadly classifies the various types of electrical energy storage solutions such as batteries and capacitors in terms of their primary characteristics.

Chapter 3 outlines the factors that make nanotube-based electrodes a desirable material for the active layer of ultracapacitor electrodes as well as the challenges which need to be overcome. The chapter reports some of the major contributions to the field of carbon nanotube ultracapacitor electrodes prior to the development of our approach. Then the chapter discusses an analysis of the energy density that could be achieved if the electrode structure having parameters that we propose is packaged in an ultracapacitor cell. A justification for the choice of electrode parameters is presented. The chapter concludes by describing the historical development of the understanding of the double layer model which is the operating principle of ultracapacitors.

Chapter 4 focuses on the fabrication of nanotube electrodes. The chapter starts with a

summary of the relevant thermodynamics involved in our process of electrode fabrication. The chapter presents the procedure and the systems that we have designed and developed to fabricate carbon nanotube electrodes and it concludes by presenting the relevant aspects of the morphological electrode analysis.

Chapter 5 describes the electrical measurements of our carbon nanotube-based electrodes. From the capacitance measurements, we then extrapolate the energy density of a packaged cell using our electrodes. The chapter presents our procedure for assembling an electrochemical test cell that incorporates either carbon nanotube or activated carbon electrodes. The experimental results from measurements on the nanotube electrodes are compared with the measured performance of activated carbon electrodes, which are used as a baseline.

Chapter 6 presents for the first time a comprehensive approach to predict the frequency response of ultracapacitors with carbon nanotube electrodes. Moreover, from the frequency response predictions, the power density and the efficiency of a cell that uses carbon nanotube electrodes are extrapolated. The chapter examines the main contribution to the electrochemical modeling of the frequency response for porous materials. The chapter applies and validates the electrochemical models using activated carbon cells. We then extend these models to the case of carbon nanotube electrodes. The frequency response of our carbon nanotube electrodes is analyzed and the response of our target electrode is extrapolated using these models. Equivalent circuit models that simulate the frequency response of activated carbon and nanotube-based cells are proposed and their circuit parameters are associated with phenomena occurring at the electrodes. The

power density and efficiency of a D-size cell packaged using either our desired carbon nanotube or activated carbon electrodes are predicted using the model that we developed. Finally, an analysis that predicts the cell performance based on the average diameter of the nanotubes comprising the active layer is presented.

Chapter 7 summarizes the contribution of this research to the fabrication and understanding of high energy and power density carbon nanotube-based ultracapacitors and discusses the next set of challenges that we will undertake in continuing this research.

Introduction

This chapter begins by describing the energy storage mechanism in batteries and capacitors. It then introduces the ultracapacitor as an energy storage device, and describes the components of an ultracapacitor cell. The chapter then presents the vision that has motivated our research, over the past six years, on developing ultracapacitors based on carbon nanotube electrodes.

2.1 Background Summary

This section surveys the available electrochemical energy storage technologies and compares the performance of commercial rechargeable batteries with the performance of ultracapacitors. It then classifies the different capacitor technologies and finally it introduces the active areas of research in the ultracapacitor field.

2.1.1 Classification of Rechargeable Batteries and Ultracapacitors

Today there are a number of electrochemical storage systems used in a variety of applications ranging from portable electronics to hybrid vehicles. These different types of energy storage systems are selected depending on their cost and performance. The main categories of energy storage systems are divided into either batteries, where energy is stored through a Faradaic reaction, or capacitors, where the energy is stored in an electric field. Generally, batteries are capable of higher energy densities than capacitors, but are charge/discharge cycle limited. As shown in Fig. 2.1, the field of batteries is divided into primary and secondary types. Primary batteries are non-rechargeable and thus can only be used once, whereas secondary batteries are rechargeable and thus can be cycled a number of times before losing their ability to store charge.

Rechargeable batteries are divided into categories defined by their chemistries - lithium ion (Li Ion), lead acid (PbO), nickel metal hydride (NiMH), and nickel cadmium (NiCd).

2.1.2 Classification of Capacitors

The types of capacitors divide in four major categories of devices, which are described in this section. As shown by Fig. 2.2, the types of capacitors are also divided into sub classes that achieve different performance, depending on the choice of electrode and electrolyte.

Electrostatic capacitors are used as components in electronic and high frequency filtering applications which require operation at frequencies up to hundreds of MHz. The electrode
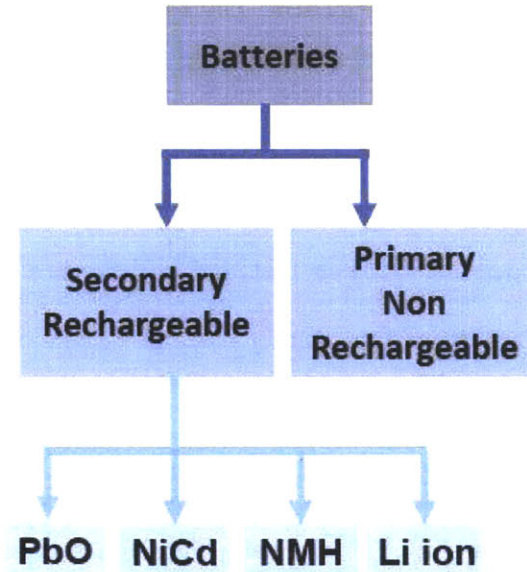
Figure 2.1: Summary of some of the most important types of batteries used today.

of these capacitors is typically made of copper or aluminum and as the dielectric between the electrodes air, mica, polymer film or a ceramic are used. By keeping the dielectric moisture-free, these capacitors can achieve very high operating voltages. The RC time constant of electrostatic capacitors can be on the order of nano seconds, their gravimetric and volumetric energy densities are on the order of 1.5 mWh/kg and 2 mWh/l, and the number of charge-discharge cycles is unlimited.

Electrolytic capacitors are polar devices in which the anode is made of a rough aluminum film coated with a thin aluminum oxide film and the cathode is made of rough aluminum[1]. The dielectric is formed by a liquid electrolyte and by the aluminum oxide layer. A paper film is used as a separator. These devices achieve a higher specific capacitance than elec-

---

[1]Aluminum is used as a cathode material due to its low cost and to its ability to be surface treated to increase its surface area leading to a higher specific capacitance. Even higher specific capacitance is obtained by electrolytic capacitors that employ sintered high surface area tantalum films as a cathode.
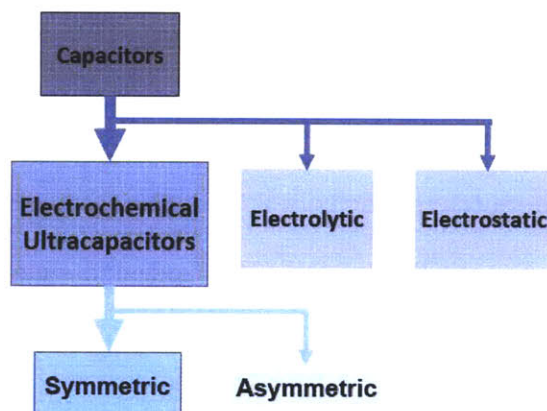
Figure 2.2: Summary of the types of capacitors available today.

trostatic capacitors thanks to the thinness of the aluminum oxide in conjunction with the liquid electrolyte. Although their maximum rated voltage is lower than that of electrostatic capacitors, their energy density is greater than that of the electrostatic capacitor due to their higher specific capacitance. Electrolytic capacitors have RC time constants on the order of milliseconds and they are used in filtering applications that require bandwidths on the order of a few kHz. Their volumetric and gravimetric capacitances are higher than those of electrostatic capacitors and consequently their energy densities are also higher - up to 30 mWh/kg and 120 mWh/l.

Our nanotube-based capacitor belongs to the category of **electrochemical symmetric capacitors or ultracapacitors**. These types of devices are made using carbon electrodes and electrolytes which are either aqueous or organic. Similar to electrostatic and electrolytic capacitors, no faradaic reaction takes place on the surface of either electrode, allowing for elevated cycleability[2]. Typical symmetric ultracapacitors present RC time constants on

---

[2]A faradaic reaction is a heterogeneous charge transfer taking place at one electrode. The charge transfer can be due either to intercalation or to a redox reaction which are the processes taking place at the surface

the order of one second, energy densities on the order of 5 Wh/kg and 6 Wh/l, and power density on the order of 5 kW/kg.

Electrochemical asymmetric capacitors are an hybrid between batteries and ultracapacitors. They typically present both a carbon electrode and a metal oxide electrode. The carbon electrode operates as an ultracapacitor and does not undergo a faradaic reaction, whereas the metal oxide electrode undergoes a faradaic reaction. This type of device has a lower longevity than regular ultracapacitors and slower RC time constants which are on the order of tens of seconds. Concurrently, though, they exhibit energy densities which are double those of commercial symmetric ultracapacitors and up to 10 Wh/kg and 12 Wh/l.

Table 2.1 shows typical performance parameters of some of the capacitors and batteries described in this section. The energy density refers to the full depth of discharge cycling of the device, the power density refers to the maximum power extractable from the device and the cycleability refers to the number of full deep discharge cycles before the capacity degrades below 80% of its initial value.

---

of battery electrodes.

Technology	Unit	Elec	LiFeP	NiMH	UCaps	Pb-acid
Energy density	Wh/kg	0.025	108	4.3	4.45	25
	Wh/l	0.036	221	5.4	6.6	55
Power density	kW/kg	287	1.08	8.5	8	0.2
	kW/l	406	2.22	10.6	11.8	0.4
Rated Voltage	V	25	3.6	2.7	2.7	12
Operating Temperature	°C	-55 +125				
Cycleability	Cycles	1M	2k	1k	1M	400
Cost of a 1 kWh	$/kWh	1.1M	2k	800	20k	250
System	cent/Cycle	100	100	66	2	62

Table 2.1: Table comparing the performance of different commercial energy storage technologies. The values are based on the volume and weight of the packaged cell. Elec refers to an example of aluminum electrolytic capacitors, LiFeP refers to lithium ion batteries having a lithium iron phosphate cathode and a carbon anode, NiMH refers to nickel metal hydrate batteries, UCaps refers to activated carbon-based ultracapaciotrs, and Pb-acid refers to lead acid batteries.

2.2 Symmetric Ultracapacitors

2.2.1 Description

The operating principle of double layer capacitors (DLCs), also known as ultracapacitors or supercapacitors, is based on the electrical double layer of charge that forms at the interface between a charged solid and an electrolyte, as discussed in detail in section 3.4. To familiarize the reader with this topic, the electrical double layer is introduced here using an analogy with the electrostatic capacitor[3] (see Fig. 2.3), which accumulates charge on two parallel conducting plates separated by an insulator. Electric energy is stored in the field between the electrodes. The DLC achieves significantly higher cell specific capacitance[4]

---

[3]Electrostatic (parallel-plate) capacitors are typically produced using a variety of dielectric materials including mica and paper.

[4]Cell specific capacitance is defined as the capacitance per unit volume or weight of the cell.
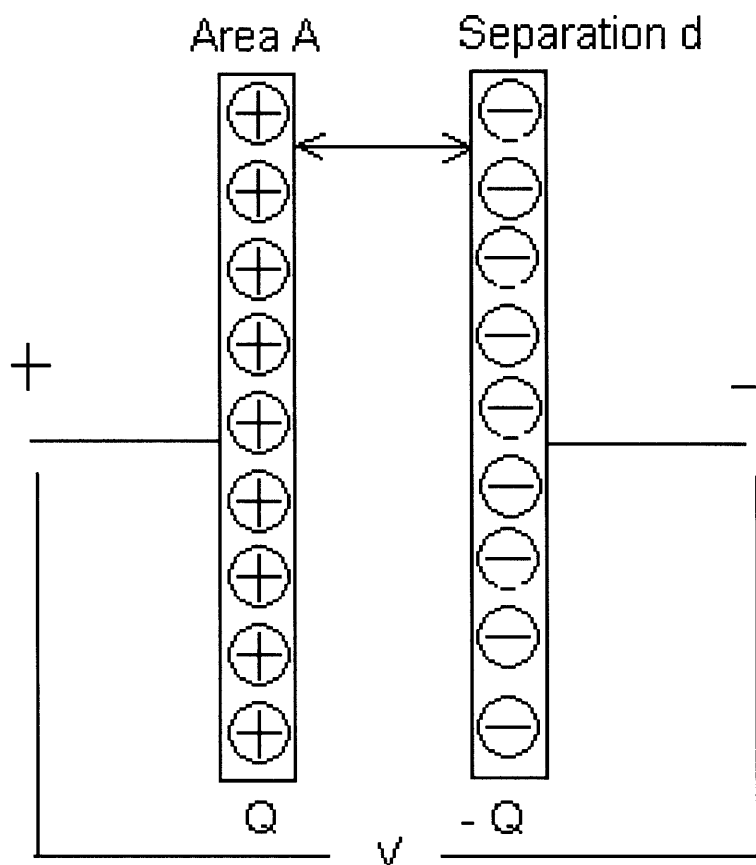
Figure 2.3: Schematic of a parallel-plate (electrostatic) capacitor. A is the area of the two electrodes, d is the distance between the two electrodes (indicated by the arrow), V is the rated voltage, and Q is the accumulated charge on each electrode.

than parallel-plate and electrolytic capacitors in two ways:

1. The electrode active layer is made of a porous material such as activated carbon, whose effective electrode surface[5] area A_E is several orders of magnitude higher than its Euclidean surface A.

---

[5]The electrode surface area A_E is the area per unit weight (m^2/g) of the electrode active layer. It is usually measured via gas absorption methods or BET [3].

2. The dielectric is replaced by an electrolyte filling the volume between the electrodes and within the electrode voids. When the capacitor is charged, two double layers of charge between the electrode and the electrolyte form at the cathode and at the anode. The two electrical double layers can be simplistically explained as two capacitors in series. In the simplest model, the two double layers of charge are characterized by a separation d' and d'', respectively, between the charge in the solid and liquid phase. Although d' and d'' can differ due to differences in the radii of the anion and cation in the electrolyte, they both have sizes on the order of a few angstroms (the approximate size of the solvated ion), and this separation is orders of magnitude less than the thinnest of solid insulators (see Fig. 2.4).

The DLC achieves a one to two order of magnitude higher dielectric field strength (at the double layer of charge) at each electrode when compared to electrolytic and electrostatic capacitors. The DLC's higher specific capacitance in conjunction with its higher dielectric field strength lead to the DLC's higher volumetric and gravimetric energy densities[6] over other types of capacitors. In addition, DLCs also achieve power densities ten time higher than those of batteries. But, currently despite this very large increase they only achieve 5% of the energy density of a lithium ion battery.

Further enhancement of activated carbon-based DLC performance is limited by:

1. the surface functional groups (impurities) instilled in the carbon by the activation pro-

---

[6]The gravimetric or volumetric energy density is, respectively, the energy a cell can store given, respectively, its weight E_W (Wh/kg) or volume E_V (Wh/l).

cess, which reduce the rated voltage;

2. the impurities present in the carbon, which reduce the ability to operate at higher potential;

3. the high resistance of the electrolyte in the pores, which affects the cell's frequency response and increases its series resistance, thus reducing the power density and the efficiency of the cell;

4. relatively low effectively usable surface area $A_{E\ ac}$, which reduces the specific capacitance and thus energy density of a carbon cell.

5. the resistance of the electrode binder, which increases the Joule dissipation and reduces the power density .

2.2.2 Components of an Ultracapacitor Cell

As Fig. 2.4 shows, the main components of a conventional activated carbon DLC cell are:

- the high surface area electrode,

- the separator,

- the electrolyte.

Considering each of the DLC's components in more details; **the DLC electrode**, as shown by Fig. 2.5, is composed of two parts:
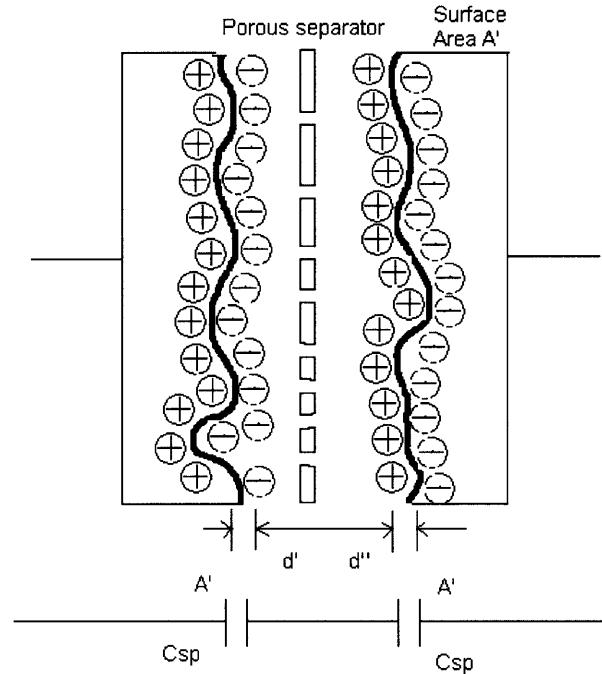
Figure 2.4: Schematic of a symmetrical carbon-based DLC showing the double layer of charge at the cathode and at the anode with a porous separator between them. A' is the surface area of the two electrodes, d' and d'' are the distances between the two double layers of charge at the two electrodes, C_{SP} is the specific capacitance in F/g of the two electrodes.

- the active carbon layer, which is composed of activated carbon particles that typically have a size from 2 to 10 μm leading to a high surface area film where the double layer effect takes place. The activated carbon particles are held together by a teflon based binder;

- the current collector, typically an aluminum conducting substrate supporting the active layer and connecting it to the DLC terminals[7].

---

[7]Aluminum is used due to the favorable tradeoff between its conductivity, ability to be laminated, and low cost.
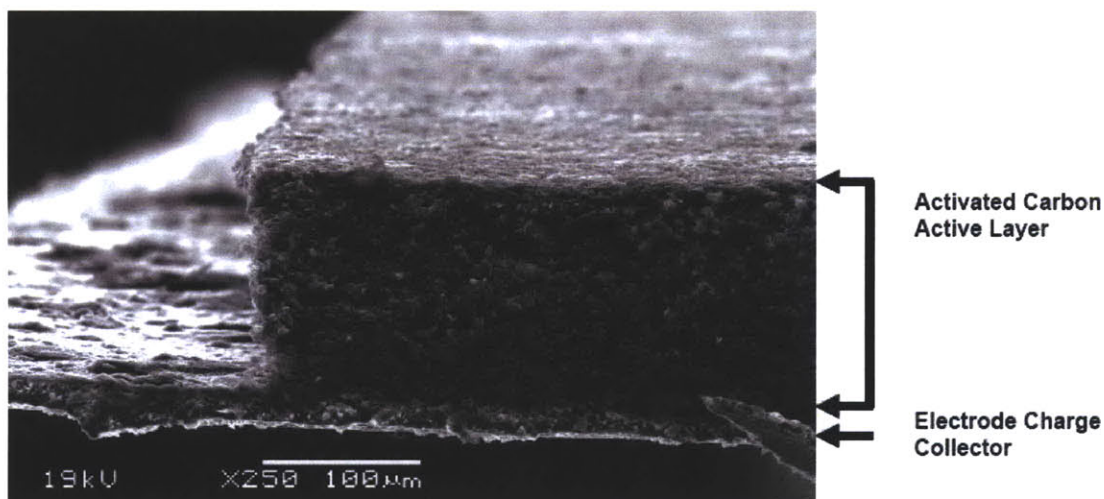
Figure 2.5: Scanning electron micrograph showing the cross section of a commercial activated carbon-based electrode in which an aluminum charge collector is covered by the activated carbon active layer. The picture was acquired using a JEOL 5910 SEM viewing the sample placed vertically onto the SEM stage.

As further discussed in section 3.2, the requirements for the electrode active layer material include high accessible surface area, high differential capacitance (electrode capacitance over the electrode surface area), low pore resistivity, low electrical resistance among the carbon particles in the carbon active layer, low content of adsorbed surface functional groups and impurities, and low cost.

The electrolyte is composed of a solvent and a salt. The requirements for the electrolyte include high electrochemical stability with the electrode active layer, high ionic mobility over a large range of ionic molarity, and low cost. The decomposition voltage, together with the reactivity of the active electrode material, determine the rated voltage of the cell. The ionic mobility directly controls the equivalent series resistance and thus the power density of the DLC cell. Organic electrolytes present a lower mobility than aqueous electrolytes, thus giv-

ing rise to a higher cell equivalent series resistance [2], however, their higher decomposition voltage makes them more desirable than aqueous electrolytes.

The separator in Fig. 2.4 is used to prevent short circuits between the electrodes and to permit ionic transfer from the negative to the positive electrode. This is necessary because as the capacitor charges, the concentration of negative ions (with respect to the bulk concentration) increases at the cathode and decreases at the anode. Conversely, the concentration of positive ions increases at the anode and decreases at the anode. The figures of merit that classify a separator are its conduciveness to permit ionic mobility, its dielectric strength, its weight, its ability to absorb electrolyte, and its cost. Therefore, a good separator should be very thin, not electrically conductive, capable of high temperature operation, highly porous, capable of being impregnated with electrolyte, and inexpensive.

2.2.3   Limitation of Activated Carbon Based DLC Electrodes

Almost all the development work on ultracapacitors has been devoted to activated carbon-based devices. However, today we are witnessing a saturation in the energy density improvement of these devices due to the intrinsic limitation of activated carbon electrodes.

High surface area activated carbon electrodes show an irregular structure with widely varying pore sizes, including pores that are too small for the electrolyte ions to penetrate and others that are too large for efficient utilization[8]. Furthermore, thicker films of carbon in-

---

[8]Wide distribution in pore sizes is due to the difficulty to control pore size during steam based activation processes.

corporate portions that cannot be accessed by the ions. As a result, such electrodes often do not fully utilize the electrode thickness. This leads to an energy density that is smaller than the energy density that could be achieved with a structure that better utilizes the entire surface. The used or effective surface area is typically 1/5 the area measured through BET testings.

The power density of activated carbon cells is limited by the poor activated carbon electrical conductivity and the poor mobility of the electrolyte ions through the irregular path from the electrode surface to the charge collector.

Moreover, the poorly conducting and amorphous nature of activated carbon forms electrically isolated islands that prevent the cell from fully discharging. The DLC rated voltage is reduced by the impurities and dangling bonds that the activation processes creates in the activated carbon. Such surface impurities are necessary for surface area augmentation, but they reduce the electrochemical stability of the carbon vs. the electrolyte interface. As an example, the typical rated voltage of activated carbon-based DLC cells is below 3 V, whereas the rated voltage of a DLC cell based on graphitic carbon is 3.7 V [3]. This rated voltage difference is due to the lower reactivity of graphite.

In the area of symmetric ultracapacitor carbon-based devices, research is currently ongoing and focused on increasing the energy density and power density as well as on cost reduction. The most promising investigations are trying to re-engineer carbon electrodes using graphitic carbon, aerogels, and carbon nanotubes. In the area of asymmetric ultracapacitors, new research has shown the ability to increase the energy density of symmetric

devices by replacing one carbon electrode with a metal oxide. The most promising metal oxides currently under investigation to enhance the energy density by using asymmetric ultracapacitors are ruthenium oxide and manganese oxide. The current technical limitation of these devices that is most serious is that at present they cannot attain any practical cycleability.

2.3 Chapter Summary

In this chapter we introduced the field of electrochemical energy storage devices by specifying the major types of commercial batteries, capacitors, and ultracapacitors. The operating principles of ultracapacitors were presented and the limitations of the state of the art activated carbon-based ultracapacitors were discussed. The next chapter will introduce the type of carbon nanotube-based ultracapacitors that have been the topic of this research aiming to improve ultracapacitors' energy and power density.

Carbon Nanotube Enhanced

Ultracapacitor

The previous chapter introduced the ultracapacitor as an electrical energy storage device. This chapter introduces a new type of ultracapacitor which uses carbon nanotube as an electrode material to improve the device energy and power densities. This chapter begins by presenting the advantages and challenges associated with the use of carbon nanotubes as an electrode material and by reviewing the major contributions in this field. This chapter then presents our approach of using vertical carbon nanotubes as a DLC electrode active layer in order to achieve energy densities more than five times greater than those achieved by commercially available ultracapacitors ($E_V \geq 31$ Wh/l vs. 5.5 Wh/l and gravimetric energy densities $E_W \geq 33$ Wh/kg vs. 5 Wh/kg). This chapter then presents the analysis that justifies our energy density estimates. This chapter ends with a review of the historical evolution of the double layer model, which is instrumental to the understanding of future chapters.

3.1 Literature Review of Carbon Nanotubes as DLC Electrode Material

This section presents the higher power density and rated voltage than might be achievable by using nanotubes as ultracapacitor electrode material, as reported by previous researchers. Concurrently, this section discusses the challenges associated with the improvement of energy density and with the fabrication of carbon nanotube ultracapacitor electrodes. At the end of this section Table 3.1 summarizes single electrode performance achieved with different types of carbon nanotube-based electrodes.

3.1.1 Contribution of Niu et. al.

Niu et. al. first showed the performance of DLC based carbon nanotube electrodes. By using entangled multi-walled nanotubes (MWNTs) and a nickel foil as a charge collector, Niu achieved a power density of 8 kW/kg and an energy density of 0.56 Wh/kg[1] [4]. From the electrode density and volume of Niu's electrode, one can compute its power density (163 kW/kg) and energy densities (12.6 Wh/l and 15.7 Wh/kg). Niu's device utilized catalytically grown CNTs with an average diameter of 8 nm that were produced by Hyperion Catalysis International. The CNTs were first pre-treated with nitric acid to disassemble the as-produced nanotube bundles. The individualized CNTs were then filtered, dried, and annealed to form an electrode of randomly entangled and thermally cross-linked CNTs.

---

[1]These figures are based on the weight of the electrolyte, separator, and of the two electrodes.

The CNT electrode had a uniform thickness of approximately 25.4 μm and required no binder since the functionalized carbon nanotubes were self-adhesive. Through the nitric acid treatment, the BET surface area increased from 250 to 430 m^2/g. Using 38 wt. % H_2SO_4 in water as the electrolyte, the maximum specific capacitance was 113 F/g or 90 F/cc and the differential capacitance was 24 F/cm^2. The "knee" frequency, or maximum frequency at which the capacitive behavior is dominant, was shown to be 100 Hz (49 F/g), significantly higher than the 1 Hz knee frequency of most commercial DLCs. This is an important consideration when ultracapacitors are considered to be used in filtering applications.

3.1.2   Contribution of An et. al.

An et al. showed a high specific capacitance achievable using an electrode based on heat treated single wall nanotubes (SWNTs) as the active layer [5]. The SWNT electrode consisted of 70 wt. % of randomly entangled and cross-linked SWNTs and 30 wt. % poly(vinylidene chloride) (PVDC) as the binder. The ratio of CNTs to binder was determined empirically. The electrode was then heat-treated for 30 minutes in argon at 900-1000°C. After the heat treatment, the electrode differential capacitance was approximately 50 $\mu F/cm^2$ and the surface area was 357 m^2/g. An's electrode achieved specific capacitances of 180 F/g and 135 F/cc in 7.5 molar KOH. The maximum power density and energy density claimed by An were, respectively, 20 kW/kg and 6.5 Wh/kg (An's report does not specify whether these figures are relative to the electrode weight or to the cell weight nor does it provides enough data to determine this).

3.1.3   Contribution of Yoon et. al.

The above discussed techniques were limited in their energy and power densities by either the need for pretreatment (Niu) or a binder (An), which increased the parasitic resistances. The use of randomly entangled CNTs instead of vertically aligned CNT arrays also limits performance. Yoon et. al. were able to decrease the contact resistance by directly growing vertically aligned CNTs on a Ni foil collector [6]. No catalyst was deposited on the current collector. MWNTs were grown using the plasma enhanced chemical vapor deposition method (PECVD) method with methane and hydrogen as the reactant gases. The CNTs were then treated with an NH_3 plasma to remove carbon impurities introduced in the growth process. The measured specific capacitance of the NH_3 treated device was 207 F/g with a surface area of 86.5 m^2/g. The directly grown CNT electrodes also exhibited nearly ideal cyclic voltammograms at scan rates up to 1000 mV/s. However, the grown CNT array achieved a thickness of only 20 nm, which is insufficient for viable energy storage purposes.

3.1.4   Contribution of Du and Pan

Du and Pan fabricated CNT electrodes by electrophoretic deposition (EPD) [7]. CNTs grown from another source are first suspended in a solution of nitric acid. After filtration by distilled water and rinsing with ethanol, the CNTs are then dried. The CNTs are dispersed in ethanol by sonication and deposited on Ni foil under the influence of an electric field. This process is similar to the Niu et. al. method, except with the introduction of a metal current collector. The electrical resistance of the as-deposited EPD films is extremely high

(in the order of kilo ohms); however, after annealing in a hydrogen environment, there is a drastic decrease in the resistance. This may be attributed to electrochemical oxidation that takes place during EPD, which is then reduced through hydrogen treatment. Du and Pan report near-ideal rectangular cyclic voltammograms at scan rates up to 1000 mV/s. The calculated specific capacitance is 84 F/g and the power density is 20 kW/kg.

3.1.5   Contribution of Kumar et. al.

Kumar et. al. have proposed a method of contact transfer of CNTs using low temperature solder alloys [8]. The process involves annealing a solder coated conducting substrate and placing it in close contact with a CNT array grown on a Si substrate. The CNTs then penetrate the solder surface and are entrapped and transferred after solidification of the solder. The use of solder provides a low contact resistance between the CNTs and the current collector. This method is capable of directly transferring an array of vertically aligned CNTs. A DLC produced using this procedure has not yet been reported. While transfer techniques sidestep the need to directly grow CNTs on a conducting substrate, producing DLCs using these methods require significant extra manufacturing steps as well as the need for a supply of CNTs from another source.

3.1.6   Contribution of Futaba et. al.

Futaba et. al. have produced a "SWNT solid", a highly dense, vertically aligned CNT structure [9]. It uses the surface tension of liquids to zip together a CNT forest initially

grown on silicon. The SWNT solid has a nanotube density on the order $8.3 \cdot 10^{12}$ CNT/cm^2,

an average nanotube diameter of 2.8 nm, and a BET surface area of 1000 m^2/g. An elec-

trochemical cell was produced by sandwiching the SWNT solid between platinum sheets,

using 1 M tetraethylammonium tetrafluoroborate (Et$_4$NBF$_4$) in a propylene carbonate (PC)

electrolyte. From the reported data, the specific capacitance of Futaba's electrode can be

estimated as (60 F/g and 48 F/cc, which lead to energy density estimates of 52 Wh/kg

and 42 Wh/l when charged to 2.5 V. A 100 μm thick SWNT solid electrode had a reported

power density of 43.4 kW/kg. The main limitation of Futaba's electrodes is its poor dif-

ferential capacitance of 6 μF/cm^2 when compared to that achieved by Niu's (24 μF/cm^2)

and An's (50 μF/cm^2) electrodes. Futaba's poor differential capacitance might be due to

ion starvation since the electrolyte molarity, limited to 1 mole/l, is not sufficient to provide

enough charge to the electrodes given the electrode surface area of 7.18 m^2 (for each 1 cm^2

electrodes in which the nanotube are 100 μm long) and the voltage of 2.5 V, as discussed

in section 3.3.3.

			Niu	An	Futaba
P_{SE}	Matched power density	kW/kg	163	20.2	40
E_{SE}	Energy Density	Wh/kg	15.7		52
E_{SE}	Energy Density	Wh/l	12.6		41.7
C_W	Gravimetric capacitance	F/g	113	180	60
C_V	Volumetric capacitance	F/cc	90.4	135	48
C_D	Differential capacitance	μF/cm^2	24	50	6
S_{BET}	Surface area	m^2/g	430	357	1000
R_S	Equivalent series resistance	Ω			
V_M	Maximum cell voltage	V	1	0.9	2.5

Table 3.1: Table of single electrode performance for different carbon nanotube-based electrodes. Unless otherwise specified performance values are based on the single electrode weight and volume.

3.2   Our Approach to Nanotubes as Ultracapacitor Electrodes

Instead of fabricating electrodes using entangled carbon nanotubes, other graphitic carbon materials, or activated carbon, we grow an ordered array of vertically aligned carbon nanotubes (VCNTs), that constitute the electrode active layer, directly on a conducting substrate. In this structure ions are stored in the spaces between nanotubes on the outside of each nanotube. While the device is charged, the electric double layer of charge forms between the charge at the nanoutbe outer walls and the layer of ions at the nanotube/electrolyte interface as illustrated by Fig. 3.1.   The factors responsible for our energy density enhancements are the combination of an improved electrode surface area, differential capacitance, and voltage rating. Our analysis predicts that an electrode based on vertical carbon nanotubes can lead to an effective surface area up to 1,342 m^2/g. This derives from the carbon carbon distance in a graphene plane (1.44 Å), from the hexagonal carbon atom arrangement in a nanotube wall and from the carbon atom weight of 12 times the mass of a proton. Each hexagon of carbon atoms has a surface of 5.39 Å^2 and a mass of two carbon atoms ($4.01 \cdot 10^{-23}$ g) and thus $S_{SWNT} = 1,342$ m^2/g. This predicted surface area of a single wall nanotube is close to the surface area of 1,100 m^2/g measured by [9]. Our goal is to fabricate arrays of VCNTs having approximately three walls. As shown in section 4.3.1 currently our electrodes have carbon nanotubes with an average of 6 walls. The surface area that we expect for as-grown three wall nanotube electrodes is 450 m^2/g. As predicted in section 3.4.3, and as experimentally shown in section 5.3.1, the use of VCNT-based electrodes in acteonitrile lead to a differential capacitance at a zero po-
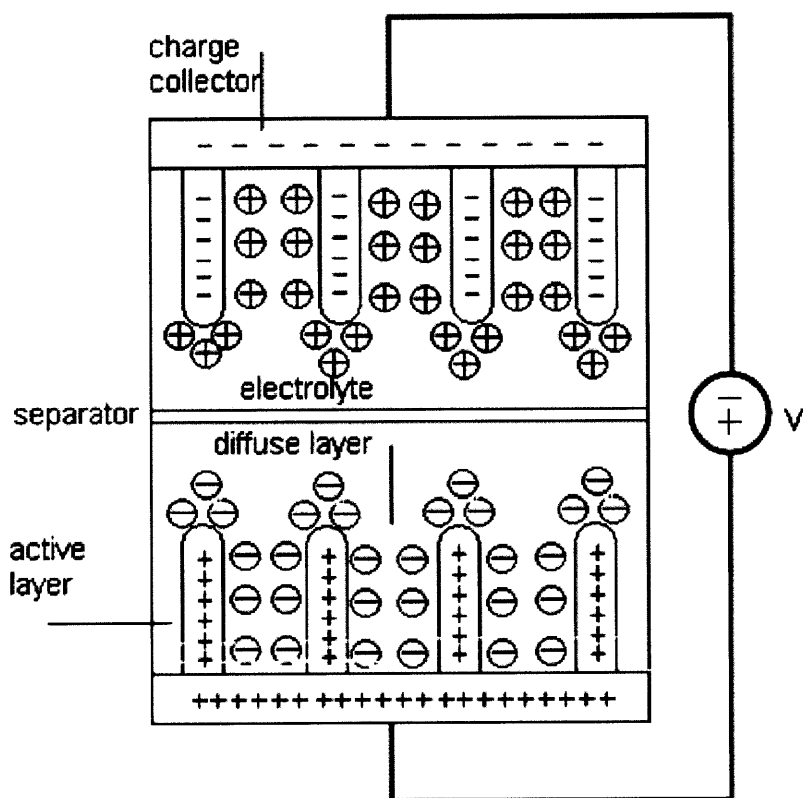
Figure 3.1: Illustration of the vertical nanotube-based ultracapacitor. The illustration shows the anode and the cathode, the separator between the anode and cathode, and the positive and negative electrolyte ions at the interface between the electrode and the electrolyte (solid/liquid interface).

tential of 10-12 μF/cm^2. As shown by An [7], a differential capacitance of up to 50 μF/cm^2 is achievable; we believe that our as-grown VCNT can be modified leading to a higher differential capacitance already demonstrated by An, which is expected to yield an electrode gravimetric specific capacitance up to 225 F/g. A discussion of different possible processes is included in the future work section of this thesis 7.2. As described in section 5.3, we are measuring the performance of our symmetric cell with a potential not exceeding 0.5 V to prevent faradaic reaction between the electrolyte and the currently used non-optimum
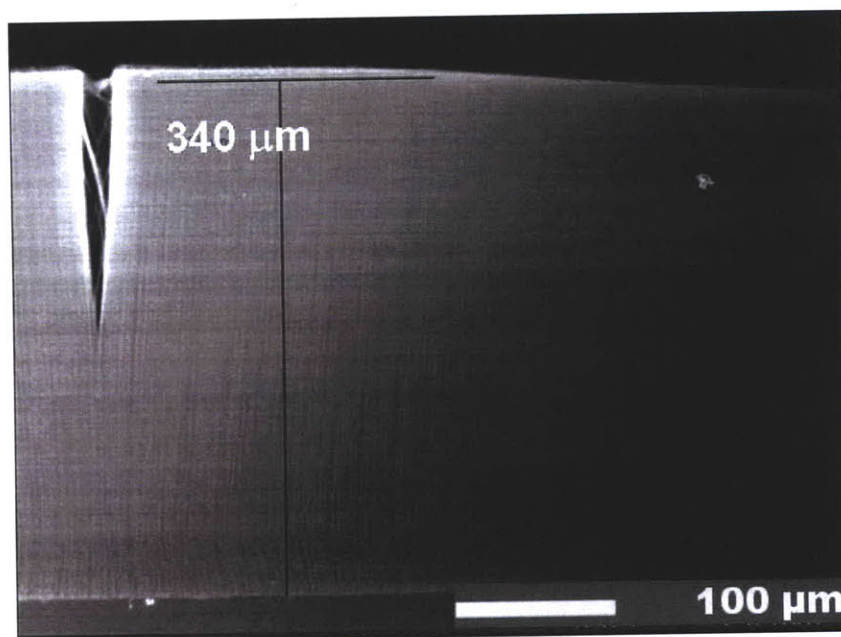
Figure 3.2: SEM micrograph showing the cross section of an electrode based on a film of vertically aligned CNT with a thickness of 340 μm.

electrochemical cell package. Upon optimization of our electrochemical test bench, we expect an increase in the maximum rated potential to 3.5 V, which has already been shown to be possible with the use of single wall nanotube-based electrodes with organic solvent by NipponChemicon [12].

As will be discussed in 3.3.3, an electrolyte providing ionic molarity greater than 1 mole/l is necessary to achieve the higher predicted device energy density. Our model predictions, summarized in Table 3.3, and our intermediate data show that for a packaged cell, energy densities of 33 Wh/kg and 31 Wh/l are achievable for a molarity of approximately 2 mole/l, which is currently commercially available.

As shown and explained in section 5.3, the equivalent series resistance, R_S, of our cell is

lower than that of an activated carbon-based cell. As shown in section 6.5, we project

the power density (at a round trip efficiency of 80%) of a D-size cell that uses our carbon

nanotube electrode to be 7.8 kW/l which is seven times higher than that of a D-size cell

that uses activated carbon electrodes (1.1 kW/l).

3.3 Performance Modeling for our Carbon nanotube-based Double Layer Capacitor Cell

This section analyzes the capacitance and operating voltage, and thus the energy, which can be stored by ultracapacior, which use carbon nanotube electrodes having defined features. Then an analysis of the influence of each cell component on the weight and volume of the cell is presented. Ultimately, the objective of this section is to offer guidelines for the estimation of the gravimetric and volumetric energy densities of a carbon nanotube-based DLC electrode packaged cells.

3.3.1 Assumptions and Constants

The electrode active layer is assumed to be a forest of preferentially vertically aligned nanotubes having an average diameter (d_C) of 6.5 nm and three walls for each nanotube (NW_C). The average spacing between nanotube centers (D_C) is assumed to be 10 nm, which corresponds to a nanotude density of 10^{12} cm^{-2}. The thickness of the nanotube active layer (t_C) is 200 μm. The aluminum charge collector thickness (t_{Al}) is assumed to be 25 μm. The area of the electrode considered (A_E) is 1 cm^2. Table 3.3.1 lists the parameters used for the energy density modeling. The theoretical gravimetric surface area of a single wall nanotube is (S_{SWNT}) 1,342 m^2/g; therefore, the surface area of three wall nanotubes[2] is one third of the figure above $(S_{3WNT} = 447$ m^2/g$)$. The Faraday constant

---

[2]This derives from the fact that only the external surface of a nuanotube is seen by electrolyte ions in a DLC electrode.

(F) is 96484 C/mol, and the density of aluminum (ρ_{Al}) is 2.7 g/cm^3. As shown by An [5],

the differential capacitance (C_D) achievable with CNTs can be up to 50 μF/cm^2 and this

value is assumed for the calculations. The maximum operating voltage for the cell (V_M)

is assumed to be 3.5 V similarly to the voltage shown possible by NipponChemicon® with

nanotube electrodes [10]. The increased voltage (2.7 V for activated carbon) arises because

graphene has a lower reactivity than activated carbon. The electrolyte density (ρ_{ACN}) is

considered to be 0.8 g/cm^3 with a molarity (M) of 2 mole of salt in one liter of solvent,

which can be achieved with available for industrial commercial acetonitrile. The separator

paper is assumed to have a density (ρ_S) of 0.8 g/cm^3 and a porosity (π_S) of 60 % voids

over the total paper volume, which are typical figures for separators used in ultracapacitor

cells. The thickness of the paper (t_S) used is 40 μm.

Symbol	Parameter Name	Parameter Value
d_C	CNT diameter	6.5 nm
NW_C	Number of walls for the CNTs	3
D_C	Average spacing between CNTs	10 nm
t_C	Average length of the CNT film	200 μm
t_{Al}	Charge collector thickness	25 μm
A_E	Electrode area	1 cm^2
S_{SWNT}	Single wall nanotube surface area	1342 m^2/g
S_{3WNT}	Three wall nanotube surface area	447 m^2/g
F	Faraday constant	96484 C/mol
ρ_{Al}	Aluminum density	2.7 g/cm^3
C_D	CNT specific capacitance	50 μF/cm^2
V_M	Maximum operating voltage	3.5 V
ρ_{LI}	Electrolyte density	0.8 g/ml
M	Molarity	2 mole/l
ρ_S	Separator density	0.8 g/ml
π_S	Separator porosity	60 %
t_S	Separator thickness	40 μm
$P_\%$	Added volume and weight of cell package	20 %

Table 3.2: Parameters used for the energy density modeling described in section 3.3.

3.3.2 Calculations

Based on the above assumptions and the parameters in Table 3.3.1, this section shows the computations leading to the prediction of the gravimetric and volumetric cell energy densities. These results account for the weight and volumes of the different cell components and casing. Accounting for the thickness of the charge collector and of the electrode surface, the weight of the aluminum substrate is:

$$W_{Al} = \rho_{Al} \cdot t_{Al} \cdot A_E = 4.05 \ mg. \tag{3.1}$$

The filling factor is indicative of the ratio between carbon nanotube volume and total volume, and is given by

$$Fill = \frac{\pi \cdot d_C^2}{4 \cdot D_C^2} = 0.332. \tag{3.2}$$

The void volume ε_V is given by

$$\varepsilon_V = 1 - Fill = 1 - \frac{\pi \cdot d_C^2}{4 \cdot D_C^2} = 0.668. \tag{3.3}$$

The surface multiplier factor is the number of times the euclidian surface of the electrode is enhanced by the nanotube-based active layer, and is given by

$$A_X = \frac{\pi \cdot d_C \cdot t_C}{D_C^2} = 40,841. \tag{3.4}$$

The total surface area of a 1 cm^2 electrode is given by

$$A_{TOT} = A_E \cdot A_X = 4.08 \text{ m}^2. \tag{3.5}$$

The weight of the nanotube active layer of a 1 cm^2 electrode composed of three wall nanotubes is

$$W_C = \frac{A_{TOT}}{S_{3WNT}} = 9.08 \text{ mg} \tag{3.6}$$

(3.7) calculates a specific capacitance of 225 F/g for the considered electrode structure, which is a factor of four higher than that of activated carbon electrodes:

$$C_W = A_{TOT} \cdot C_D/W_C = 225 \text{ F/g}. \tag{3.7}$$

For the assumed 1 cm^2 electrode, the total capacitance, C_T, is calculated by considering that an ultracapacitor cell is formed by two CNT electrodes in series:

$$C_T = A_{TOT} \cdot C_D/2 = 1.02 \text{ F}. \tag{3.8}$$

Given the rated voltage and the cell capacitance, the total charge stored on both electrodes of the double layer capacitor cell is given by

$$Q_m = \frac{A_{TOT} \cdot C_D}{2} \cdot V_M = 3.57 \text{ C}. \tag{3.9}$$

Q_m is the minimum required charge from the electrolyte ions. In order to retain electrolyte conductivity, the amount of electrolyte ions used in a typical device is 50% more than the minimum, and thus is given by

$$Q_R = \frac{A_{TOT} \cdot C_D}{2} \cdot V_M \cdot 1.5 = 5.36 \text{ C.} \tag{3.10}$$

The electrolyte weight, W_{LI}, based on an acetonitrile solvent, is calculated by considering the charge required, the electrolyte molarity, and the electrolyte gravimetric density:

$$W_{LI} = \frac{Q_R \cdot \rho_{LI}}{M \cdot F} = 22.22 \text{ mg.} \tag{3.11}$$

The energy density of the two carbon nanotube active layer is

$$E_{W2C} = \frac{1}{8} C_W \cdot V_M^2 = 344 \ J/g = 96 \text{ Wh/kg.} \tag{3.12}$$

The total energy stored in the DLC cell comprised of two 1 cm^2 electrodes is

$$E_T = E_{W1} \cdot 2 \cdot W_C = 6.25 \text{ J.} \tag{3.13}$$

Taking into account the weight of the electrolyte, an aluminum charge collectors with a thickness of 25 μm, and the active layer for both electrodes, the energy density of the cell is

$$E_{W2} = \frac{E_T}{3.6 \cdot (W_{Al} + 2 \cdot W_C + W_{LI})} = 36.5 \text{ Wh/kg.} \tag{3.14}$$

It is important to compute the void volume, V_V, in the electrode active layer V_{VC} and in the separator V_{VS} since this volume is not occupied by carbon, it has to be filled with electrolyte. To reduce the weight of the total cell, it is important that the void volume be close to the required electrolyte volume.

$$V_V = V_{VC} + V_{VS} = 2 \cdot \varepsilon_V \cdot t_C \cdot A_E + t_S \cdot \pi_S \cdot A_E = 0.029 \text{ cm}^3 \qquad (3.15)$$

In the cell design the volume of the required electrolyte should match the void volume in the carbon nanotube electrode and in the separator.

$$V_{LI} = W_{LI}/\rho_{LI} = 0.029 \text{ cm}^3 \qquad (3.16)$$

The total volume of the active layers of both electrodes' is given by

$$V_{2C} = 2 \cdot t_C \cdot A_E = 0.04 \text{ cm}^3. \qquad (3.17)$$

The total weight of the separator is given by

$$W_S = \rho_S \cdot V_S = 3.2 \text{ mg}. \qquad (3.18)$$

The volume of the cell, given 1 cm^2 electrodes, accounts for the volume of the CNT active layers, the charge collectors, the separator, for the (20%) packaging, and thus the total volume is

$$V_T = (2 \cdot V_C + V_{Al} + V_S) \cdot 1.2 = 0.055 \text{ cm}^3. \qquad (3.19)$$

The volumetric energy density of the cell E_V is therefore

$$E_V = \frac{E_T}{3.6 \cdot V_T} = 31 \text{ Wh/l.} \tag{3.20}$$

Similarly, once all of the same components are taken into account, the maximum gravimetric energy density of the cell E_W under the stated assumptions can be calculated with (3.21) and (3.22).

$$W_T = (W_{Al} + W_{LI} + 2 \cdot W_C + W_S) \cdot 1.2 = 53 \text{ mg} \tag{3.21}$$

$$E_W = \frac{E_T}{3.6 \cdot W_T} = 33 \text{ Wh/kg} \tag{3.22}$$

3.3.3   Results Discussion and Possibilities for Performance Enhancement

Table 3.3 summarizes the energy density achievable with the proposed CNT electrode structure. It shows that a CNT electrode structure could result in energy densities six times as high as those achieved using activated carbon. It is important to note that the molarity of the electrolyte considered is commercially available for an acetonitrile and propylenecarbonate based electrolyte. The differential capacitance of untreated nanotubes, as calculated in section 3.4 and as experimentally shown in section 5.3, is approximately 12 μF/cm^2. The differential capacitance assumed for our modeling is comparable to that shown using surface treated nanotubes by An [5] of 50 μF/cm^2. This higher differential capacitance coupled with the use of a 2 molar electrolyte can lead to the predicted energy densities of 31 Wh/l and 33 Wh/kg.

Symbol	Parameter Name	Parameter Value
d_C	CNT diameter	6.5 nm
NW_C	Number of walls for the CNTs	3
D_C	Average spacing between CNTs	10 nm
t_C	Average length of the CNT film	200 μm
t_{Al}	Charge collector thickness	25 μm
C_D	CNT differential capacitance	50 μF/cm^2
V_M	Maximum operating voltage	3.5 V
M	Molarity	2 mole/l
$P_\%$	Volume and weight of cell package	20 %
E_V	Volumetric energy density accounting for packaging	31 Wh/l
E_W	Gravimetric energy density accounting for packaging	33 Wh/kg

Table 3.3: Table summarizing the energy density predicted for the VCNT DLC based cell according to the modeling described in section 3.3.

A further increase in the nanotube surface area (achievable through either an increase in the nanotube density or in the nanotube average diameter) or in the nanotube differential capacitance would result in an energy density increase if an electrolyte with a molarity of salt higher than 2 mole/l were available. For instance, 1 cm^2 nanotube electrodes in which the nanotubes have a length of 200 μm, a density of 10^{12} cm^{-2}, and an average diameter of either 8 or 9 nm would present electrode surface areas of 5.03 m^2 and of 5.66 m^2, respectively. An ultracapacitor packaged with these electrodes could achieve energy densities of 45 Wh/l or 50 Wh/l, respectively. These two cases would require electrolytes having, respectively, molarities of 3.2 or 4.8 mole/l. Currently, these types of electrolytes or ionic liquids present high costs and much lower conductivities (their five to ten times lower conductivity would decrease the device power density) than a 2 molar electrolyte, and are not yet available in large scale volumes. Given the available electrolytes, the expected energy density of our ultracapacitor design is optimized with respect to the nanotube average diameter, density,

and differential capacitance. Not only do we believe that the target values chosen for these parameters are achievable, but also that they could result in the highest ultracapacitor energy density given the electrolyte molarities that are industrially available.

3.4   Historical Evolution of the Electrical Double Layer Model

The previous section presented a model that predicts the capacitance and the energy density of an ultracapacitor cell packaged using carbon nanotube-based electrodes and mentioned that the differential capacitance of untreated nanotube is of 12 $\mu F/cm^2$. This section analyzes the expression and the value of the differential capacitance for untreated nanotube electrodes given electrolyte parameters while reviewing the historical evolution of the understanding and modelling of the double layer of charge. The discussion and analysis presented in this section can be found in [11].

3.4.1   Helmholtz Model

The first researcher to observe the presence of a double layer of charge at the interface between a liquid and a charged solid was Helmholtz in 1853 [12]. According to the Helmholtz model, the interface between a liquid electrolyte and a charged solid phase resembles a parallel plate capacitor, where a sheet of charge resides in the solid and a sheet of counter charge resides in the electrolyte. The separation between these two sheets of charge is on the order of molecular dimensions. Under the assumption postulated by the Helmholtz

model, the relation between the stored charge, Q, and the voltage drop, V, between the sheets is predicted by the relation

$$Q = \frac{\varepsilon \cdot \varepsilon_0 \cdot A}{d} \cdot V \tag{3.23}$$

where ε is the relative dielectric constant of the solvent and ε_0 is the dielectric constant of vacuum, and d is the average distance between the layers of charge in the double layer. Even though this initial understanding was qualitatively significant, the model does not describe the experimental results well. Specifically, the differential capacitance is

$$C_{D\,H} = \frac{\varepsilon \cdot \varepsilon_0}{d} \tag{3.24}$$

and as predicted by the Helmohltz model does not account for a dependence on the applied voltage and electrolyte molarity. However, if we consider the case of an acetonitrile electrolyte with one molar tetramethylammonium tetrafluoroborate $(TEMA - BF_4)$ salt, the predicted differential capacitance calculated using (3.24), assuming a distance d of 3 nm, which is on the order of the solvated ion size, and an acetonitrile dielectric constant of 37.5, is $C_{D\,H} = 11\ \mu F/cm^2$, which is almost exactly equal to that observed for carbon nanotube electrodes at a 0 V bias, as shown in section 5.3.

3.4.2   Gouy-Chapman Diffuse Layer Model

Independently, Gouy and Chapman [13] [14] understood that charge in the electrolyte is stored over a finite space and not in a sheet like the Helmholtz model assumes. The ions storing charge in solution are attracted to the electrode surface by electrostatic forces and concurrently the ion distribution is randomized by thermal processes. According to the Gouy-Chapman double layer theory, the diffuse ionic layer in solution can be modeled with adjacent reference laminae of thickness dx from the electrode surface. The concentration of each ionic species over each adjacent lamina in solution depends on the potential $\phi(x)$ at a distance x from the electrode surface and on the concentration of the ith ionic species, n_i, in the bulk of the solution. Such a concentration is given by (3.25), where z_i is the signed number of charges per ion of the ionic species considered and k is the Boltzmann constant

$$n_i = n_i^0 \cdot e^{(-z_i q \phi(x)/kT)} \tag{3.25}$$

where n_i^0 is the concentration of the specie at zero potential, q is one unit of electron charge and $\phi(x)$ is the potential difference from the bulk of the electrolyte to different points in the diffuse layer. The overall charge for all the ionic species i at a distance x from the surface (where $x = 0$ identifies the position of the surface) is given by

$$\rho(x) = \sum_i n_i(x) z_i q = \sum_i n_i^0 z_i q e^{(-z_i q \phi(x)/kT)}. \tag{3.26}$$

The integration of the Poisson's equation (3.27) given the charge distribution $\rho(x)$ from 3.26 yields several meaningful results described below:

$$\rho(x) = -\varepsilon\varepsilon_0 \frac{d^2\phi}{dx^2} \tag{3.27}$$

The double integration of the Poisson equation, while dropping the subindex i, for a given $\rho(x)$ yields the potential profile ϕ as a function of the total potential drop between the solid and the bulk of the electrolyte, ϕ_0.

$$\frac{\tanh(zq\phi(x)/4kT)}{\tanh(zq\phi_0/4kT)} = e^{-\kappa x} \tag{3.28}$$

In (3.28) κ has the dimensions of cm^{-1} and is given by (3.29). For an acetonitrile-based electrolyte for which the relative dielectric constant ε is 37.5, κ depends on the electrolyte molarity (M that derives from the concentration n_0) in mole/l, and its expression is given below

$$\kappa = \left(\frac{2n^0 z^2 q^2}{\varepsilon\varepsilon_0 kT}\right)^{1/2} = (4.77 \cdot 10^7) z M^{1/2}. \tag{3.29}$$

Only under the condition of a small applied potential ϕ_0, which is $(zq\phi_0/4kT) < 0.5$, equation (3.28) simplifies to

$$\phi(x) = \phi_0 e^{-\kappa x}. \tag{3.30}$$

From the differential equation (3.31) solved at x = 0 and the potential given by (3.28), the

surface charge, σ^M, at the solid-liquid interface can be computed with (3.32).

$$Q = \varepsilon\varepsilon_0 A(\frac{d\phi}{dx})_{x=0} \tag{3.31}$$

$$\sigma^M = -\sigma^S = \frac{Q}{A} = (8kT\varepsilon\varepsilon_0 n^0)^{1/2}\sinh(\frac{zq\phi_0}{2kT}) \tag{3.32}$$

σ^S is the surface charge on the solid side of the interface and σ^M on the liquid one. The

surface charge, σ^M, given in $\mu C/cm^2$ at the electrode surface has the dependence given by

(3.33) as a function of the total potential drop ϕ_0 and of the electrolyte molarity in mol/l.

$$\sigma^M = 8.1M^{1/2}\sinh(19.5z\phi_0) \tag{3.33}$$

From the charge density (σ^M) the differential capacitance $(C_{D\ GC})$ predicted by the Gouy-

Chapman model as a function of the potential drop (ϕ_0) can be computed with

$$C_{D\ GC} = \frac{d\sigma^M}{d\phi_0} = (\frac{2z^2q^2\varepsilon\varepsilon_0 n^0}{kT})^{1/2}\cosh(\frac{zq\phi_0}{2kT}) = 157zM^{1/2}\cosh(19.5z\phi_0)\ \mu F/cm^2. \tag{3.34}$$

The Gouy-Chapman (GC) theory constitutes a significant improvement from the Helmohltz

theory, and the behavior of double layers at low electrolytic concentration and applied po-

tentials can be predicted using the GC theory. However, there are still some significant

discrepancies between its predictions and the experimentally observed behavior of dou-

ble layers. At potentials higher than "the point of zero charge", experiments show that

the differential capacitance becomes constant with voltage whereas the GC model predicts

exponential growth with increasing voltage. At higher electrolyte concentrations, the differential capacitance also flattens out and saturates at a maximum value, whereas the GC theory predicts a continuous increase of the differential capacitance with molarity.

3.4.3   Stern Modification - Gouy-Chapman-Stern Model

To correct the unlimited rise of the differential capacitance with voltage predicted by the Gouy-Chapman theory, Stern unified the Gouy-Chapman and the Helmholtz models [15]. The Gouy-Chapman-Stern (GCS) theory combines the Helmholtz layer with the Gouy-Chapman diffuse layer. In the GCS theory, the Helmholtz Layer (HL), constitutes the layer of closest approach for the ion to the electrode surface. Indeed, the thickness of the HL is directly related to the size of the solvated ions[3].

This double layer description known as the Gouy-Chapman-Stern (GCS) model is important when the diffuse layer thickness is comparable to the Helmholtz layer thickness. Therefore, the GCS model is particularly important in the presence of electrolytes with high ionic concentrations or in the presence of a high total potential difference between the electrolyte surface and the electrolyte bulk solution.

The expression for the total differential capacitance for the GCS model becomes a sum of two terms: the differential capacitance of the diffusion layer and the differential capacitance of the HL. Of these two terms, only the first is voltage dependent. Equation (3.35) shows

---

[3]Depending on the electrolyte salt and solvent, the HL thickness typically varies from a few angstroms to nanometers.

the expression for the total differential capacitance

$$C_{D\ GCS} = \left(\frac{x_2}{\varepsilon\epsilon_0} + \frac{1}{(2\varepsilon\varepsilon_0 z^2 q^2 n^0/kT)^{1/2}\cosh(zq\phi_2/2kT)}\right)^{-1}. \qquad (3.35)$$

The differential capacitance $C_{D\ GCS}$ can be modeled by the series connection of two capacitors. One capacitor is composed by the Helmholtz layer and its differential capacitance has the same expression as that predicted by the Helmholtz model

$$C_{D\ H} = \frac{\varepsilon\varepsilon_0}{x_2} \qquad (3.36)$$

where x_2 is comparable in size to the size of the solvated ions in the salt and is also the distance of closest approach between the charged particles and the solid surface. The second capacitor is composed of a diffusion layer of charge in solution, which is voltage and concentration dependent and has the form described by the Guy-Chapman differential capacitance given by (3.34). In this term ϕ_2 is the potential drop across the diffusion layer only. The total potential drop across the electrode ϕ is given by the sum of the potential drop across the Helmholtz layer and the diffusion layer of charge.

This new description solves the problems of the GC theory since the smallest of the two differential capacitances dominates the series. Thus, in the presence of a high salt concentration or high applied potentials, the differential capacitance is voltage independent and given by the Helmholtz differential capacitance $C_{D\ H}$. At low electrolyte concentrations and near the point of zero charge, $C_{D\ GCS}$ (Gouy-Chapman-Stern) is dominated by $C_{D\ GC}$

(Gouy-Chapman) as given by (3.37)

$$C_{D\ GC} = (2\varepsilon\varepsilon_0 z^2 q^2 n^0 / kT)^{1/2} \cosh(zq\phi_2 / 2kT) \tag{3.37}$$

which came from the Gouy-Chapman theory. In (3.37) the potential is the difference between the HL (Helmholtz layer) and the bulk of the electrolyte. Even though the SGC model does not take into account details regarding the electrode surface, the SGC model explains the shape of the curves of the double layer differential capacitance vs. the applied cell voltage. However, details of the electrode and electrolyte interface become necessary to explain double layer features like the reduction or oxidation peaks at different applied voltages in the differential capacitance curves.

If we consider the case of carbon nanotube electrodes at an applied potential of 0 V and using again a 1 mole/l $TEMA - BF_4$ in acetonitrile solvent, the differential capacitance of each electrode is given by

$$C_{D\ GCS} = (\frac{1}{C_{D\ H}} + \frac{1}{C_{D\ GC}})^{-1} \tag{3.38}$$

where $C_{D\ H} = \varepsilon\epsilon_0 / x_2 = 11$ μF/cm^2 and where for an applied zero potential $C_{D\ GC} = (2\varepsilon\varepsilon_0 z^2 q^2 n^0 / kT)^{1/2} \cosh(zq\phi_2 / 2kT) = 157$ μF/cm^2 and thus using (3.38), $C_{D\ GCS}$ is 11 μF/cm^2 which matches the experimental measurements shown is section 5.3.1.

3.5   Chapter Summary

In this chapter we presented the benefits and challenges associated with the use of carbon nanotube-based ultracapacitors. Then, our approach based on vertical carbon nanotube-based electrode was presented as a path to produce ultracapacitors having six time higher energy density and five times higher power density than activated carbon-based devices. We showed an analysis that justifies the capacitance and energy density expected with our target nanotube electrodes and we explained the current limitations to further energy density increases. Finally, the chapter reviewed the major contributions to the evolution of the understanding of the double layer of charge principle. The next chapter will explain the steps involved in the synthesis our nanotube electrodes and will point out the remaining challenges that still have to be overcome in order to produce our target electrodes.

Vertical Carbon Nanotube Array Fabrication and Morphological Characterization

The previous chapter discussed the features of our target carbon nanotube-based electrodes. This chapter focuses on the advances we have made in the fabrication of vertical carbon nanotube-based electrodes that approximate the ideal desired structure described and modeled in Chapter 3. This chapter begins by reviewing the thermodynamics that control the nanotube growth reaction and the formation of oxide material on the substrate, which as shown in Chapter 5 has an effect on the electrode measurements. The chapter then introduces the system that was designed and built, along with the synthesis procedure developed for the electrode fabrication. This chapter concludes by describing the morphological electrode characterization procedure.

4.1 Thermodynamics of Nanotube Growth

This section introduces the thermodynamics of nanotube growth given the gas mixture, substrate and catalyst, and temperature conditions used in our experimental apparatus. In this section the most thermodynamically stable phase of the catalyst, underlayer, and substrate, given the operating conditions, is identified. Moreover, the reaction of decomposition of the carbon feedstock to form nanotubes is proposed along with a calculation showing the large decrease in Gibbs free energy associated with this nanotube growth reaction. This indicates the particularly high thermodynamical drive associated with the decomposition of acetylene with an iron oxide catalyst to form carbon nanotubes.

4.1.1 Metallurgy of the Substrate

The understanding of the oxide metal present on the substrate is important to the interpretation of the electrode measurements described in Chapters 5 and 6.

As shown in section 4.2.1, most of our tests used a thin film of tungsten as the substrate for the growth of the carbon nanotube electrodes. Tungsten was chosen for its high melting temperature (3422°C) and for its relatively low electrical resistivity (5.5 $\mu\Omega \cdot$ cm), which at room temperature is approximately only three times higher than copper (1.75 $\mu\Omega \cdot$ cm). An exhaustive investigation of other suitable candidate substrate materials should be performed.

Our tests show that a 10 to 20 nm thin aluminum oxide underlayer and a nanometer thin

iron catalyst layer yield particularly good results with respect to the speed of growth of multiwall carbon nanotubes. We believe that the aluminum oxide underlayer promotes the nanotube growth reaction by preventing the coalescence of the iron catalyst on top of the aluminum oxide surface as shown by [16]. The issue associated with using aluminum oxide as an underlayer between the iron catalyst and the substrate is the high electrode resistance that the aluminum oxide introduces, which decreases the electrode power performance. To reduce this resistance while still yielding the growth of vertically aligned nanotubes, we replace the aluminum oxide underlayer with a 15 nm thin layer of deposited aluminum. After the deposition and prior to the nanotube growth we oxidize the surface of this aluminum layer at the aluminum iron interface. As described in this section, we believe that the oxidation process creates a layer of aluminum oxide that has an average thickness of a few Å, as indirectly shown in section 6.4.1. This thin aluminum oxide layer can prevent the coalescence of the iron catalyst during the nanotube growth, and it is thin enough to introduce an acceptably low resistance (which is lower than 0.5 Ω/cm^2, as shown indirectly in section 6.4.1, and which is much lower than that introduced by a 15 nm thick layer of aluminum oxide) between the nanotube and the substrate.

The air oxidation process, prior to the start of the reaction of carbon nanotube self assembly, takes place at approximately 200°C. This temperature was empirically selected by maximizing the speed of the nanotube growth reaction. The most likely iron phase present between room temperature and 700°C is Fe_3O_4. As shown by the Ellingham diagram[1] in

---

[1]Ellingham diagrams show the molar free energy of formation of a species as a function of temperature. It indicates therefore whether a reaction is thermodynamically favorable by showing whether its formation is associated with a decrease of Gibbs free energy (favorable) or with an increase in Gibbs free energy (unfa-

Fig. 4.1, the Gibbs free energy of formation of Fe_3O_4 is the lowest among the other iron

oxide species up to a temperature of 500°C, indicating that the reaction

$$3/2Fe + 1/2O_2 \longrightarrow Fe_3O_4 \tag{4.1}$$

is the most thermodynamically favorable reaction during the air oxidation treatment at

200°C. This and all the other oxide formation reactions are written for one mole of oxygen

reacting. Similarly, the superficial layer of aluminum in contact with the iron oxide layer

is oxidized into Al_2O_3, within milliseconds, which, as shown by the Ellingham diagram

in Fig. 4.2, is the most thermodynamically likely aluminum form within the operating

temperature range. Along the same reasoning, tungsten is likely to show a layer of tungsten

oxide WO_2, since as shown by Fig. 4.3, the free energy of formation of tungsten oxide is

negative. Figure 4.4 summarizes the free energy of formation of the different oxide forms of

deposited metals. The diagram shows comparable energies of formation for iron oxide and

tungsten oxide. Moreover, it shows a much lower energy of formation for aluminum oxide.

This justifies the much more stable nature of aluminum oxide versus other metal oxides.

The reaction energies of formation of the different oxide species are normalized with respect

to their oxygen molar content. This enables us to infer with a high degree of confidence the

likely metal oxide that is present on the substrate immediately prior to the CNT growth

reaction. In this case, the presence of an iron oxide Fe_3O_4 catalyst on top of an aluminum

oxide Al_2O_3 layer is very likely.

---

vorable). Concurrently, Ellingham diagrams indicate the most likely reactions among different alternatives by showing the reaction associated with the greater decrease in Gibbs free energy for a given temperature range.
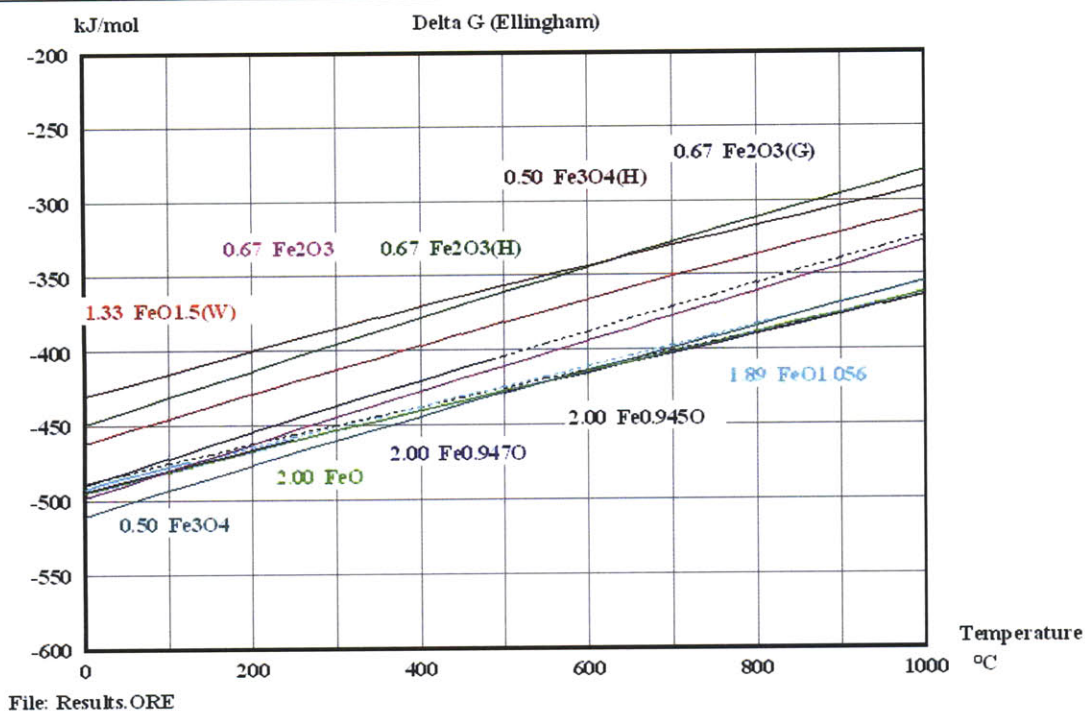
Figure 4.1: Ellingham diagram for iron oxides showing the Gibbs free energy per mole of reaction (as indicated in the diagram) associated with the formation of different iron oxide species as a function of temperature. The diagram clearly indicates Fe_3O_4 as the most thermodynamically likely iron oxide specie between room temperature and 500°C. The molar energies of the reaction of formation of the different oxide species are normalized with respect to the oxygen molar content and thus the different species shown all contain one mole of oxygen.

4.1.2   Nanotube Growth Reaction Thermodynamics

Given the most thermodynamically favorable states of the metal oxides prior to nanotube nucleation, the reaction (4.2) is thermodynamically favored to describe the decomposition of acetylene and the delivery of carbon to the surface of the iron containing particles, resulting in the formation of nanotubes. Table 4.1.2 shows the significant reduction in Gibbs free energy within the operating temperature range associated with the reaction leading
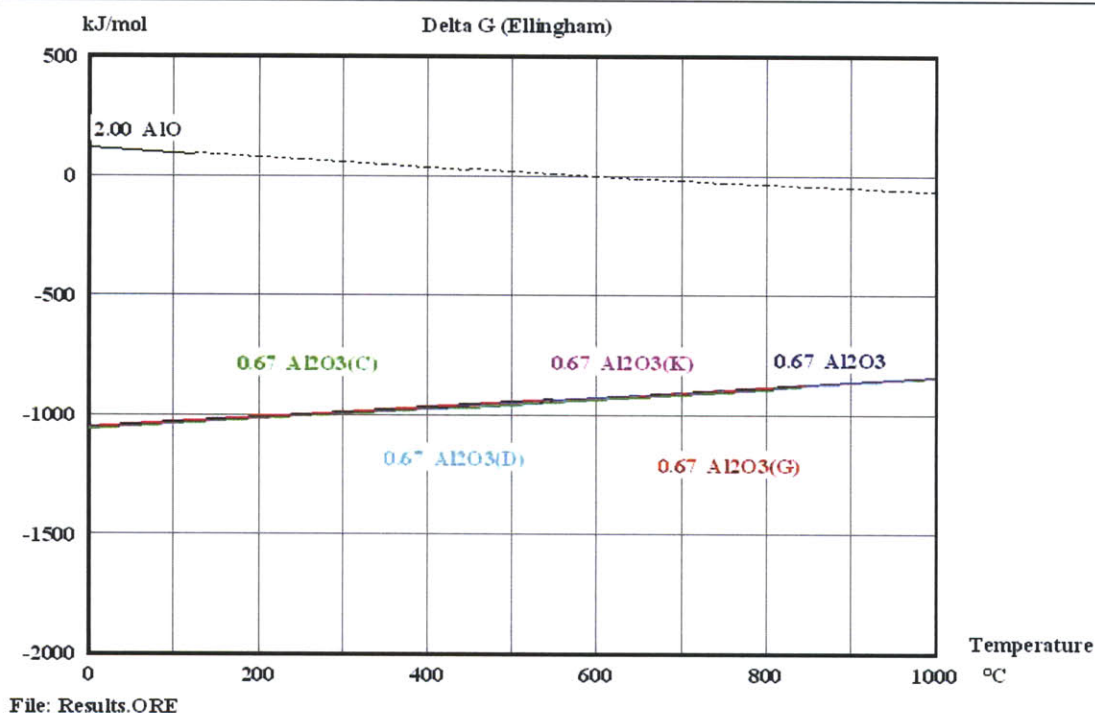
Figure 4.2: Ellingham diagram for aluminum oxides showing the Gibbs free energy per mole of reaction (as indicated in the diagram) associated with the formation of different aluminum oxide species as a function of temperature. The diagram clearly indicates Al_2O_3 as the most thermodynamically likely aluminum oxide specie independent of the temperature. The molar energies of the reaction of formation of the different oxide species are normalized with respect to the oxygen molar content and thus the different species shown all contain one mole of oxygen.

to the acetylene decomposition, and iron reduction. This indicate the particularly high

thermodynamical drive, associated with acetylene as the carbon feedstock (as to compared

with other hydrocarbon gases) and iron oxide as the catalyst, to promote the release of car-

bon to the nanotube growth reaction. The acetylene decomposition into carbon is essential

in that it delivers carbon that first nucleates and then supplies feedstock that continues to

support the growth of the carbon nanotubes. A more thermodynamically favorable reaction

typically result in a faster reaction rate, and thus in this case in a faster nanotube growth
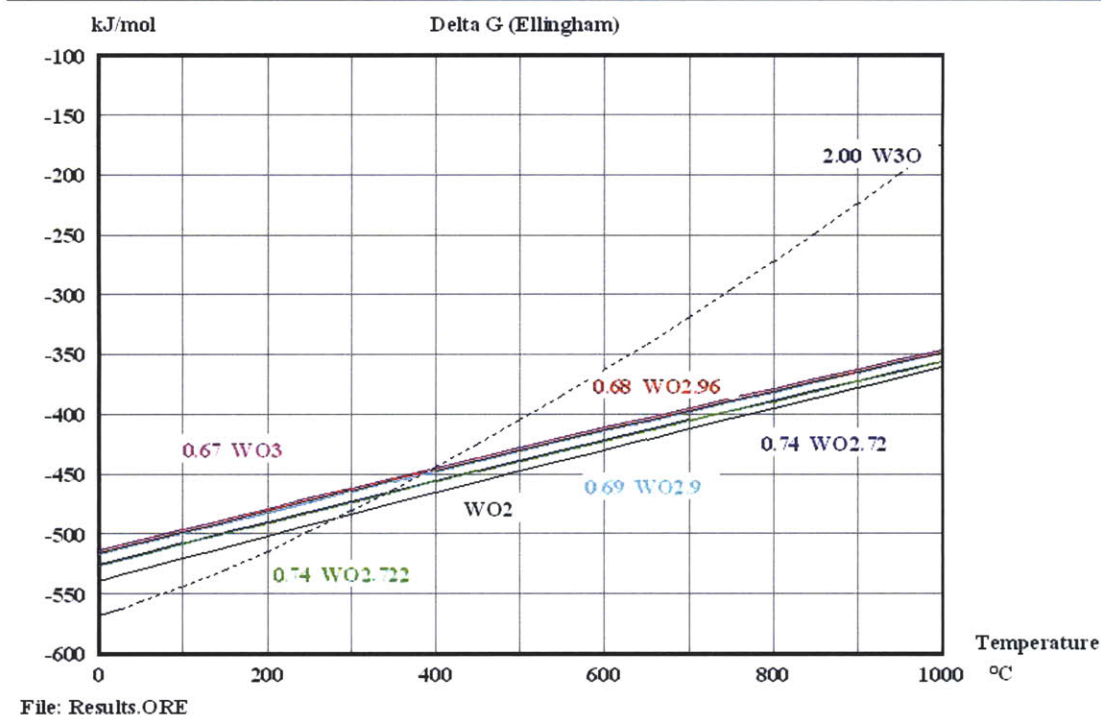
Figure 4.3: Ellingham diagram for tungsten oxides showing the Gibbs free energy per mole of reaction (as indicated in the diagram) associated with the formation of different tungsten oxide species as a function of temperature. The diagram clearly indicates WO_2 as the most thermodynamically likely tungsten oxide specie for temperatures higher than 300°C. The molar energies of the reaction of formation of the different oxide species are normalized with respect to the oxygen molar content and thus the different species shown all contain one mole of oxygen.

rate. The reaction indicated also shows water vapor as a byproduct of the iron reduction.

$$Fe_3O_4 + 3C_2H_2 \longrightarrow FeO + 2Fe + 3H_2O + 6C \tag{4.2}$$
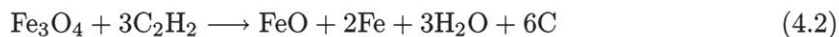
The metals that can be used as catalysts for the growth of nanotubes include iron, nickel, and cobalt. These metals can dissolve carbon from the acetylene decomposition and also, as shown by the Ellingham diagram in Fig. 4.5, these metals also form unstable carbides in
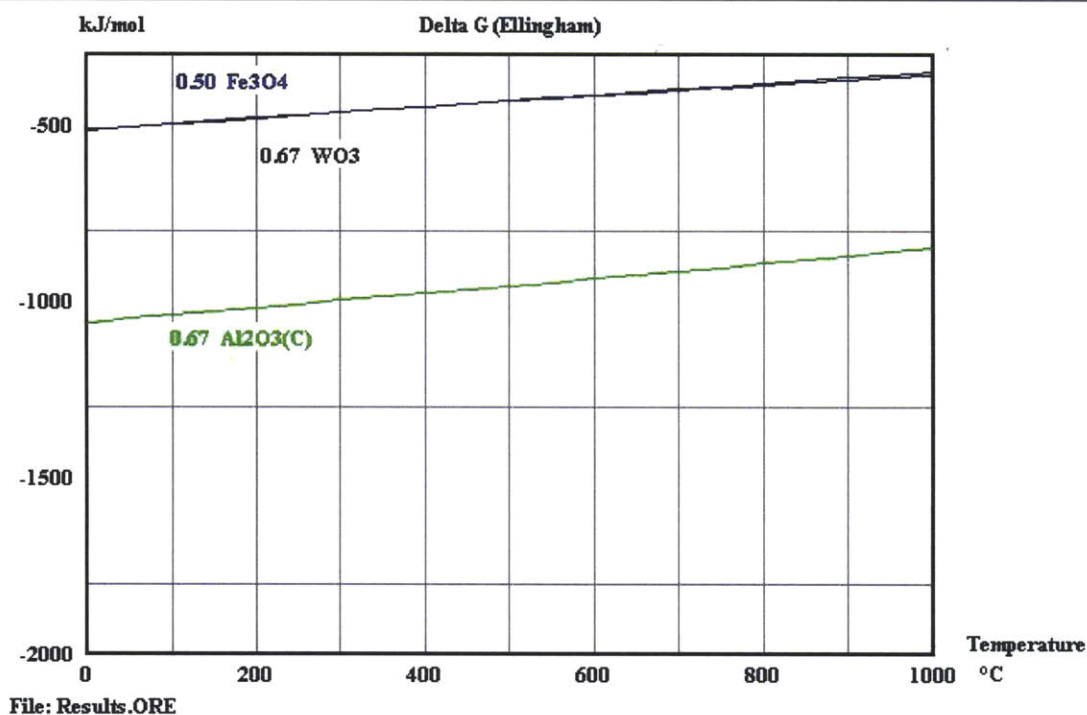
Figure 4.4: Ellingham diagram showing the molar Gibbs free energy of formation for the most likely metal oxides present on the substrate prior to the beginning of the reaction of nanotube growth. The molar energies of the reaction of formation of the different oxide species are normalized with respect to the oxygen molar content and thus the different species shown all contain one mole of oxygen.

the temperature range of interest (up to 700°C). Transition metals that form very stable carbides, such as titanium, would slow down or completely prevent the carbon release process and thus the nanotube growth reaction, whereas catalysts that do form unstable carbides, such as cobalt, nickel and iron, promote the release of the product, carbon, to continue the nanotube growth.

This section first discussed the most thermodynamically likely metal oxide materials present on a substrate underneath the nanotube film. These oxide materials are tungsten trioxide

Temperature T ($^\circ C$)	Free Energy ΔG (kJ/mole)
400	-527
500	-519
600	-510
700	-501
800	-491
900	-482

Table 4.1: Molar Gibbs free energy associated with Reaction 4.1.2 at different temperatures.

(WO_3) present on top of the tungsten substrate, alumina (Al_2O_3) occurring on top of the aluminum underlayer, and iron oxide (Fe_3O_4) within the catalyst.

This section then showed how this oxide materials might evolve during the most thermodynamically likely nanotube growth reaction. Finally, this section presents possible alternatives that could be used instead of iron as a catalyst for the growth of carbon nanotubes.
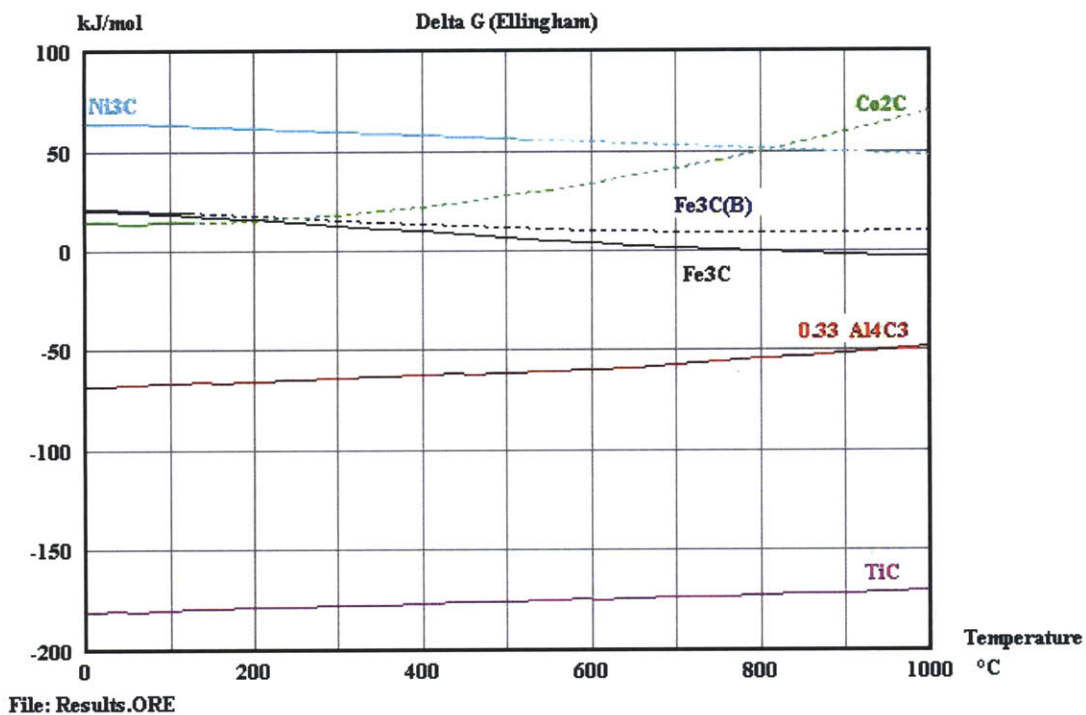
Figure 4.5: Ellingham diagram of the molar Gibbs free energy of formation of cobalt carbide, iron carbide, nickel carbide, aluminum carbide, titanium carbide. The diagram shows that nickel, cobalt and iron form unstable carbides for temperature up to 750°C, whereas aluminum and titanium form very stable carbides. The molar energies of the reactions of formation of the different carbide species are normalized with respect to the carbon molar content and thus the different species shown all contain one mole of carbon.

4.2 Vertical Carbon Nanotube-Based Electrode Fabrication

This section begins with the method that we have developed to deposit the underlayer and catalyst layers onto the substrate surface. It then discusses the procedure we that have developed to fabricate vertically aligned carbon nanotube electrodes via low pressure chemical vapor deposition (CVD). Finally, the section describes the small scale low pressure chemical vapor deposition reactor (LP-CVD) that we have designed and built to fabricate our nanotube electrodes.

4.2.1 Preparation of the Substrate and Catalyst

The first step in the electrode fabrication process is the preparation of conducting substrates. A variety of conducting substrate electrode materials including aluminum, tungsten, and platinum have been used. The processing steps that follow refer mostly to tungsten substrates.

A 99.9 % pure tungsten substrate (purchased from Alfa Aesar) that is 500 μm thick, 50 mm wide, and 100 mm long was used to fabricate the carbon nanotube-based double layer capacitor electrode. Once received, the substrate is cut into 10 mm by 10 mm squares using a diamond saw. The 1 cm^2 or 0.5 cm^2 pieces of substrate are then polished on one side. The polishing is performed using either a rough sandpaper procedure (RP) or a more fine chemical mechanical procedure (CMP). We have empirically observed that a smother substrate can significantly increase the achievable carbon nanotube density. Further investigation

is necessary to understand the relation between the substrate smoothness and the carbon nanotube density. Once the substrate is polished, it is cleaned using an ultrasonic bath of acetone and subsequently rinsed with methanol to remove any residues left by the acetone.

After cleaning, the substrate is ready for the underlayer and catalyst deposition that takes place via electron beam evaporation. Once the substrate is introduced into the e-beam evaporator, the background pressure of the chamber (p_c) is reduced to $3 \cdot 10^{-6}$ Torr. Before beginning the Al deposition onto the substrate, roughly 1000 Å of Al are evaporated from the source target. This is done to stabilize the evaporation rate of Al, and to remove the superficial layers of oxides present on the target. Once the chamber pressure returns to $3 \cdot 10^{-6}$ Torr, the shutter is opened and Al is deposited onto the substrate at a rate ranging from 1.0 Å/s to 1.9 Å/s. The deposition continues until the desired thickness is achieved (150 Å). The evaporation of the first metal layer, aluminum, begins at an evaporation rate ranging from 1.0 Å/s to 2.2 Å/s. Correspondingly, the pressure of the chamber abruptly rises to $7 \cdot 10^{-6}$ Torr due to oxygen and the moisture being evaporated from the top aluminum surface. Similarly, the catalyst, iron, is first evaporated, without being deposited onto the substrate. While the iron is initially evaporated, the adsorbed moisture and oxygen released into the chamber inevitably oxidizes the top layer of Al. Once the chamber pressure stabilizes and the Fe evaporation rate is stabilized between $0.3 - 0.8$ Å/s, the shutter is opened and the Fe is deposited on top of the naturally occurring aluminum oxide on the aluminum substrate to achieve the desired iron thickness of 10 to 15 Å.

4.2.2   The Chemical Vapor Deposition System

Our custom LP-CVD system is composed of four main components - the reaction chamber, the low pressure piping and fittings, the infrared temperature measurement system and control, and the gas mixing system.

The reactor chamber, which is shown by Fig. 4.6, encloses the heater, on which the substrate is placed during the growth of the vertical carbon nanotube layer. The chamber is composed
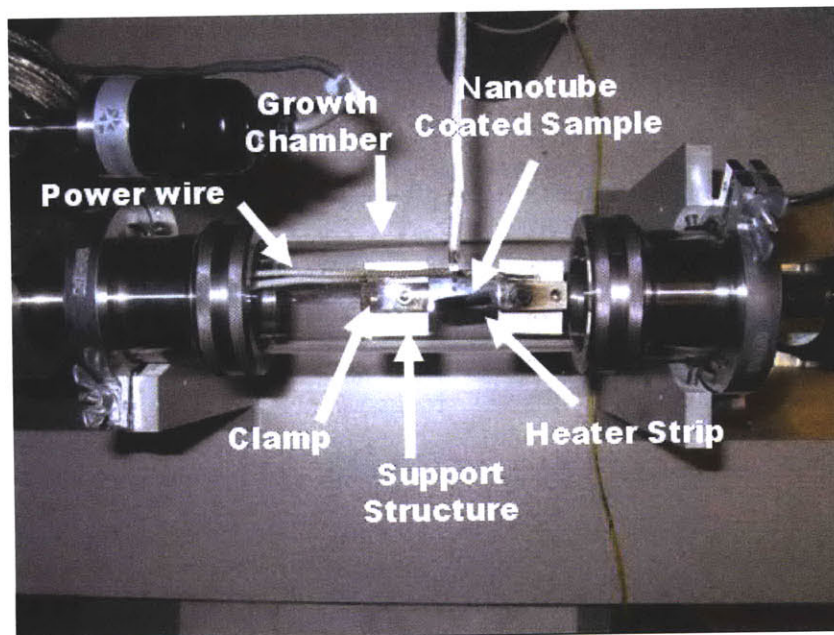
Figure 4.6: CNT Fabrication Chamber.

of a quartz tube having an ID of 46 mm, an OD of 50 mm and a length of 200 mm. The inlet and outlet gas lines are connected to the quartz tube using stainless steel MDC NW-50 "ultra-torr-quick-connects", which are rated for vacuum levels as low as 10^{-6} Torr.

The heating system is an extrinsic p-type silicon strip 10 mm wide and 25 mm long used

as a resistive heating element. Silicon heating elements have been previously used for the growth of CNT by [19]. The structure supporting the heating element is made of stainless steel clamps. The support for the entire heater is made of a Maycor® plate 20 mm wide and 60 mm long and 5 mm thick. A three strand nickel wire is used to electrically connect the heater to the vacuum feed-troughs. The wires are electrically isolated with alumina flexible tubing from Omega-Vacuum. The temperature of the heater is measured using an infrared pyrometer from Gentech.

Before beginning the CNT growth, the background pressure of the chamber is reduced to 5 mTorr. This background pressure level is sufficiently low to ensure a low level of contamination from ambient gases during growth. The chemical vapor deposition takes place at a pressure of about 30 Torr. The roughing vacuum pump used is an Eduard-BOC 80 lubricated with Fomblin® oil. The vacuum pump is connected to the growth chamber using two stainless steel vacuum lines. The rough vacuum line is composed of stainless steel tubes with an inner diameter of 1.5 inches, and it is used to rapidly evacuate the growth chamber. The fine vacuum line is composed of stainless steel tubes with an inner diameter of approximately 1/4 in, and it is used to maintain a constant chamber pressure during the growth. Flexible tubes are used in both vacuum lines to prevent the transmission of vibration from the vacuum pump to the growth chamber.

The gases used for the growth reaction are industrial grade argon, hydrogen, and acetylene. The gases are mixed prior to flow through the reaction chamber and the flow of each gas is controlled using mass flow controllers by Unit™. The gas flows and the temperature of

the heater are controlled via a feed-back control loop in real time.

4.2.3   Vertical Carbon Nanotube Synthesis

This subsection discusses our synthesis procedure for the growth of nanotubes on a conducting tungsten substrate coated with a deposited underlayer of aluminum and iron oxide catalyst. The temperatures and pressures involved of each step as well as the different steps used in the nanotube growth reaction are a result of an optimization process that lasted several years. Moreover, before using the combination of substrate, underlayer, and catalyst materials here discussed we have experimented a wide variety of conducting and non conducting substrate, underlayer, and catalyst materials.

After being coated with catalyst, the substrate is ready for the fabrication of the nanotube active layer. The process is divided into four steps - catalyst pre-heating, catalyst oxidation and vacuum annealing, nanotube nucleation and growth, and finally, shut down and sample extraction. To ensure repeatable conditions among the various experiments, the substrate is placed on the heater with the heater at a temperature of 150°C in an ambient air environment. After the sample is placed onto the heater, the temperature is raised to 200°C. The substrate is held at this temperature for up to 5 min in an ambient air environment, resulting in the oxidation of a superficial layer of iron and aluminum. Subsequently, the reaction chamber is evacuated to a pressure lower than 5 mTorr within 30 s. Once the pressure of the growth chamber is lower than 5 mTorr, the temperature is held at a value ranging from 300°C to 400°C. No appreciable difference has been noted in results using

temperatures within this range.

After the oxidation and annealing of the sample, argon, hydrogen, and acetylene are flowed through the reaction chamber while the heater is at room temperature. The flow rates of argon, hydrogen, and acetylene are 696 sccm, 90 sccm, 30 sccm, respectively. Once the gas flow stabilizes, the pressure of the chamber is increased from 500 mTorr to 30 Torr over 30 s. Subsequently, the temperature of the system is increased from 400°C to 675°C over a period of 5 min. The nucleation of carbon nanotubes abruptly starts once the heater reaches a temperature between 640°C and 670°C, and while the chamber pressure is 30 Torr. The partial pressures and relative concentrations of the gases during the nucleation and growth of the carbon nanotubes are 25.59 Torr (85.3 %) for argon, 3.31 Torr (11 %) for hydrogen, and 1.1 Torr (3.7 %) for acetylene.

For nanotube lengths up to 400 μm and given the growth conditions, the duration of the nanotube growth is selected according to the desired thickness of the nanotube film. Once the desired thickness (or height) of the nanotube active layer is achieved, the growth reaction is terminated by interrupting the flow of acetylene and hydrogen, reducing the pressure of the chamber to 500 mTorr, and lowering the temperature of the heater to 250°C. Once the growth chamber is filled with argon and the temperature of the heater is lower than 200°C, the sample is extracted from the reactor.

4.3   Electrode Morphology

This section describes the techniques used to characterize the nanotube electrodes with respect to the density of nanotubes, the thickness of the nanotube active layer, and the average nanotube diameter and number of walls. Currently, electrodes with target nanotube thicknesses between 20 μm and 200 μm, and target number of walls between 3 and 7 walls have been fabricated. The remaining challenge consists of improving the nanotube electrode density from its current value of $2.6 \cdot 10^{11}$ cm^{-2} to the target goal of 10^{12} cm^{-2}. One of the future tasks of the research is to investigate the effect that the nanotube quality (i.e. amorphous carbon vs. nanotube ratio) has on the electrode performance (affecting parameters such as the differential capacitance and the electrode resistance).

4.3.1   Vertical Carbon Nanotube Structure

Figure 4.7 shows a nanotube active layer that has a thicknesses of 150 μm. The sample was fabricated on a tungsten (W) substrate roughly polished and subsequently coated with 15 nm of aluminum (Al) and 1.5 nm of Iron (Fe), as described in section 4.2.1. After the underlayer and catalyst deposition, the nanotube film was-grown using the growth process detailed in section 4.2.3. One of the future tasks of this research is the characterization of the effect of the residual iron catalyst on the leakage current and maximum rated voltage of these carbon nanotube electrodes packaged in an ultracapacitor cell. Control of the variation of the CNT active layer thickness was achieved by varying the time during which acetylene was flowing into the reaction chamber. The diameter and number of walls of the
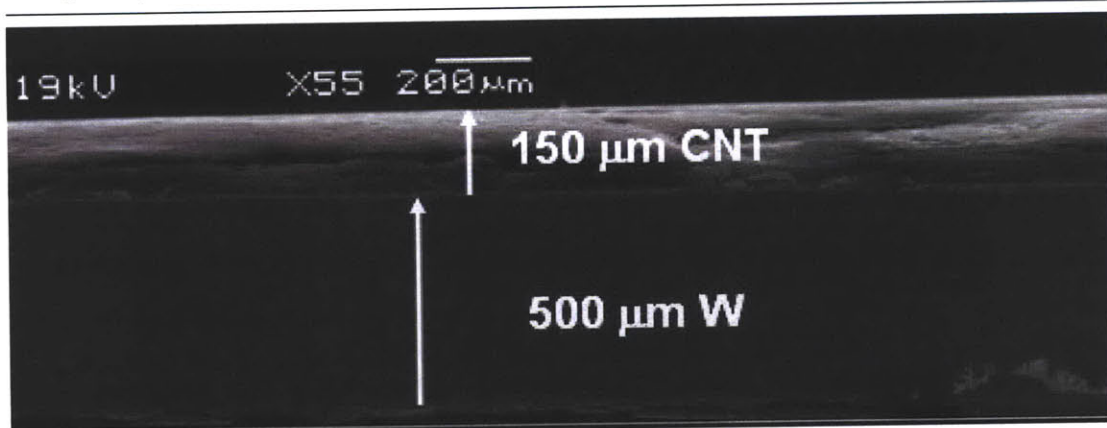
Figure 4.7: Scanning Electron micrograph of the edge of sample 031708-3 showing the 150 μm thick CNT active layer on top of the 500 μm thick tungsten substrate. The picture was acquired using a JEOL 5910 SEM viewing the sample placed vertically onto the SEM stage.

CNTs from different samples were measured using a HR-TEM JEOL 2010 instrument. After imaging, the average diameter and number of walls were estimated as 6.5 nm and 6 walls, respectively. Figure 4.8 shows HR-TEM illustrations of nanotubes collected from sample 042208-4. The nanotube imaged in Fig. 4.8 shows some areas in which defects and deposits (likely amorphous carbon) are present on the nanotube. Important future investigation in this research will be to identify the effect of defects on the differential capacitance of the electrode. Moreover, Fig. 4.8 shows a nanotube inner and outer diameter which are 4.4 nm and 10.4 nm, respectively. We are only seeking to use the external surface of the nanotube for the double layer capacitor effect, though we might later seek to "treat" this surface. The reason for this is that the inner nanotube is too small to allow penetration of solvated ions. Similarly, since the spacing between nanotube walls is only 0.34 nm, we are not trying to use the area between nanotube walls to increase the surface area and thus the capacitance of the electrode. The typical CNT density achieved with roughly polished W substrates

coated with Al and Fe as described in section 4.3.2 is $5 \cdot 10^{10}$ cm^{-2}. This value is calculated

using the average CNT diameter, length, number of walls per tube, and the weight of the

CNT active layer as described in the next section. Morphological data for sample 042208-4

is summarized in Table 4.2 and compared with the desired parameter values described in

section 3.3.

Symbol	Parameter Name	Example	Target Value
A_E	Electrode area	1 cm^2	1 cm^2
W_C	CNT film weight	0.4 mg	3.6 mg
t_C	CNT film length	80 μm	80 μm
d_C	CNT average diameter	6.5 nm	6.5 nm
NW_C	CNT average number of walls	6	3
A_{TOT}	CNT film surface area	0.09 m^2	1.63 m^2
ρ_C	CNT calculated density	$5 \cdot 10^{10}$ cm^{-2}	10^{12} cm^{-2}
D_C	CNT average spacing	50 nm	10 nm

Table 4.2: Morphological information of sample 042208-4 compared with target values.
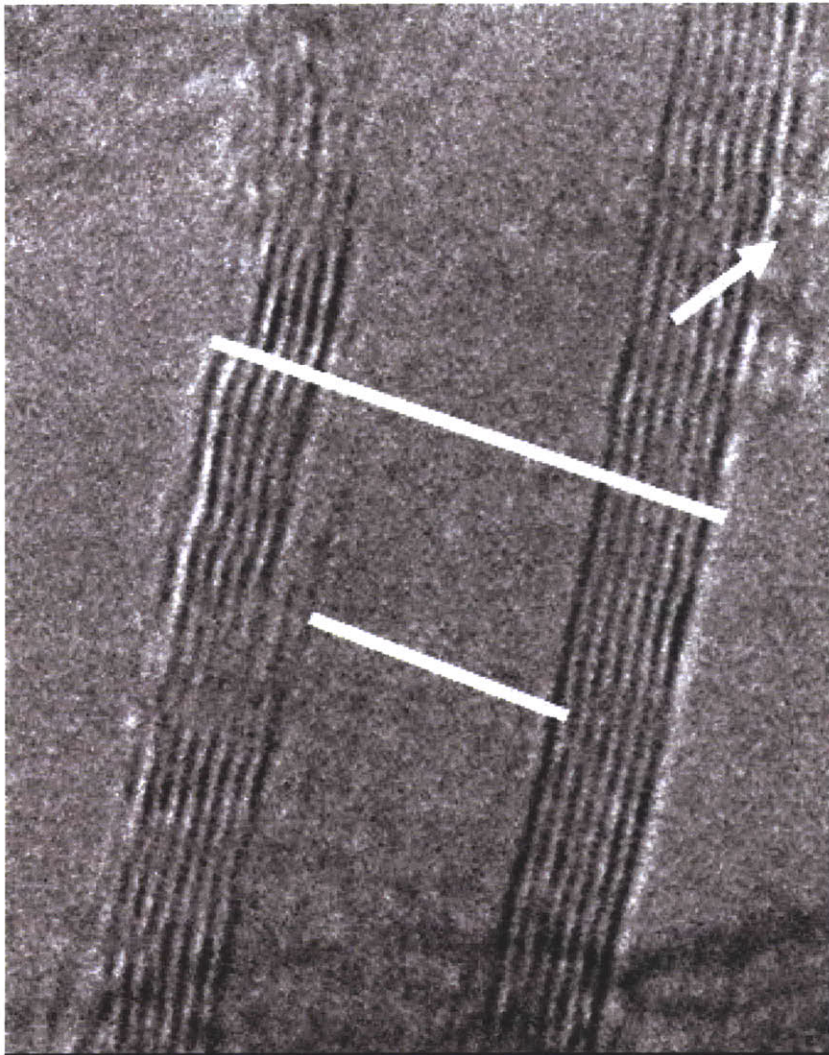
Figure 4.8: HR-TEM micrograph of a 7 wall nanotube from sample 042208-4. The nanotube OD is 10.4 nm and the nanotube ID is 4.4 nm. The arrow indicates carbon material on the nanotube surface. The picture was acquired using a JEOL TEM 2010 while imaging nanotubes that had been dispersed on a copper TEM grid coated with amorphous carbon.

4.3.2 Density Analysis Procedure

The density of the carbon nanotube active layer is determined in two ways, which can then be compared to corroborate the results. The first method relies on the measurement of the weight and thickness of the nanotube active layer grown on the substrate, and on the measurement of the average diameter and number of walls of the nanotube comprising the active layer. From the morphology of the active layer, the CNT density ρ_C can be estimated as

$$\rho_C = \frac{1342}{NW_C \cdot \pi \cdot d_C \cdot t_C} \cdot W_C \tag{4.3}$$

Table 4.3.1 defines the parameters and provides the morphological characteristics of a 1 cm^2 CNT substrates and (4.3) is applied to estimate the average CNT density.

The second method relies on the measurement of the density of holes left in the substrate from the nanotube removal, once the nanotubes are removed from the substrate by sonication. By imaging the substrate, via HR-SEM and AFM, after the removal via sonication of the nanotubes, we have observed that holes are left in the original locations. By imaging the density of these holes we then have an indirect measurement of the original density of the carbon nanotubes.

Figure 4.9 shows an atomic force microgram of the substrate from the sample 042208-4 after the nanotube removal. Figure 4.9 clearly shows the location of the holes which are indicated by the white arrows. By dividing the number of holes by the area of the picture a density of approximately $5 \cdot 10^{10}$ cm^{-2} nanotubes is calculated. This nanotube density
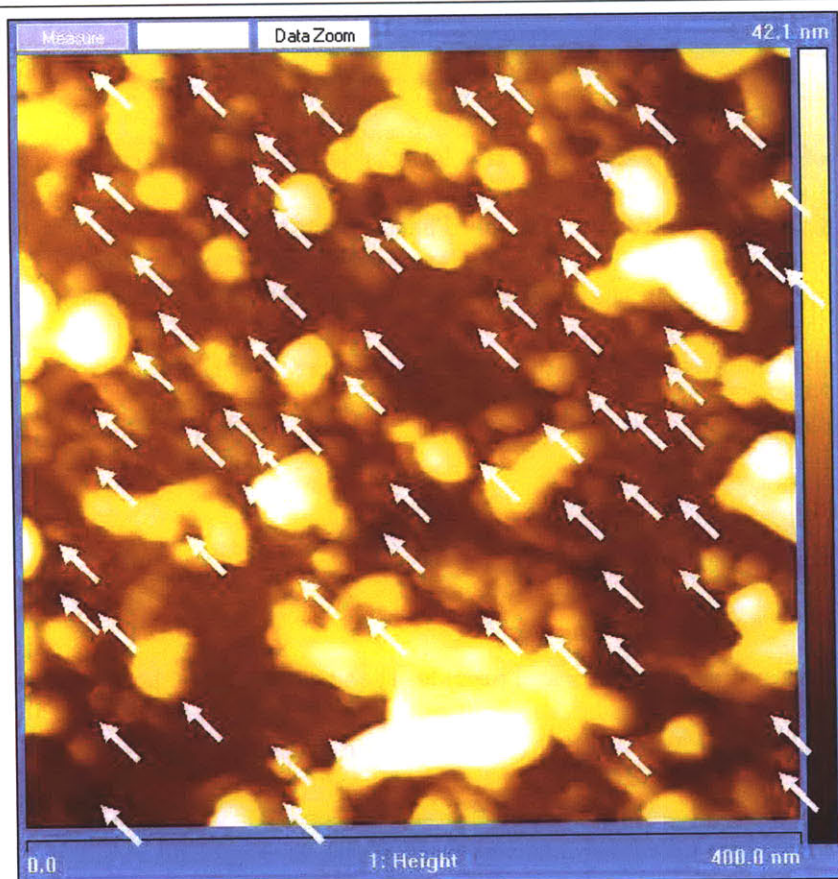
Figure 4.9: AFM micrographs showing a tungsten substrate where holes are left from the removal of nanotubes by sonication. The white arrows indicate the location of the holes left from the nanotube removal process.

corresponds to the density calculated via the morphological characterization of the nanotube

film. Figure 4.10 magnifies a region of Fig. 4.9 in which four holes are identified by the white

circles. These holes have a diameter of approximately 10 nm. In order to corroborate the

hole density measurement via atomic force microscopy, the same substrate is also imaged

via high resolution SEM. Figure 4.11 show the holes left in the substrate surface after

removal of nanotubes for the same sample described in Table 4.3.1 and imaged by AFM.

The same nanotube and hole density reported in Table 4.3.1 is measured by analysis of the
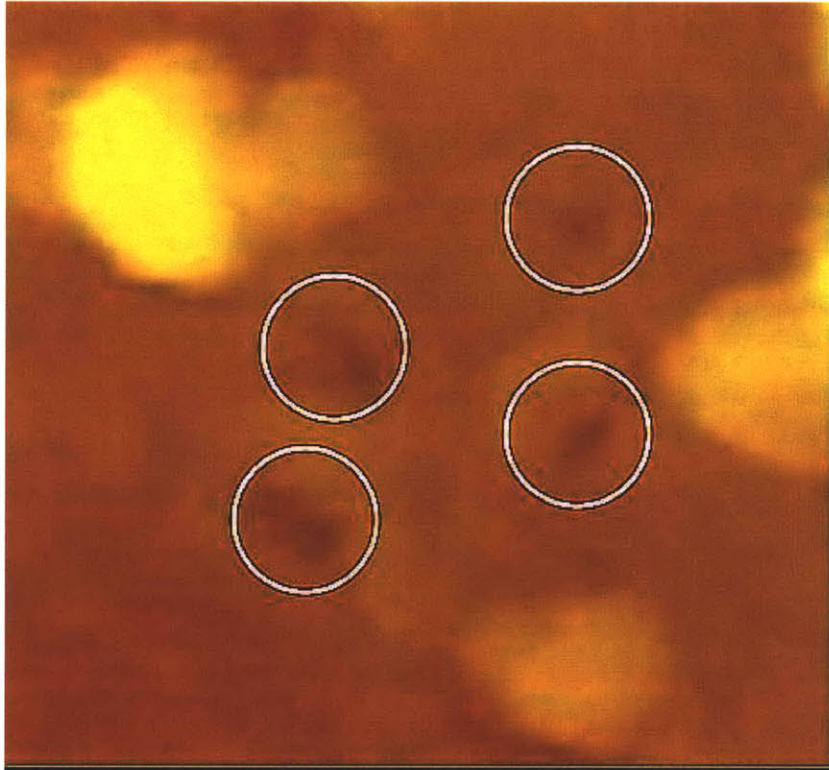
Figure 4.10: AFM micrographs showing a magnification of a region of Fig. 4.9. The figure shows four holes indicated by the white circles.

hole density via SEM. That is, $5 \cdot 10^{10}$ cm^{-2} nanotubes.

4.4   Chapter Summary

This chapter analyzes the thermodynamics of the growth procedure and the metal oxide materials present on the substrate. The chapter then describes the system that was designed and built, along with the synthesis procedure defined to fabricate carbon nanotube electrodes directly on thin tungsten and aluminum substrates. Currently, the nanotubes in the electrode active layers have a density ranging from 10^{10} cm^{-2} up to $2.6 \cdot 10^{11}$ cm^{-2}.
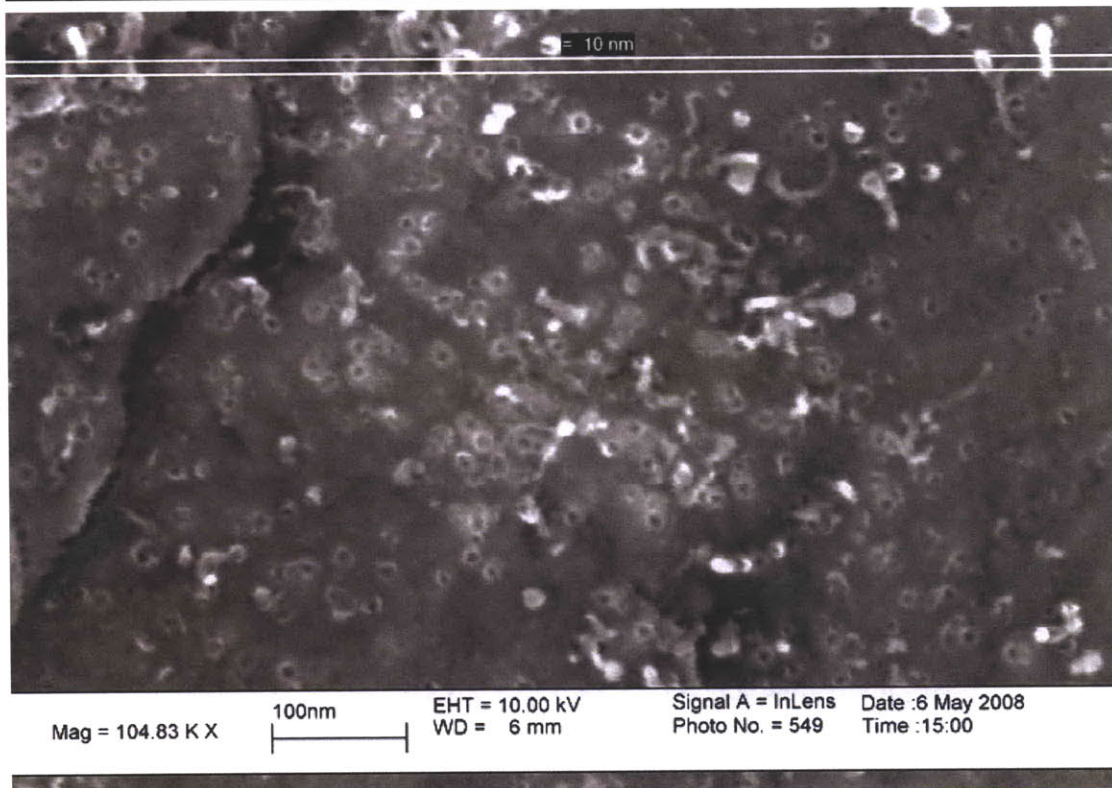
Figure 4.11: SEM micrographs showing a tungsten substrates where holes are left from the removal by sonication of nanotubes. The picture was acquired using a Reith HR-SEM.

One of the remaining fabrication challenges is to further improve this density to reach our target value of 10^{12} cm^{-2}. This chapter concludes by describing two methods to quantify the density of carbon nanotubes in the electrodes. The next chapter will first describe how to package the carbon nanotube electrodes, which this chapter showed how to fabricate, into an experimental ultracapacitor cell. The next chapter will then show how to use this cell to perform capacitance measurements that corroborate the capacitance modelling described in the previous chapter.

Chapter 5

Capacitance Measurements and Energy

Density Extrapolation

This chapter describes the preparation of an electrochemical cell that packages the nanotube electrodes that the previous chapter showed how to fabricate. This chapter shows the procedure used for measuring the cell and electrode capacitance, and predicts the energy density for a packaged CNT cell. Finally, this chapter discusses the good agreement between the capacitance modelling and measurements for our nanotube electrodes.

5.1   Electrochemical Cell Preparation

In this section we describe the assembly of the double layer capacitor cell used for the electrochemical characterization of our electrodes. This section describes the components of our electrochemical cell as well as the cell assembly steps. Finally, the limitations that the cell structure and material impose on the measurements are described. Figure 5.1 shows the schematic of our cell, purchased from Oshen, a supplier of electrochemical testing equipment,
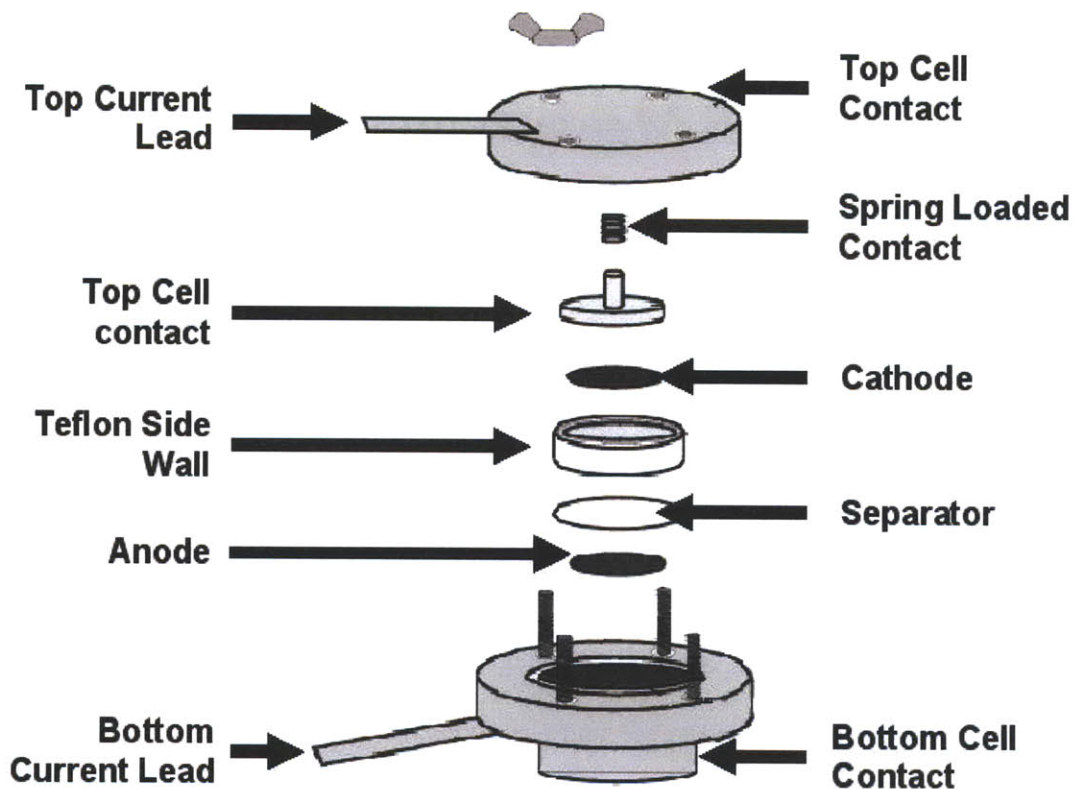
Figure 5.1: Schematic of the cell assembly used for the electrode measurements described in this chapter and in Chapter 6.

in which a cathode, a separator, and an anode are stacked. The cell casing is made of 304 stainless steel, teflon, and viton parts. Either carbon nanotube-based electrodes or activated carbon-based electrodes having a size of 1 cm^2 are used as the cathode and anode. A three layer stack of commercial NipponChemicon® ultracapacitor paper is used as the separator. Three layers of paper separator are used to prevent possible short circuits created by the nanotubes. As Fig. 5.1 shows, a spring loaded contact applies pressure to the cathode, separator, and anode stack. A teflon cylindrical side wall is used to align the cathode and anode to insure the overlapping of the two electrodes and to prevent short circuits through

the cell side walls. Finally, the assembly is enclosed by a top and a bottom contact which hermetically seal the cell to prevent infiltration of air from the environment. One molar tetramethylammonium tetrafluoroborate (TEMA $-$ BF$_4$) salt in acetonitrile solvent is used as the electrolyte. The electrolyte impregnates the electrodes and fills the cell void volume. The assembly procedure used to impregnate the electrodes with electrolyte and package the
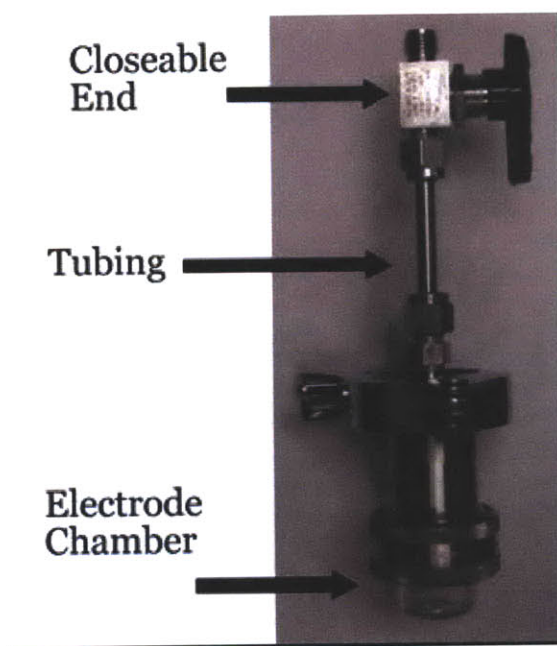
Figure 5.2: Illustration of the chamber used to dry the electrodes.

cell must extract any adsorbed moisture prior to the introduction of electrolyte, and ensure complete penetration of the electrolyte within the void volume of the electrode. First, the electrodes are placed inside of the chamber shown in Fig. 5.2 and placed under vacuum at room temperature for a minimum of twenty four hours to dry. After the twenty-four hour drying process, the valve in the filler tube is closed and the closed chamber is placed inside an argon filled glove box. Argon is used because it is an inert gas, other inert gases could

be used instead of argon to fill the glove box. Inside of the glove box the chamber tubing is connected to a reservoir of electrolyte and the valve is opened and the chamber containing the electrodes under vacuum is flooded with electrolyte. Prior to the electrolyte flooding of the electrodes, it is important to keep the electrodes under vacuum in order to minimize their intake of argon, which would prevent good penetration of the electrolyte into the voids of the nanotube active layer. Once the electrodes are impregnated with electrolyte, they are removed from the cell in Fig. 5.2 and rapidly placed into the cell in Figs. 5.3 and 5.4, which show the cell components.
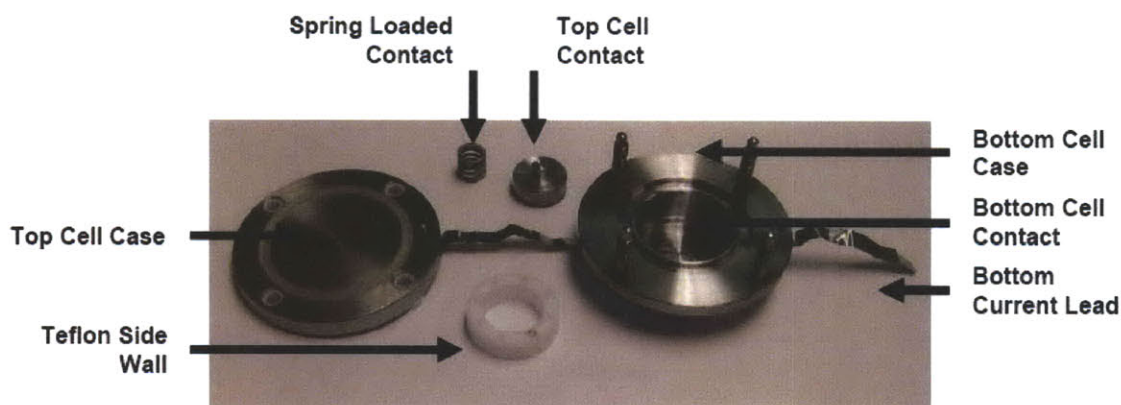
Figure 5.3: Tilted view of the components used in the electrochemical test cell.

First the cell is filled with acetonitrile, then the anode is placed at the bottom of the cell, then three separator layers are placed on top of the anode, and then the cathode is placed on top of the separator layer. The cell is finally sealed according to the schematic in Fig. 5.1.

In order to characterize the interference introduced in the electrode measurements by the stainless steel cell package itself, a cyclic voltammetry measurement was performed on the cell without the carbon electrodes. The anode and cathode were constituted by the top and
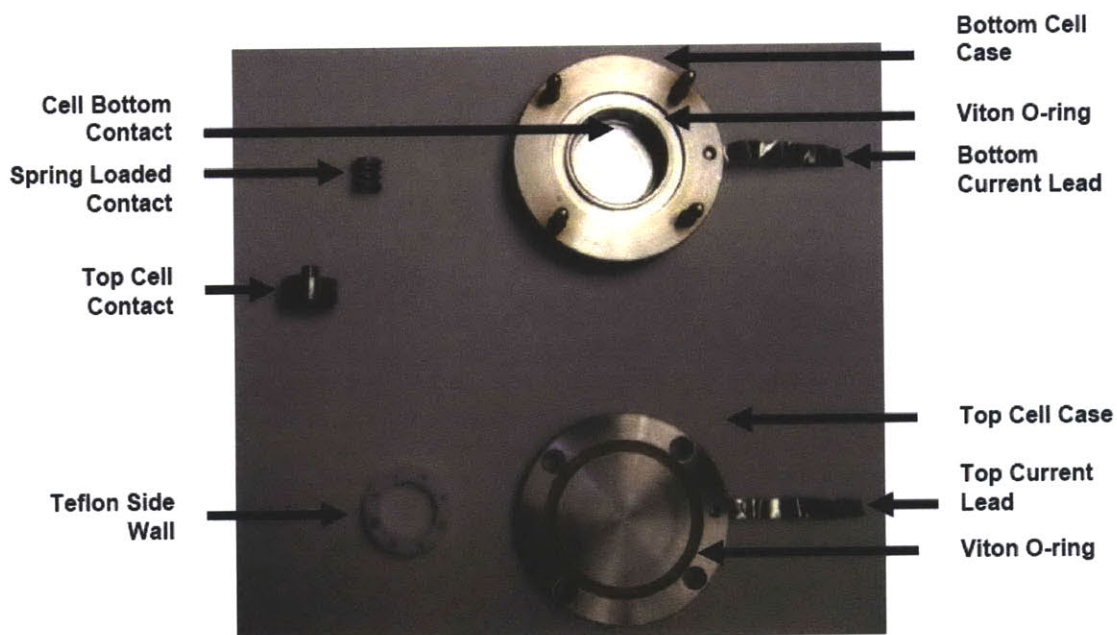
Figure 5.4: Top view of the components used in the electrochemical test cell.

bottom contacts of the cell, without any active electrode material. Figure 5.5 shows that the cell exhibits a Faradaic current, which is clear from the fact that for a constant scan rate of 50 mV/s a current that increases with increasing voltage is observed. In particular, a rapid increase in the charging current is observed, for a voltage greater than 2.5 V. For an applied bias less than $+/- 0.5$ V the Faradaic current due to the cell package is small $(+/- 30 \mu A)$ compared to the double layer current, as will be shown in sections 5.2 and 5.3.1. To minimize the Faradaic current introduced by the cell package to the electrode measurements, the applied voltage was kept below 0.5 V during electrode testing.
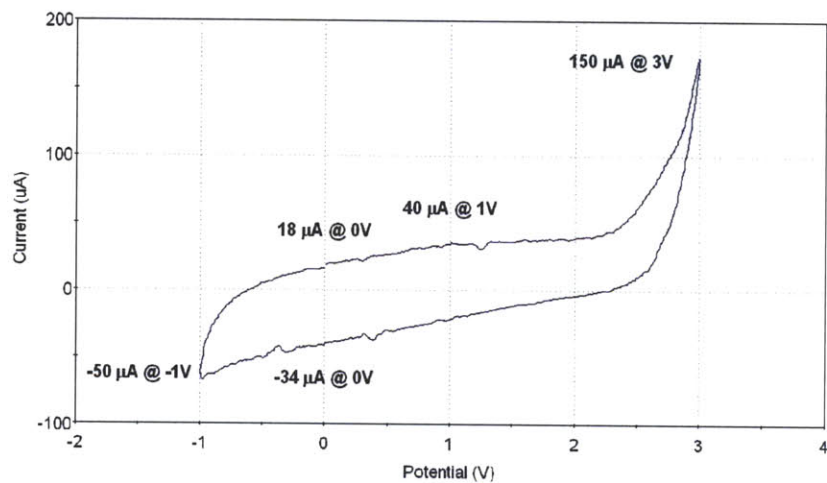
Figure 5.5: Cyclic Voltammogram characterizing the background current introduced by the stainless steel cell package. The measurements is performed using a scan rate of 50 mV/s.

5.2   Baseline Measurement of Activated Carbon Performance

This section reports the performance of a double layer capacitor cell packaged with 1 cm^2 activated carbon electrodes. The cell and the procedure used for the cell assembly is described in section 5.1. The purpose of measuring activated carbon electrodes is to establish a baseline for comparing the performance of carbon nanotube based electrodes and activated carbon-based electrodes packaged using the same procedure and the same components.

5.2.1   Activated Carbon Electrode Description

The activated carbon-based cathode and anode used for the measurements have an identical shape and morphology and were acquired from Maxwell Technologies®. Each has a Euclidean area of 1 cm^2. Their electrode active layers are made of activated carbon and have a thickness of approximately $130 - 135$ μm, and their charge collectors are made of aluminum with a thickness of $25 - 30$ μm. Figure 5.6 shows a comprehensive image of the charge collector and the active layer. As shown by Fig. 5.7, the carbon active layer is composed of activated carbon particles having a size ranging from 2 to 10 μm. The carbon particles are held together by a teflon based binder.

Activated Carbon Active Layer

Electrode Charge Collector
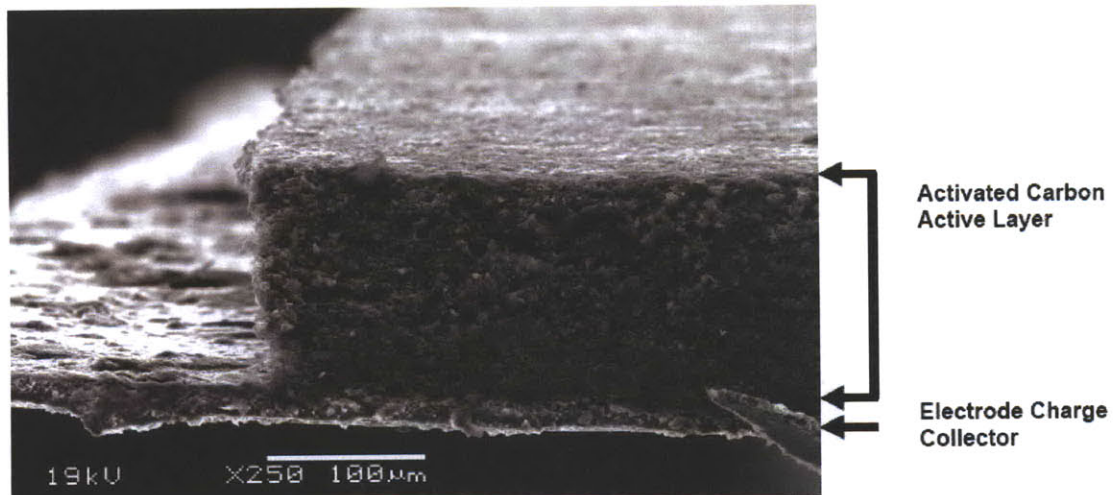
Figure 5.6: Scanning electron micrograph showing the cross section of a commercial activated carbon-based electrode in which an aluminum charge collector is covered by the activated carbon active layer.
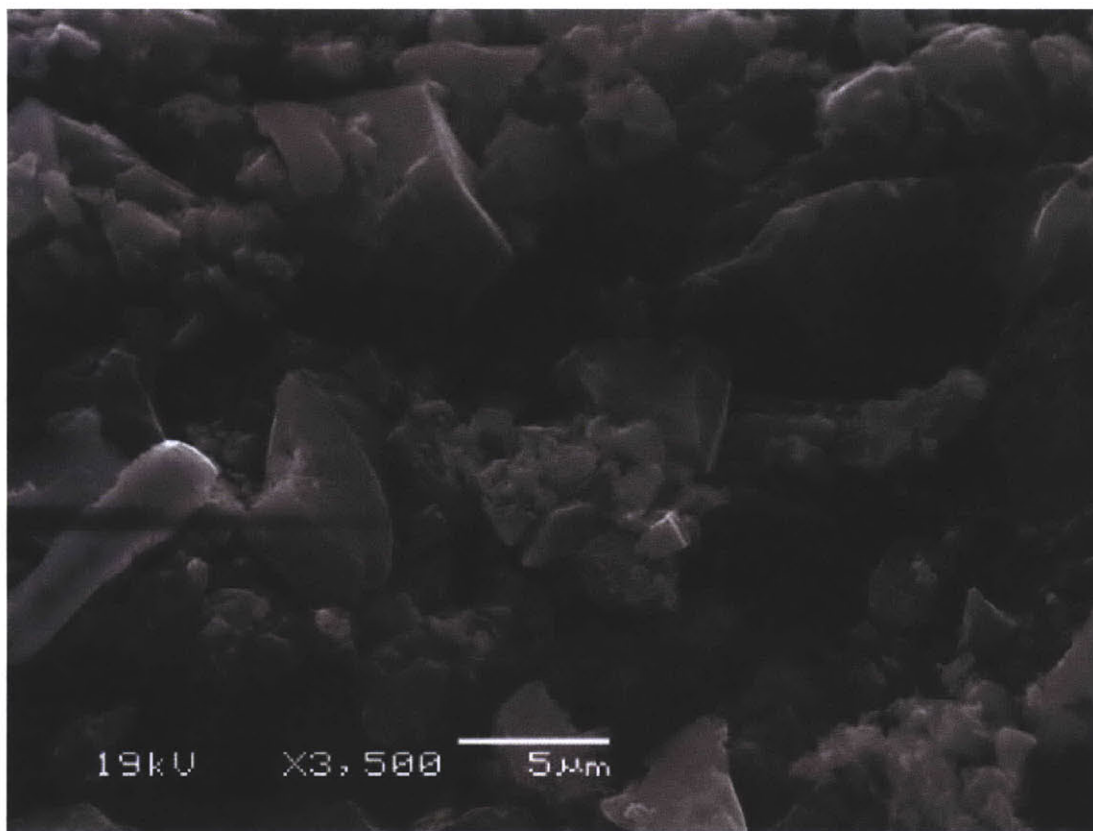
Figure 5.7: Scanning electron micrograph showing activated carbon particles forming the electrode active layer. The activated carbon particles in the picture have sizes ranging from 5 to 15 μm. The picture was acquired using a JEOL 5910 SEM viewing the sample placed vertically onto the SEM stage.

5.2.2   Activated Carbon Measurements

The test cell that incorporates activated carbon electrodes is assembled according to the procedure described in section 5.1, and a one molar tetramethylammonium tetrafluoroborate (TEMA $-$ BF$_4$) salt in acetonitrile solvent is used as the electrolyte. Three sheets of NipponChemicon^{TM} paper are used as the separator.

Figure 5.8 shows how the cyclic voltammograms of the activated carbon electrodes for different scan rates deviate from the expected square shape of an ideal double layer capacitor cell. The deviation from the ideal shape is accentuated for faster scan rates and it is indicative of a slow RC time constant for the cell. To accurately measure the cell capacitance, an impedance spectrum analysis is used. Figures 5.9 and 5.10 show the impedance spectroscopy of the activated carbon-based cell represented by a Nyquist and Bode plot, respectively. Figure 5.9 shows an equivalent series resistance of 1 Ω. From a frequency of 160 kHz to 160 Hz the Nyquist plot shows a high frequency semicircle, which increases the series resistance of the cell due to the interfacial resistive layer between the active layer and the charge collector. A comprehensive explanation of this is in Chapter 6. From the knee frequency of 160 Hz to the frequency of 0.8 Hz the Nyquist plot shows a 45° sloped line, which is due to the distributed resistance and capacitance in the activated carbon pores. For frequencies lower than 0.6 Hz the impedance starts increasing at a phase angle tending toward the 90° phase angle characteristic of an ideal capacitor. The 3 dB bandwidth of the double layer capacitor cell based on this activated carbon electrodes is of 0.2 Hz. Figure 5.11 shows an accurate measurement of the cell capacitance as a function of frequency,
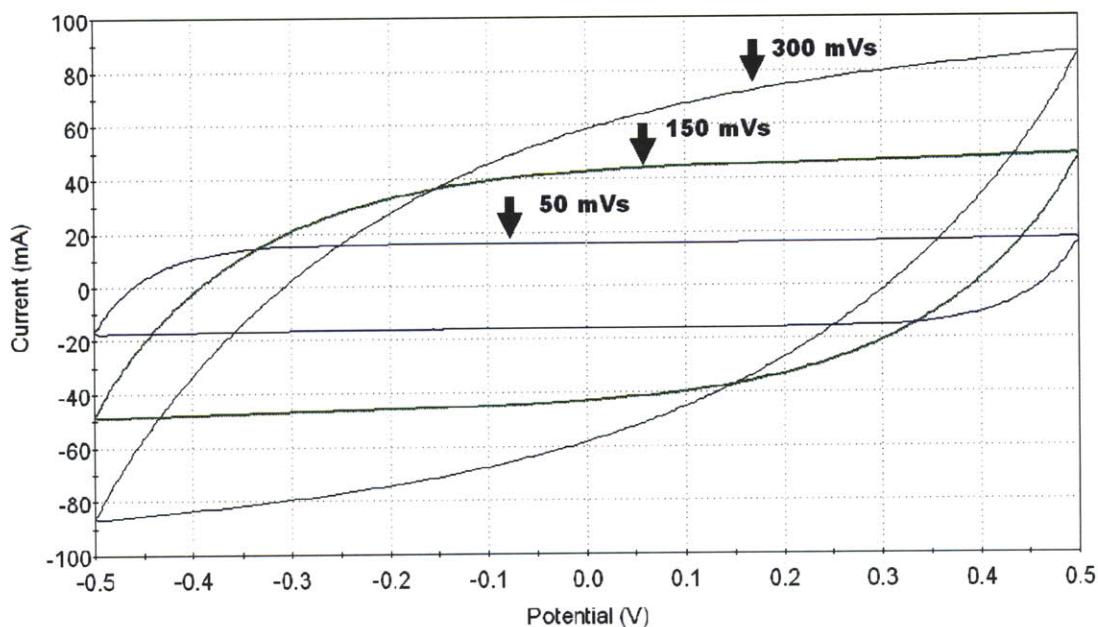
Figure 5.8: Cyclic voltammograms of a symmetric double layer capacitor cell comprised of 1 cm^2 activated carbon electrodes. The cyclic voltammetry measurements are performed at different scan rates and show deviation from the ideal rectangular behavior for more rapid scan rates.

in which the capacitance is 0.331 F at 10 mHz and 0.346 F at 1 mHz. This capacitance plot as a function of frequency is derived from the frequency spectrum of the cell. The resistance of the cell, which as shown in Fig. 5.9 is approximately 2.7 Ω at the 3 dB frequency, and the low frequency capacitance of the cell, which is shown in Fig. 5.11 is 346 mF, yielding a time constant τ on the order of 1 s.
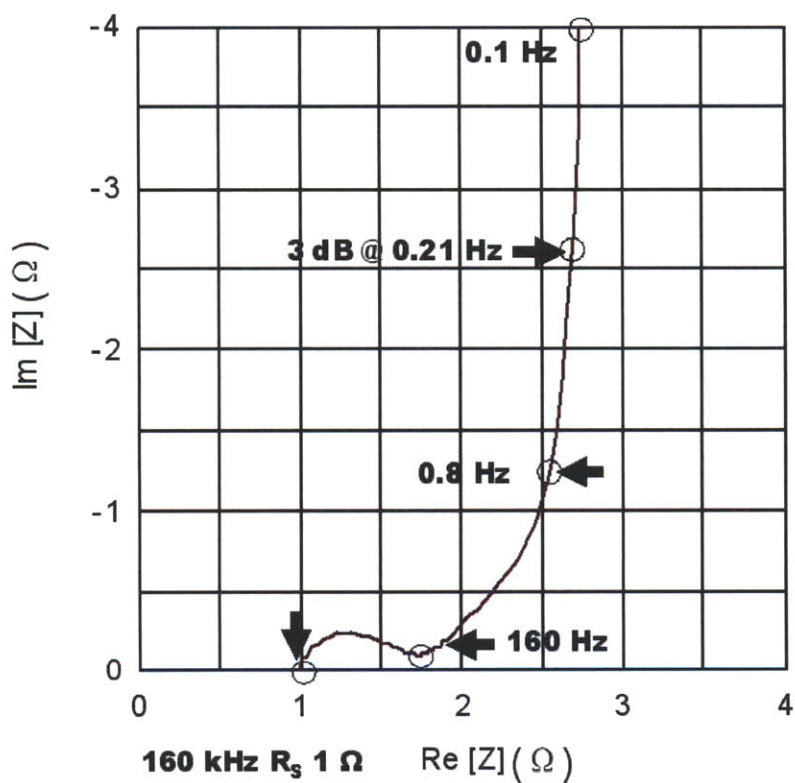
Figure 5.9: Nyquist plot of the impedance of a symmetric double layer capacitor cell comprised of 1 cm^2 electrodes having an activated carbon layer thickness of 135 μm. The impedance spectrum is measured at a bias of 0 V. The arrows and the circles indicate the frequency. R_S indicates the equivalent series resistance of the cell.
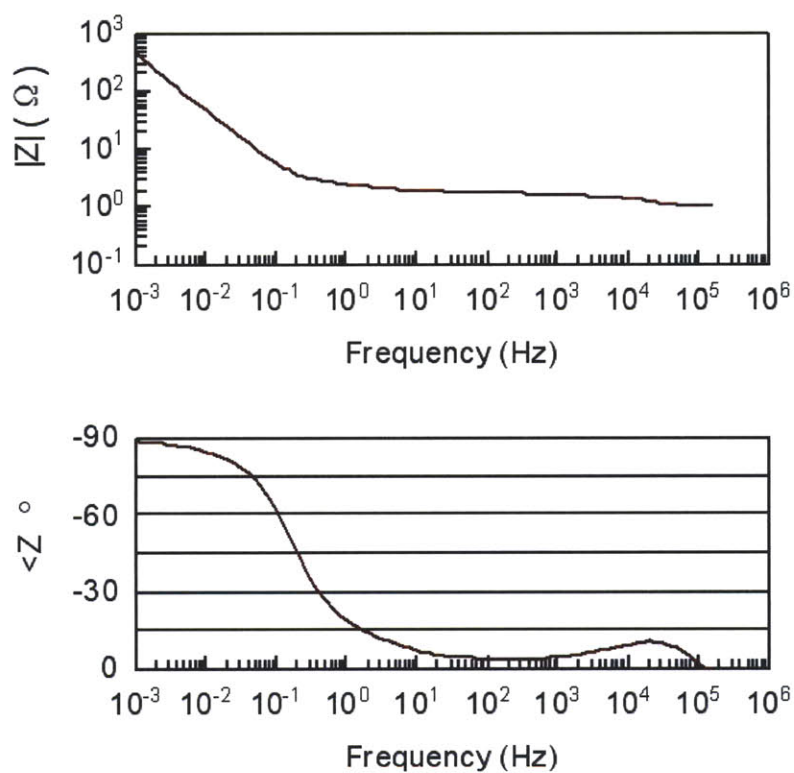
Figure 5.10: Bode plot of the impedance of a symmetric double layer capacitor cell comprised of 1 cm^2 electrodes having an activated carbon layer thickness of 135 μm. The impedance spectrum is measured at a bias of 0 V.
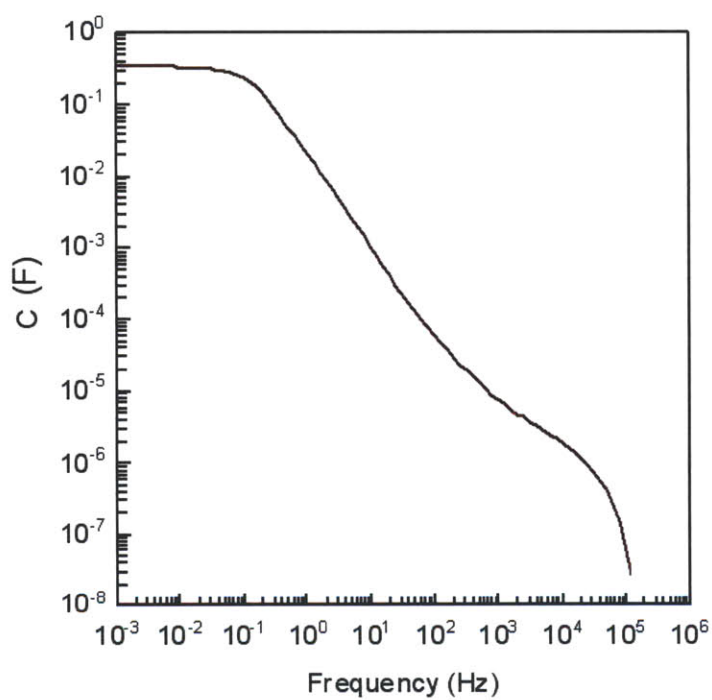
Figure 5.11: Cell capacitance as a function of frequency of a symmetric double layer capacitor cell comprising of 1 cm^2 electrodes having an activated carbon layer thickness of 135 μm.

5.2.3   Activated Carbon Packaged Cell

The measurements of the 1 cm^2 activated carbon cell are now compared to the measurements of a packaged D-size ultracapacitor that uses this electrode material. The comparison allows to validate our method of extrapolating data relative to a packaged cell from data relative to a 1 cm^2 electrode material. Figures 5.12 and 5.13 show the frequency response analysis of a commercial D-size cell[1] that uses the same activated carbon electrodes characterized by Figs. 5.8 - 5.11. The D-size cell has a weight of 59.5 g and a volume of 43 cm^3. From the impedance spectrum the cell capacitance at 0.01 Hz and a bias of 0 V is 241 F. The rated capacitance for this cell is 350 F, and the lower measured value at 0 V arises from the voltage dependent nature of the diffuse layer which leads to a voltage dependent differential capacitance as shown in section 3.4.3. From the ratio between the measured packaged cell capacitance and the 1 cm^2 cell capacitance the total euclidean size of the activated carbon electrodes in a D-size cell is 241/0.331 = 728 cm^2. This parameter is linearly related to the capacitance scaling and inversely proportional to the resistance of the packaged cell.

Given the maximum applied voltage of 2.5 V and the cell average capacitance of approximately 300 F over the potential range, the calculated gravimetric and volumetric energy densities for the D cell are therefore approximately 4.5 Wh/kg and 6 Wh/l. This calculated results are very close (less than 10% error) to the volumetric and gravimetric energy density specified by the vendor of 5 Wh/kg and 6.1 Wh/l and thus corroborate our model to predict the energy density of a packaged cell from data regarding a 1 cm^2 test cell.

---

[1]The D-size cell is a 350 F ultracapacitor cell manufactured by Maxwell Technologies.
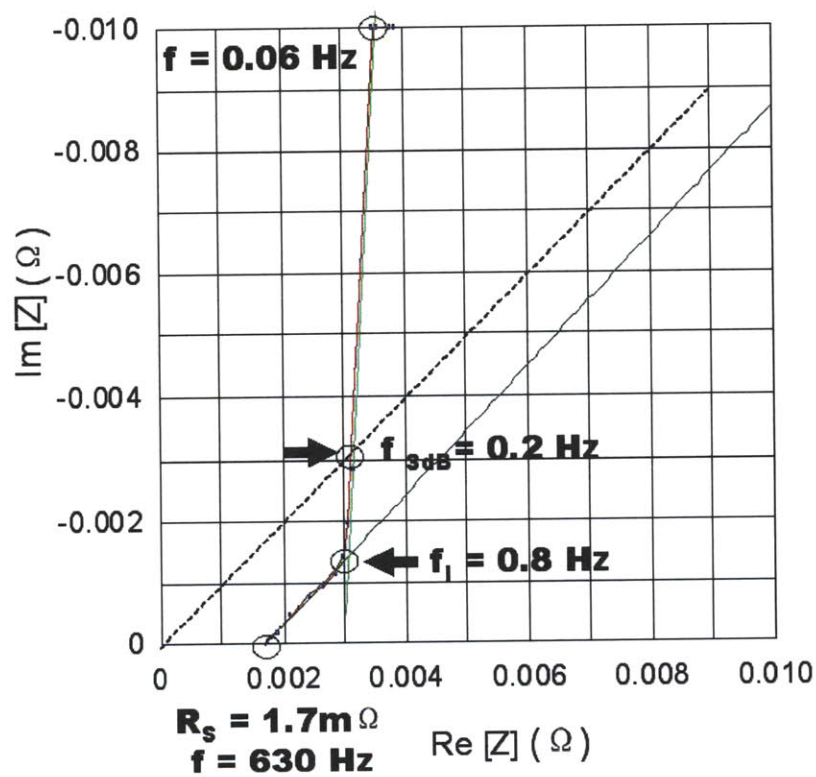
Figure 5.12: Nyquist plot of a D-size cell manufactured by Maxwell Technologies. R_S is the equivalent series resistance of the cell. The intersection between the dotted line (which has a slope of 45°) and the impedance identifies the 3 dB attenuation point of the impedance and its frequency. The impedance spectrum is measured at a bias of 0 V.
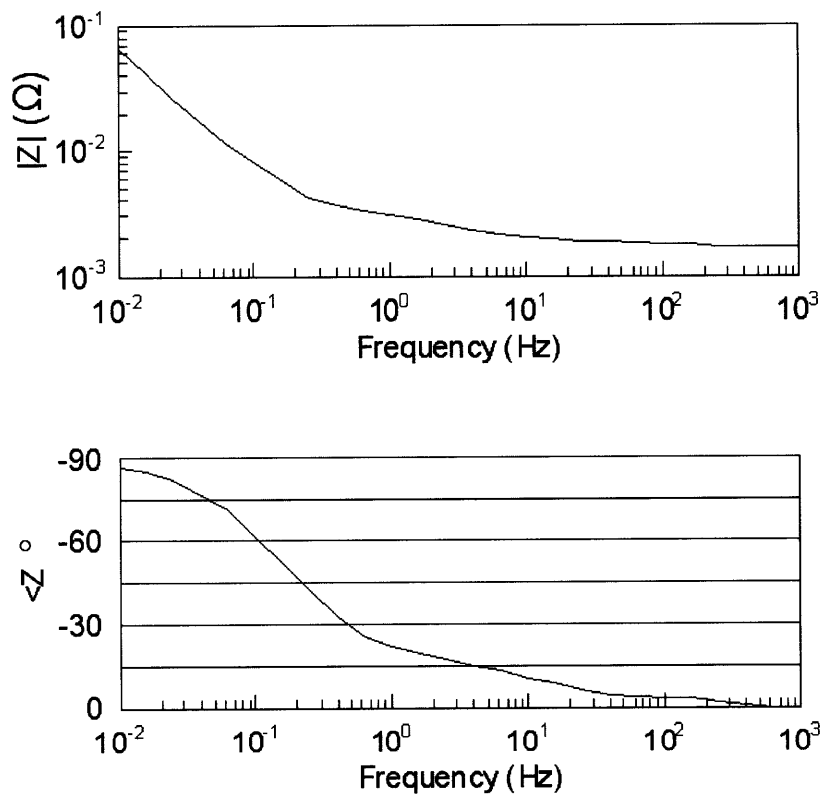
Figure 5.13: Bode plot of a D-size cell manufactured by Maxwell Technologies. The impedance spectrum is measured at a bias of 0 V.

5.3   Capacitance Cell Measurements and Capacitance Model Validation for a CNT based Cell

The previous section discussed capacitance measurements made on activated carbon-based electrodes. This section reports measurements made on symmetric double layer capacitor cells packaged with vertically aligned nanotube-based electrodes in which the nanotubes present three examples of thicknesses. Three data points where used in order to verify the linearity between the electrode capacitance and the thickness of the nanotubes. From the analysis of these measurements we extrapolate the energy density performance of a double layer capacitor cell packaged using CNT electrodes. The energy density extrapolation is done using the same procedure as was used for activated carbon electrodes, as described in section 3.3. Finally, this section concludes by indicating the electrode parameters that we are currently optimizing to improve the energy density performance.

5.3.1   Measurements on a 18 μm Thick Nanotube Electrode

This subsection reports cyclic voltammetry and frequency response analysis measurements of a symmetric cell assembled with electrodes based on carbon nanotube films having a thickness of 18 μm. The next subsection repeats these measurements for nanotube electrodes having thicknesses of 30 μm, and 75 μm. The nanotube film was-grown in each case on a 500 μm thick layer of tungsten, and both anode and cathode have a size of 1 cm^2. Each set of measurements includes data extracted from cyclic voltammetry and frequency

response analysis. All the cells are assembled according to the procedure described in section 5.1, and a one molar $TEMA - BF_4$ in acetonitrile is used as the electrolyte. Moreover the experimental conditions for the measurements of activated carbon and carbon nanotube-based electrodes are the same. Three sheets of NipponChemicon® paper are used as the separator.

Figure 5.14 shows a cross section of the 18 μm thick electrode used in the first cell. Figure 5.15 shows the results of a set of cyclic voltammetry measurements performed on

Figure 5.14: Scanning electron micrograph of an 18 μm thick CNT electrode showing the nanotube active layer on top of a tungsten charge collector. The picture was acquired using a JEOL 5910 SEM viewing the sample placed vertically onto the SEM stage.

the cell at different scan rates. Figure 5.15 shows that even at a scan rate of 1000 mV/s the voltammogram shape is nearly square and that the capacitance value is nearly constant with respect to the scan rate which indicates a rapid response (or short RC time constant) for

the cell. The cell capacitance measured from the cyclic voltammetry data is 1.8 mF, which

accounts for the small RC time constant. Since the two electrodes are morphologically very

similar, the capacitance of each electrode[2] is 3.6 mF. Each electrode active layer has a

size of 1 cm^2 and a thickness of 18 μm, which yields a volumetric capacitance of 2 F/cm^3.

Figures 5.16 and 5.17 show the frequency response characteristics of the cell with Nyquist
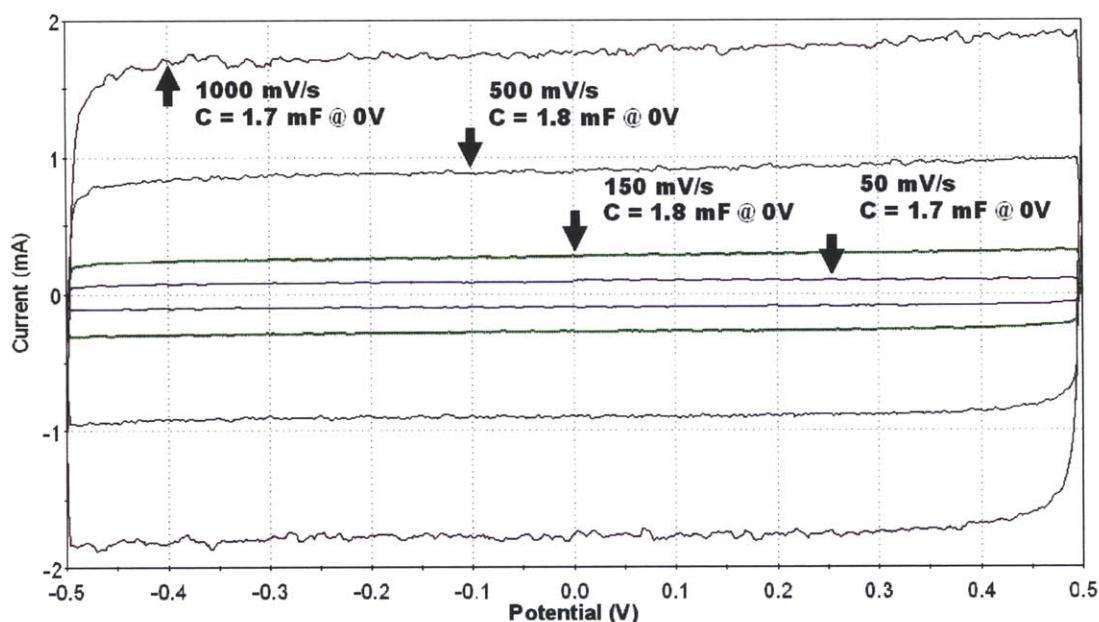
Figure 5.15: Cyclic voltammetry of a symmetric double layer capacitor cell comprised of
a 1 cm^2 18 μm thick carbon nanotube anode and cathode. The different curves show the
cyclic voltammetry measurements of the cell at different scan rates. The arrows relate each
capacitance measurement to its curve.

and Bode plots, respectively. Figure 5.16 shows an equivalent series resistance of the cell

of 0.5 Ω, which is approximately half of that of the activated carbon-based cell shown in

Fig. 5.9. It also shows a transition frequency[3] of this cell at approximately 1000 Hz. The

---

[2]The cell capacitance C_T of two identical electrodes C_E is half of the capacitance of each electrode
$C_T = (C_E^{-1} + C_E^{-1})^{-1} = C_E/2$.

[3]The transition frequency is the frequency at which the behavior of the cell transition from being dominated by diffusion to being capacitive. A detailed explanation of the modeling and implication of the

3 dB attenuation point in the impedance is at 95 Hz. These data indicate a quite large

bandwidth for this cell which is due to the lower resistance at the 3 dB frequency and small

cell capacitance[4] relative to the activated carbon cell. For the case of an activated carbon

electrode the cell resistance at the 3 dB frequency and capacitance are respectively 2.7 Ω

and 0.346 mF leading to a bandwidth of 0.2 Hz which is confirmed by Fig. 5.9. For the case

of the cell packaged with nanotube electrodes the resistance at the 3 dB frequency and the

capacitance are respectively 1.2 Ω and 1.8 mF leading to a bandwidth of 75 Hz, which is

close to that shown by Fig. 5.16[5]. As shown later in this section, the cell capacitance scales

linearly with the nanotube film thickness. Section 6.3.3 describes a model to predict the

cell bandwidth given different nanotube morphologies. Due to the larger capacitance of

the 1 cm^2 activated carbon electrode than that of the 1 cm^2 nanotube electrode, we cannot

compare the shape of the two voltammograms or the shape of the Nyquist and Bode plots.

---

transition frequency for nanotube and activated carbon electrodes is carried out in Chapter 6.

[4]At the 3 dB frequency the reactance and the resistance of the cell are equal and thus $f_{3\ dB} = 1/(2\pi C R)$. Therefore, given a similar cell resistance, a lower capacitance would lead to a higher cell bandwidth

[5]The difference between the calculated and the measured bandwidth comes from the difference between the cell capacitance at the 3 dB point and the low frequency capacitance used for the calculation.
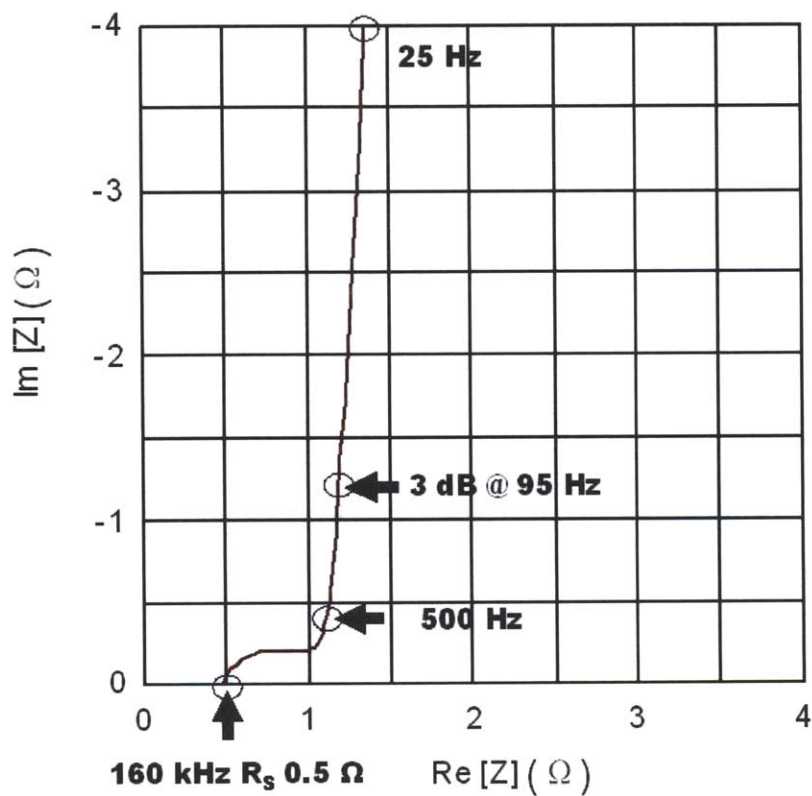
Figure 5.16: Nyquist plot of the impedance of a symmetric double layer capacitor cell comprised of a 1 cm^2 wide and 18 μm thick carbon nanotube-based anode and cathode. The impedance data are recorded at a bias of 0 V.
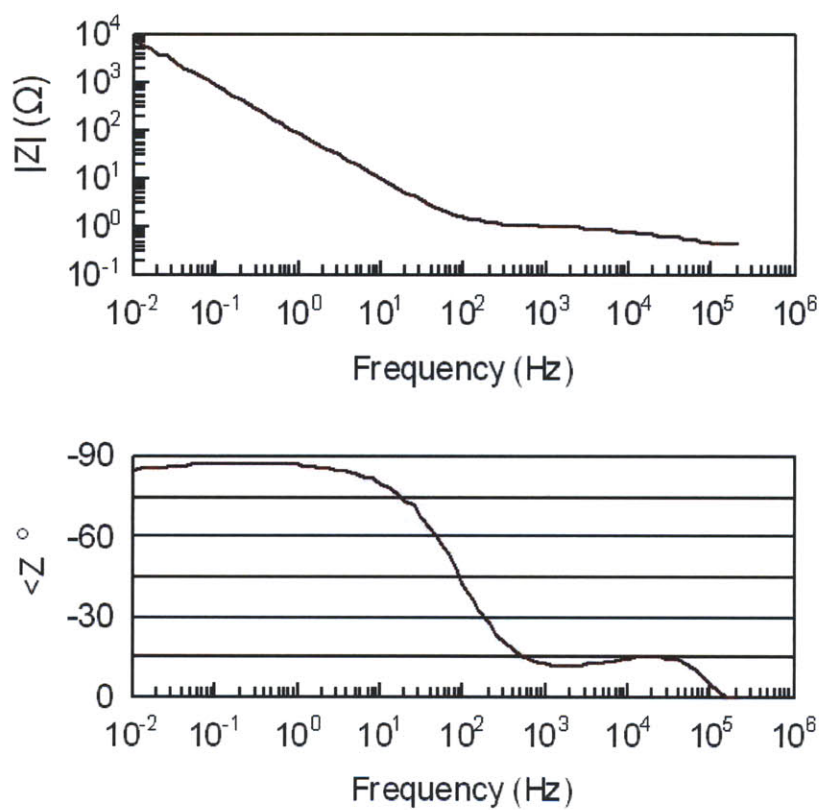
Figure 5.17: Bode plot of the impedance of a symmetric double layer capacitor cell comprised of 1 cm^2 wide and 18 μm thick carbon nanotube-based anode and cathode. The impedance data are recorded at a bias of 0 V.

5.3.2   Electrode Measurements on a 33 μm Thick Nanotube Electrode

The sets of measurements performed on the double layer capacitor cell packaged with 18 μm electrodes are repeated using 33 μm CNT electrodes. Figure 5.18 shows the 33 μm thick electrode active layer fabricated on top of a 500 μm thick tungsten charge collector. Similar
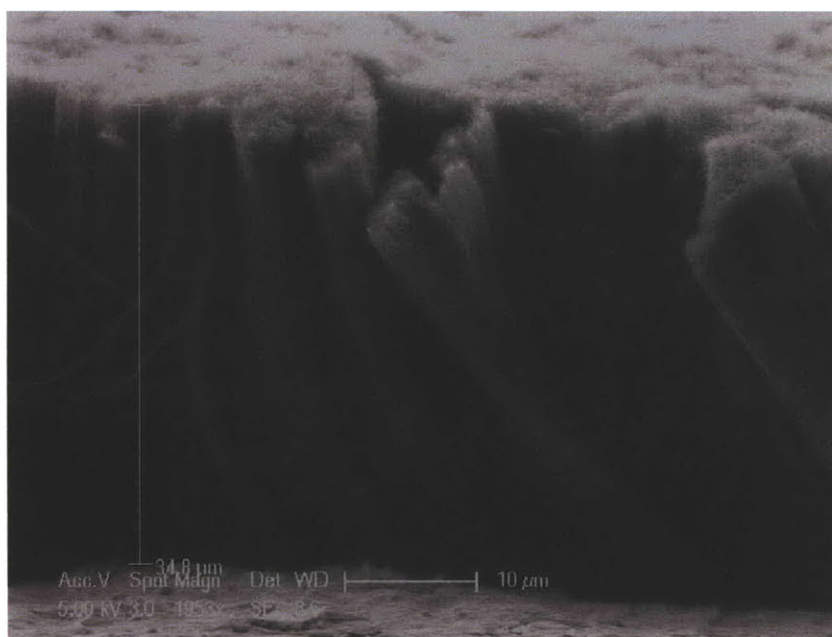
Figure 5.18: Scanning electron micrograph of a 33 μm thick CNT electrode showing the nanotube active layer on top of the tungsten charge collector. The picture was acquired using a JEOL 5910 SEM viewing the sample placed vertically onto the SEM stage. This picture was taken by Sulinya Ramanan and by Eletha Flores.

to the 18 μm measurements, the cyclic voltammetry data in Fig. 5.19 shows a nearly square shape and a nearly constant capacitance with increasing scan rate, which is again indicative of the rapid response, or short RC time constant, of the cell for scan rates up to 500 mV/s. The short time constant though is mainly due to the small capacitance, 5.8 mF, of the electrode. The frequency response analysis for this cell packaged using 33 μm thick elec-
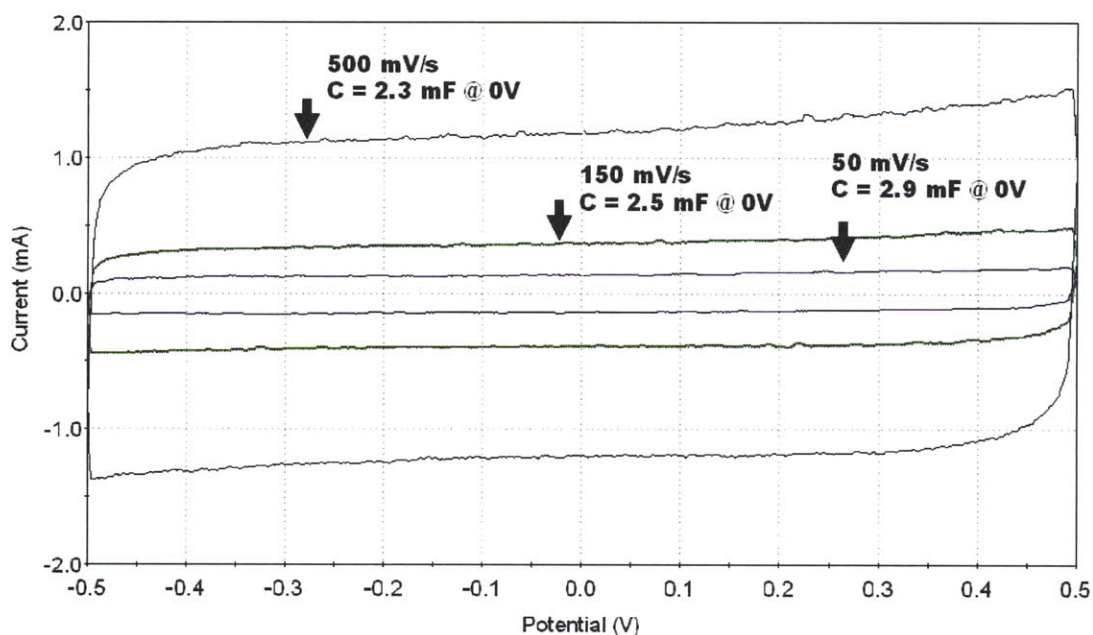
Figure 5.19: Cyclic voltammetry data for a symmetric double layer capacitor cell comprised of a 1 cm^2 wide and 33 μm thick carbon nanotube anode and cathode. The different curves show the cyclic voltammetry measurements of the cell at different scan rates. The arrows relate each capacitance measurement to its curve.

trodes is shown in Figs. 5.20 and 5.21. The Nyquist plot in Fig. 5.20 presents an initial high frequency semi-circle and a nearly ideal capacitive behavior with a phase approaching the 90° angle characteristic of an ideal capacitor of 2.3 F for frequencies lower that the transition frequency of 500 Hz. The 3 dB attenuation in the impedance is at a frequency of 90 Hz.
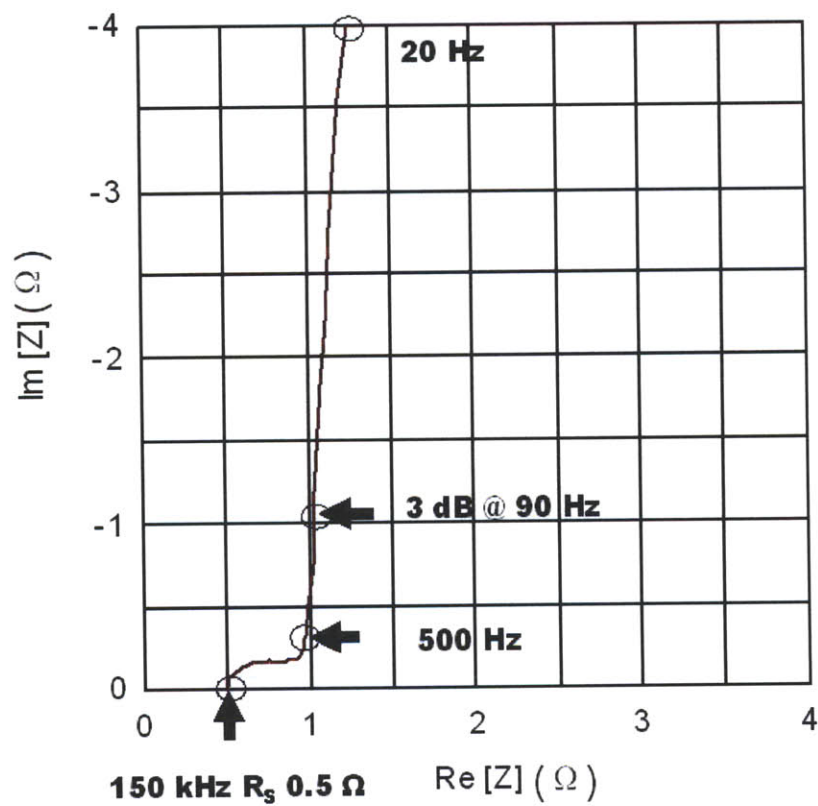
Figure 5.20: Nyquist plot of the impedance of a symmetric double layer capacitor cell comprised of a 1 cm^2 wide and 33 μm thick carbon nanotube-based anode and cathode. The impedance data are recorded at a bias of 0 V.
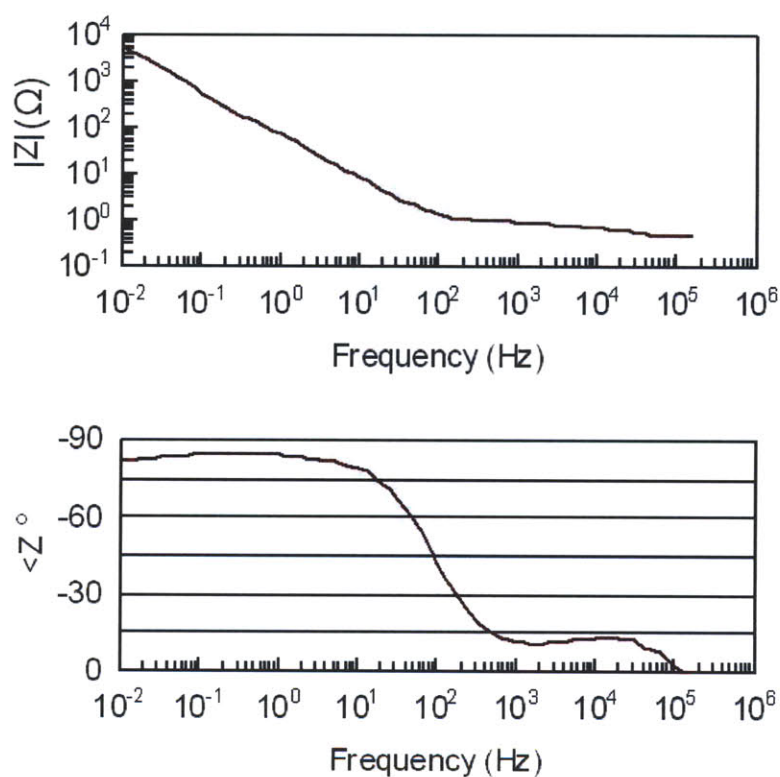
Figure 5.21: Bode plot of the impedance of a symmetric double layer capacitor cell comprised of a 1 cm^2 wide and 33 μm thick carbon nanotube-based anode and cathode. The impedance data are recorded at a bias of 0 V.

5.3.3   Electrode Measurements on a 75 μm Thick Nanotube Electrode

The measurements are repeated using electrodes with a thickness of 75 μm. Figure 5.22 shows the electrodes used for the packaging of this cell. Similar to the previous cases,
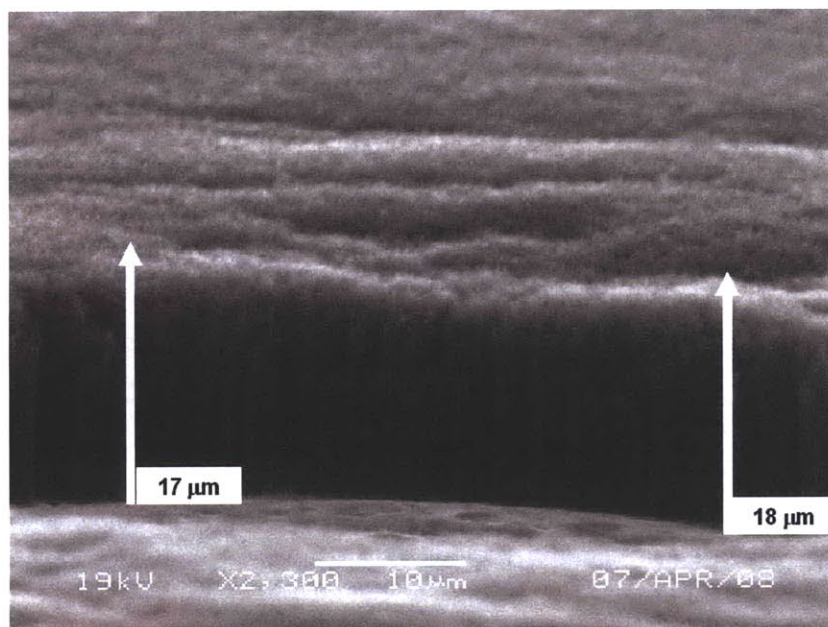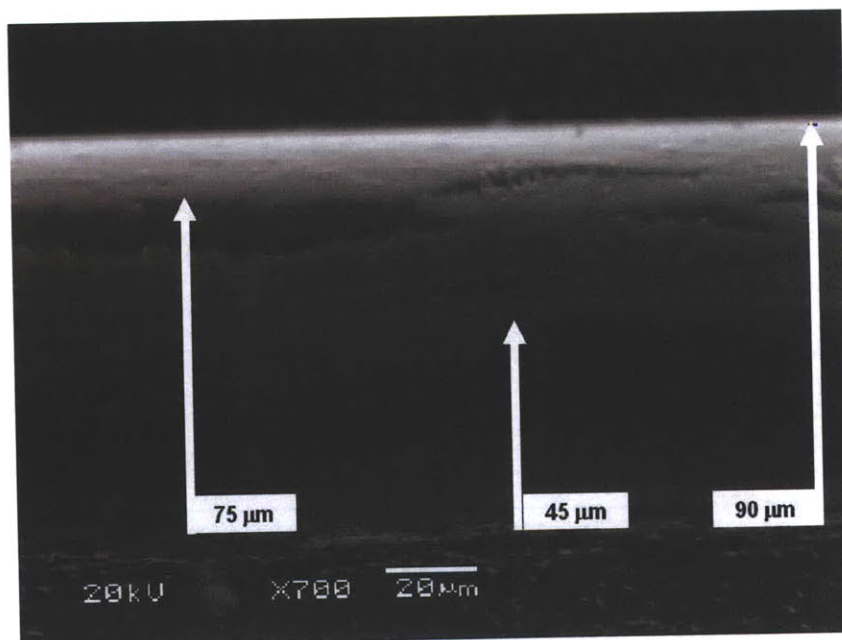

Figure 5.22: Scanning electron micrograph of an 75 μm thick CNT electrode showing the nanotube active layer on top of the tungsten charge collector. The picture was acquired using a JEOL 5910 SEM viewing the sample placed vertically onto the SEM stage.

cyclic voltammetry data for this cell exhibit a nearly square shape and a nearly constant cell capacitance of 11.5 mF with increasing scan rates indicating the rapid response of the cell for scan rates up to 500 mV/s. As before, the frequency response analysis for this cell presents a nearly ideal behavior with a phase approaching the 90° angle characteristic of an ideal capacitor for a frequency lower that the transition frequency of 80 Hz. The 3 dB attenuation in the impedance is at a frequency of 15 Hz.

5.3.4   CNT Electrode Measurement Analysis

Figure 5.23 shows that the measured electrode capacitance scales linearly with respect to the electrode thickness. This results is expected and it indicates that the electrolyte wets the void volume of the electrode. In case of incomplete wetting, increases in nanotube length would not translate into increases in the electrode capacitance. As summarized in Table 5.1,
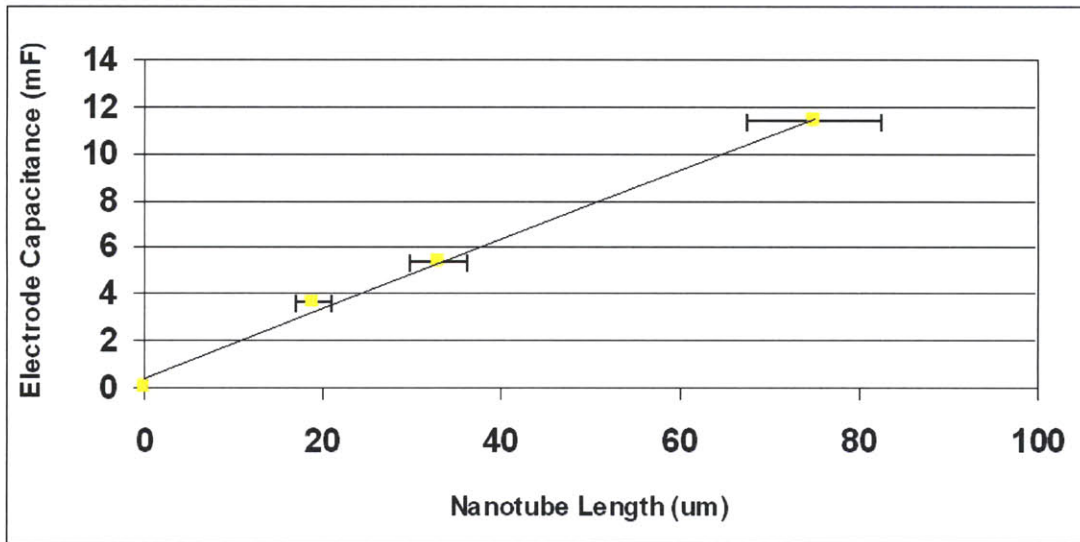
Figure 5.23: Relation between the thickness of the carbon nanotube active layer and the electrode capacitance. The graph shows the expected linearity between electrode capacitance and nanotube film thickness.

the three nanotube-based cells have a volumetric capacitance ranging from 1.5 to 2 F/cm^3 and a gravimetric capacitance on the order of 28 F/g, which are measured at low frequency (10 mHz). The capacitance measurements for the cells reported in Table 5.1 match the capacitance expected from the modeling proposed in section 3.3. Considering for instance cell 3, the nanotube density of its electrodes was $6 \cdot 10^{10}$ cm^{-2}. The density of nanotubes in the electrodes was measured according to the procedures discussed in section 4.3.1 by

	CNT Thickness μm	ρ_C 10^{-10} cm^{-2}	CNT Weight mg	Cell Capacitance C_T mF	Electrode Capacitance C_E mF	Volumetric Capacitance F/cm^3	Gravimetric Capacitance F/g
Cell 1	18	6	-	1.8	3.6	2	-
Cell 2	33	7	-	2.9	5.8	1.7	-
Cell 3	75	7.5	0.41	5.7	11.4	1.5	28

Table 5.1: Cell and electrode capacitance as a function of the nanotube electrode active layer thickness.

examining the electrodes after having performed the electrical measurements on the cell. The cell and the electrodes after the measurements were dried and the nanotube substrate was sonicated away from the charge collector and the density was analyzed according to the procedures described in section 4.3.1 on the tested electrodes. At present, the nanotube density is lower than our target. From the measured weight of the electrode active layer[6] of 0.41 mg and from the average number of walls and diameters for the nanotubes that are, respectively, 6 and 6.5 nm, the estimated density of the nanotube active layer is $6 \cdot 10^{10}$ cm^{-2}, which is given by (4.3). This estimated nanotube density, in conjunction with the length (t_C), and diameter (d_C) of the nanotubes, leads to a total CNT surface area for the 1 cm^2 active layer, A_{TOT}, given by

$$A_{TOT} = \rho_C \cdot \pi d_C t_C = 0.092 \text{ m}^2 \qquad (5.1)$$

The differential capacitance calculated at a 0 V bias using the Gouy-Chapman-Stern model in section 3.4.3 is 11 μF/cm^2. The cell capacitance calculated using (3.8), which is repeated

---

[6]The weight of the electrode active layer was measured using a scale with a resolution of 0.01 mg. The resolution of the scale used is not sufficient to measure the weight of the active layers of the electrodes of cell 1 and 2, and that is why only cell 3 has an indication of its gravimetric capacitance.

here, is

$$C_T = A_{TOT} \cdot C_D / 2 = 5.06 \; mF \tag{5.2}$$

and thus the calculated electrode capacitance, C_E is given by

$$C_E = 2 \cdot C_T = 10.1 \; mF, \tag{5.3}$$

which matches within 10% the measured electrode capacitance of cell 3 (11.4 mF). This demonstrates the validity of our geometrical model to predict the cell and electrode capacitance based on the carbon nanotube morphology. Considering the surface area A_{TOT} for the electrodes of cell 3, their measured differential capacitance is given by

$$C_D = \frac{11.4 \; mF}{A_{TOT}} = 12 \; \mu F/cm^2 \tag{5.4}$$

where 11.4 mF is the measured electrode capacitance. This shows that the calculated differential capacitance, using the Gouy-Chapman-Stern theory, of 11 $\mu F/cm^2$ is in good agreement with the measured differential capacitance of 12 $\mu F/cm^2$.

From the nanotube electrode densities of cells 1 and 2, (determined by analyzing the electrodes after the electrical measurements according to the procedures described in section 4.3.1), which are respectively $7.5 \cdot 10^{10}$ cm^{-1} and $7 \cdot 10^{10}$ cm^{-1}, from the average diameter and number of walls of the nanotubes (6.5 nm and 6), from the respective electrode thicknesses (18 and 33), the total surfaces for the electrodes of cell 1 and 2 are 0.027 and 0.047 m^2. From these respective total electrode surfaces and from the differential capaci-

tance calculated for cell 3 of 12 μF/cm^2, the expected electrode capacitances for cells 1 and

2 are, respectively, 3.3 mF and 5.7 mF. These capacitances are again very close (having and

error less than 5%) to the measured capacitances of 3.6 mF and 5.8 mF for the electrodes

of cells 1 and 2, which validates our geometrical model for estimating the capacitance of

nanotube electrodes presented in section 3.3.

5.3.5   Device Energy Density Extrapolation from the Electrode Capacitance

The measured volumetric capacitance values for these three cells and the gravimetric capac-

itance for cell 3 are lower than our target of 102 F/cm^3 and of 225 F/g due to the nanotube

morphology of the specific electrode. The nanotube features of the electrodes that need to

be improved to reach the capacitance targets are the nanotube density and the nanotube

differential capacitance. The differential capacitance for cell 3 is 12 μF/cm^2 as indirectly

measured in this section. Our differential capacitance target is on the order of 50 μF/cm^2.

Section 7.2 describes our approach to improve this parameter and to achieve this target.

The current carbon nanotube density of our electrodes ranges from $0.5 \cdot 10^{11}$ cm^{-2} to

$2.6 \cdot 10^{11}$ cm^{-2}. These values are also lower than our target range of 5 to $10 \cdot 10^{11}$ cm^{-2}

and section 7.2 describes our approach for improvement.

As shown by section 5.2, activated carbon packaged cells achieve energy densities of approx-

imately 4.5 Wh/kg and 6 Wh/l. Table 5.2 shows our expected energy density as a function

of the carbon nanotube density. Table 5.2 assumes nanotubes having an average diameter

of 6.5 nm, an average of 4 walls each, a length of 100 μm, and the target differential ca-

pacitance of close to our target of 50 μF/cm^2. The energy density values are extrapolated

Electrode Type A.C. Multiple	E 1	E 2	E 3 x1.2	E 4 x2.2	E 5 x3.5	E 6 x5	E 7 x7
ρ_C x 10^{11} (cm^{-2})	0.51	1	1.6	3.1	5.1	6.9	10
C_T (mF)	26	53	82	158	260	355	511
C_E (mF)	52	106	164	315	521	710	1,021
E_V (Wh/l)	1.86	3.83	5.88	11.3	18.8	25.5	36.8
E_G (Wh/kg)	3.24	4.14	6.20	11.1	17.2	21.6	30.0

Table 5.2: Cell energy densities and capacitances as a function of the electrode active layer specifications.

according to the model in section 3.3 assuming a voltage of 3.5 V and electrolyte molarity

of 2 mole/l for electrodes E 6 and E 7. All the other electrodes assume electrolyte molarity

of 1.4 mole/l.

In Table 5.2, electrode type identifies the specifics of the electrode considered, A.C. multiple

refers to how many times the energy density of a ultracapacitor device packaged with

nanotube electrodes is greater than that of an activated carbon one. ρ_C is the density of

carbon nanotubes per cm^2 of electrode, C_T and C_E are respectively the cell capacitance

and the electrode capacitance. Finally, E_V and E_G are the volumetric and gravimetric

capacitance for a packaged cell using that electrode type.

5.4   Chapter Summary

This chapter explains the procedure that we developed to prepare an electrochemical cell that packages the nanotube electrodes that we produce or, alternately, packages activated carbon electrodes for comparison. This chapter showed the procedure used for measuring the cell and electrode capacitance, and predicts the energy density for a packaged D-size cell that use CNT or activated carbon electrodes. The energy density predicted using this procedure for an activated carbon-based D-size cell is compared with the vendor specifications showing an error smaller than 10%. This chapter also compare the electrode capacitance predicted from a specific nanotube electrode morphology with our modelling with the measured capacitance. The comparison shows an error less than 5%. The chapter concludes with a discussion on the expected energy density of a cell packaged using electrodes of different morphologies, which could be up to seven times that of activated carbon-based ultracapacitors. The next chapter will analyze the power density we can obtain using our nanotube electrodes in a packaged cell.

Chapter 6

Electrochemical Modeling

The previous chapter validated our capacitance modelling based on the capacitance measurements of a cell packaged with nanotube electrodes. This chapter focuses on the analysis and prediction of the impedance spectrum of carbon nanotube-based electrodes which is important for estimating the power density and efficiency of a packaged cell. The chapter starts by introducing the theory and modeling of porous electrodes in electrolyte solutions that are used to predict the impedance spectrum of the electrodes. The chapter then extends the models developed for porous electrodes to include the case of nanotube-based double layer electrodes. The behavior of the impedance spectrum of 1 cm^2 nanotube electrodes is explained and analyzed using an equivalent circuit. The parameters of the circuit are then linked to physical characteristics of the electrodes. Finally, a design procedure is proposed to predict the impedance spectrum of nanotube electrodes given their geometrical characteristics. The resulting impedance leads to useful estimates of the power density and efficiency of a cell packaged using nanotube electrodes. This, in conjunction with the energy density prediction based on measured capacitances proposed in chapter 5 explains the performance of the ultracapacitor.

6.1 Theory of Porous Materials in Electrolyte Solutions

This section discusses the most significant contributions to modelling the behavior of porous electrodes by predicting their impedance spectrum. First, the de Levie model which idealizes the pores as semi-infinite cylinders is presented. Second, the Keiser extension of the de Levie model, which includes pores having a finite length, is presented. These two seminal contributions in the field are then extended to predict the impedance spectrum of our electrodes made of vertically aligned carbon nanotubes.

6.1.1 Response of Semi-Infinite Pores - the de Levie Model

In 1963 de Levie[18] proposed a model to predict the response of porous electrodes to a sinusoidally varying potential. In his work de Levie simplified the pores as semi-infinitely long cylinders[1] having a uniform diameter $2r_0$ and an semi-infinitely long length as shown in Fig. 6.1. Further, de Levie's model considers the pore to be uniformly filled with an electrolyte. The electrolyte in the inside of the pores presents an ionic uniformly distributed resistance per unit length R and a capacitance per unit length C. The idealized pore is assumed to behave according to the RC distributed network shown in Fig. 6.2 for which the differential equations are

$$de = \frac{\partial e}{\partial z}dz = -iRdz \tag{6.1}$$

$$di = \frac{\partial i}{\partial z}dz = -C\frac{\partial e}{\partial t}dz \tag{6.2}$$

---

[1]Semi-infinitely long pores are pores having a finite length that within a certain frequency range behave as if they had an infinite length.
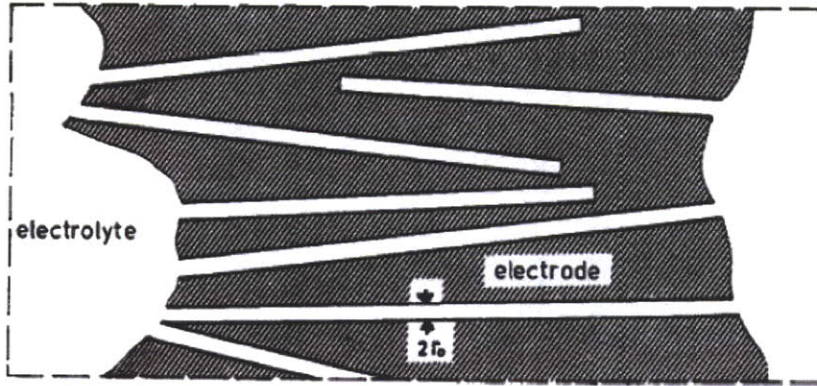
Figure 6.1: Representation of the porous electrode in the de Levie model in which the pores have a radius r_0 and a semi-infinite length. The black regions are the solid electrode and the white region are the pores filled with electrolyte. The picture is reproduced from[1].

where e is the potential in the pore referenced to the bulk electrolyte. The differential

equation modeling the pore behavior can be combined resulting in the following equation

$$\frac{\partial^2 e}{\partial z^2} - RC\frac{\partial e}{\partial t} = 0. \tag{6.3}$$

Imposing the boundary conditions (a sinusoidally varying potential) at the entrance to
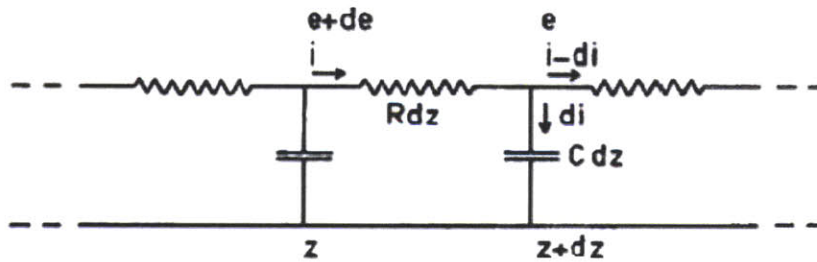
Figure 6.2: Distributed RC network that models the behavior of the semi-infinite pore along its axis z. The picture is reproduced from[1].

the pore, $e(0,t) = E\sin(\omega t)$, and at a distance z infinitely far from the orifice entrance,

$e(z,0) = e(\infty,t) = 0$, the charging current into the pore that corresponds to the potential

that solves (6.3) and that satisfies the imposed boundary conditions is

$$i(0,t) = \frac{E}{R}\sqrt{\frac{1}{2}\omega RC}[\sin(\omega t) + \cos(\omega t)]. \tag{6.4}$$

The condition $e(\infty, t) = 0$ is approximately satisfied for a length of pore l that satisfies the condition

$$l \geqslant \frac{8}{\sqrt{\omega RC}} = \frac{8}{\sqrt{2\pi f RC}}. \tag{6.5}$$

This condition is satisfied at high enough frequencies resulting in a 45° angle between the potential imposed at the surface of the orifice and its charging current[2]. The 45° angle between the potential and current translates in a 45° phase angle in the impedance, which is caused by the distributed RC nature of the model representing ion transport in the pore. Although this model is rather rudimentary due to the fact that the pores in a real electrode have neither a uniform radius nor a semi-infinite length, it explains the observed behavior for frequencies for which the the pore length l satisfies the condition $l \geqslant 8/\sqrt{\omega RC}$ while ceasing to be applicable for frequencies that do not satisfy this condition.

6.1.2   Keiser Extension to Finite Length Pores

The model originally proposed by de Levie for the case of semi-infinite pores [1] was extended by Keiser et al. in 1976 to treat the case of porous electrodes in which the pores have length less than $\frac{8}{\sqrt{\omega RC}}$ [2]. Keiser predicted the shape of the impedance spectrum as a function of

---

[2]This results from the identity $\sin(\omega t) + \cos(\omega t) = \sqrt{2} \cdot \sin(\omega t + \pi/4)$

the parameter l/λ for pores having different geometries as shown by Fig. 6.3, where λ is

$$\lambda = \sqrt{\frac{rk}{8\pi f C_D}} \tag{6.6}$$

where r is the radius of the pores, k is the specific conductance, in (S/cm, of the electrolyte inside the pores, C_D in F/cm^2, is the differential capacitance of the surface of the double layer, and f is the frequency. The dotted lines in Fig. 6.3 refer to different values of l/λ, which is a function of frequency and the geometrical parameters of the electrodes. For
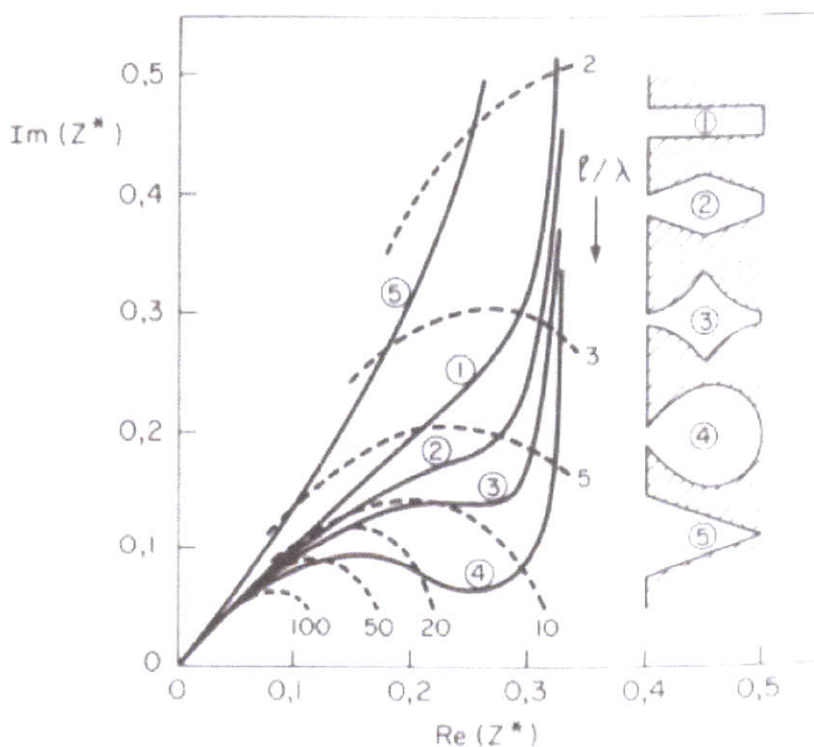
Figure 6.3: Normalized impedance spectrum, Z^*, of pores having geometries indicated from 1 to 5, as predicted by Keiser [2]. The real and imaginary part of Z^* are normalized by the resistive parameter R_0 and thus Z^* is unitless. The dotted lines indicate values of the ratio l/λ at different points on the impedance curves relative to the different pore geometries.

the case of cylindrical pores, Keiser's model predicts the impedance, Z^*, in closed form as a parametric function of l/λ. The real and imaginary parts of the impedance Z^* are normalized by the parameter R_0.

$$R_0 = \frac{l}{\pi k r^2} \tag{6.7}$$

Figure 6.4 shows Z^* as a parametric function of l/λ. Considering the case of idealized
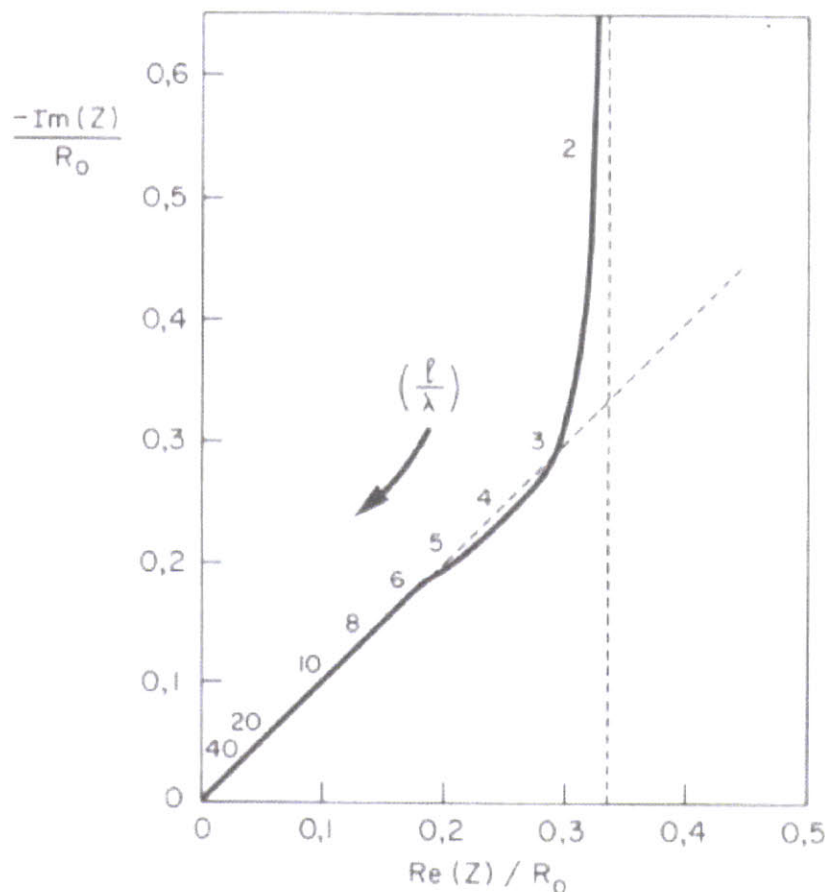
Figure 6.4: Normalized impedance spectrum as a function of l/λ of a cylindrical pore having length l, as predicted by Keiser [2]. The numbers on the impedance indicate values of the ratio l/λ. The dotted line are the extension of the 45° region of the impedance and the 90° impedance asymptote. The real and imaginary part of Z are normalized by the resistive parameter R_0 and thus the impedance in the graph is unitless.

response of the porous material. The first, high frequency, region presents the same 45°
slope in the Nyquist impedance plot that was predicted by the de Levie model, which is
due to the distributed nature of the electrolyte resistance and capacitance over the length
of the pores. This region extends down to the transition frequency $\bar{f}$ for which $l/\lambda \sim 3$.
At frequencies lower than $\bar{f}$ the Keiser model predicts a 90° slope, which as shown in
section 6.2.1, is indeed observed in activated carbon porous electrodes, and is due to the
capacitance of the double layer of charge. This implies that for frequencies lower than $\bar{f}$
the resistance and capacitance along the pore axis ceases to appear distributed and can be
lumped into a total pore resistance and a capacitance, which is equivalent to the capacitance
of the double layer. We will call this the quasi static region. The 45° slope is given by the
distributed nature of the resistance and capacitance of the pore and we call this the dynamic
region.

6.2   Behavior of Activated Carbon Electrodes

This section applies the de Levie and Keiser models to describe the impedance spectrum
of activated carbon electrode cells. It shows how the transition frequency between the
dynamic and quasi-static region can be predicted using the Keiser model. Thereafter the
section shows how the different regions of the impedance spectrum can be represented by
an equivalent circuit model. Section 6.3.2 shows a procedure for predicting the circuit
parameters of the model given the physical features of the electrode.

6.2.1 Application of the de Levie and Keiser Models

We are considering a one molar acetonitrile electrolyte and activated carbon electrodes for which the distributed resistance and capacitance per unit length R and C are $R = 1/(kr_0^2\pi) = 4.4 \cdot 10^{16}$ Ω/cm and $C = C_D r_0 2\pi = 9.4 \cdot 10^{-12}$ F/cm where, k ~ 2 mS/cm. [20] specifies ranges for the values of the activated carbon electrode and acetonitrile electrolyte parameters that are necessary to calculate R and C, and here we report the values (summarized in Table 6.1) that we use for these calculations. The the pore length, l, is approximately 12 μm, the average pore radius for micropores, r_0, is approximately 0.6 nm, and the differential capacitance for activated carbon electrodes with acetonitrile, C_D, is approximately 25 μF/cm^2. The parameter k is the electrolyte conductivity within the activated carbon pores. As discussed by [21], the effective electrolyte conductivity within an electrode is given by

$$k = k_{Bulk} \cdot \varepsilon^x \tag{6.8}$$

where k_{Bulk} is the bulk conductivity (which for a 1 to 2 molar acetonitrile electrolyte is approximately 60 mS/cm), ε is the ratio of void volume to electrode volume (which for activated carbon electrodes is typically of 0.25), and x is an exponent ranging from 1 to 1.8 which takes into account the degree of electrode tortuosity, which depends on the shape of the electrode particles. In the case of nonuniform activated carbon particles randomly distributed, as prescribed by [21], this exponent is assumed to be 1.8.

The pore diameter for activated carbon micro pores, according to the IUPAC definition is smaller then 1.5 to 2 nm and thus the average radius is 0.6 nm. The average pore length

is comparable to the activated particle size and thus 10 μm. This leads to the conclusion, from applying the condition (6.5), that for frequencies higher than $f \geqslant 32/(RCl^2\pi) = 17\,\text{Hz}$ the impedance will show the behavior predicted by de Levie, whereas at lower frequencies the de Levie model ceases to be applicable.

Figure 6.5 shows the impedance spectrum measured for a symmetric double layer capacitor cell made with 1 cm^2 activated carbon electrodes. The data is measured at a bias of 0 V and for frequencies ranging from 1 mHz to 10 kHz. The Nyquist diagram in Fig. 6.5 for activated carbon electrodes shows a 45° slope up to 1.2 Hz and a quasi-static region characterized by an approximately 90° impedance slope for frequencies lower than 1.2 Hz.

The impedance spectrum shown in Fig. 6.5 can be divided into three frequency ranges. The first region is a high frequency semicircle[3] (due to the presence of a resistive oxide layer between the activated carbon and the charge collector); the second dynamic region is characterized by the distinctive 45° slope; and the third quasi-static region is characterized by the approximately 90° slope.

Table 6.1 shows the parameters of the activated carbon electrodes used in this cell. From these electrode parameters the frequency predicted by Keiser at which the impedance behavior changes from dynamic (45°) to quasi-static (90°), that is where $l/\lambda \simeq 3$, is 1.2 Hz, which is in accordance with what is observed in the data. The frequency f_I is the intersect of the asymptotes approximating the dynamic and the quasi-static regions and is 0.8 Hz.

---

[3]It is noted that this high frequency semicircle has a center that is depressed from the real axis of the impedance. An explanation of the cause of this feature is part of the future work of this research.
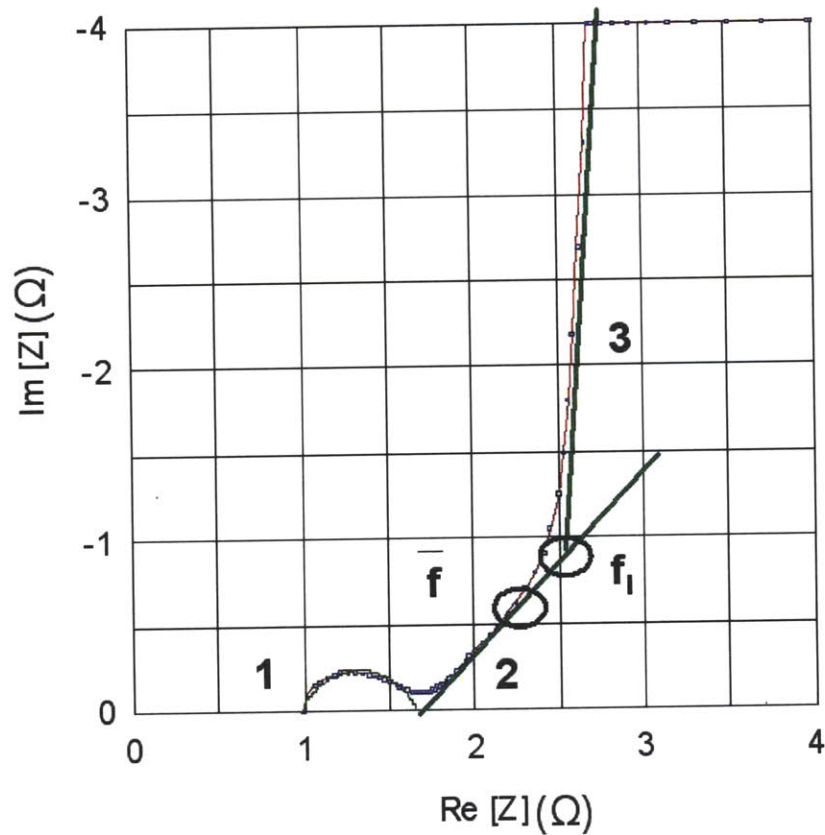
Figure 6.5: Impedance spectrum of a cell made with activated carbon electrodes having parameters shown in Table 6.1. For these parameters $l/\lambda \simeq 3$ at the transition frequency $\overline{f} = 1.2\ Hz$. The intersect frequency f_I at which $l/\lambda \simeq 2.6$ is 0.8 Hz.

At f_I, $l/\lambda \simeq 2.6$.

6.2.2 Equivalent Circuit Model of AC Based DLC Electrode Cells

The impedance spectrum of the activated carbon electrodes described in Table 6.1 can

be simulated using the equivalent circuit model shown in Fig. 6.6. The match between

the measured and simulated impedance spectrum is shown in Fig. 6.7. The topology of

the circuit that we have chosen explicitly shows the parameters that model the particular

	l μm	r_0 nm	C_D μF/cm^2	k_{bulk} mS/cm	k mS/cm	$\overline{f}$ Hz	f_I Hz
Activated carbon cell	12	0.6	25	60	2	1.2	0.8

Table 6.1: Pore dimensions and electrolyte parameters for the activated carbon electrode cell whose measured impedance is shown in Fig. 6.5.

frequency region in the electrochemical spectrum. L and R_S model the impedance intersect at high frequency with the real axis. R_{OX} and C_{OX} model the semicircle. C_1, R_2, C_2, R_3, C_3, and R_P model the dynamic and quasi static region of the impedance. The values of the parameters are determined by providing the impedance spectrum as an input to the software ZWiew from ScribnerAssociates, Inc. This section focuses on the description of the relation
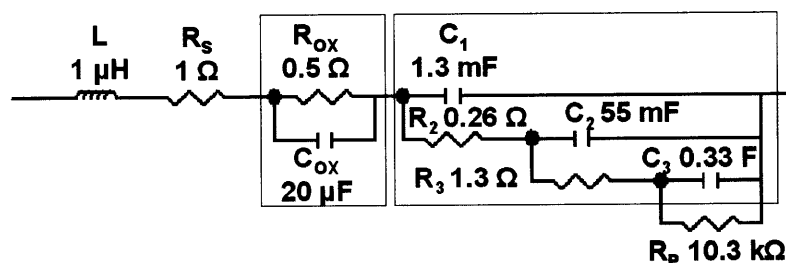
Figure 6.6: Equivalent circuit to model the frequency response behavior of the cell having the parameters shown in Table 6.1. The cell is assembled using 135 μm thick activated carbon-based electrodes.

between equivalent circuit parameters and the different regions of the frequency response spectrum shown in Fig. 6.5. L models the high frequency parasitic inductance that arise from the two electrodes. The resistor R_S represents the high frequency intersect with the real axis, R_{OX} and C_{OX} model the resistive layer present between the charge collector and the activated carbon layer. If we neglect the parasitic inductance, the first time constant of the circuit is given by the equivalent resistance and by the oxide capacitance, $\tau_{OX} = R_S \cdot C_{OX}$.

The dynamic region of the impedance spectrum (the 45° region) is simulated by the two time constants τ_1 and τ_2 where $\tau_1 = (R_S + R_{OX}) \cdot C_1$ and $\tau_2 = (R_S + R_{OX} + R_2) \cdot C_2$. The quasi-static region is described by the time constant τ_3 and by the parallel resistance R_P, where $\tau_3 = (R_S + R_{OX} + R_2 + R_3) \cdot C_3$.
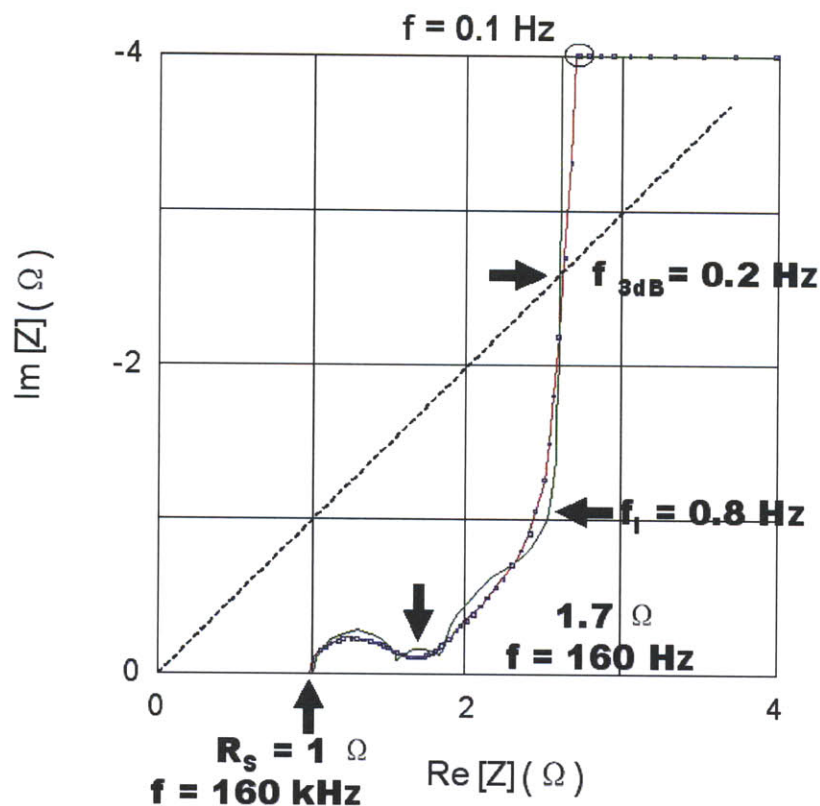
Figure 6.7: Measured and simulated impedance spectrum of a cell made with activated carbon electrodes having the parameters shown in Table 6.1. The measured curve is red and the simulated curve is green. The intersection between the dotted line (which has a slope of 45°) and the impedance identifies the 3 dB attenuation point of the impedance and its frequency.

6.3   Impedance Spectrometry Analysis of a CNT Electrode

This section analyzes the impedance spectrum shown in Fig. 6.8 for a carbon nanotube electrode based cell. The nature of each region of the impedance represented by the Nyquist plot is explained and modeled via an electrical equivalent circuit. The parameters of the equivalent circuit are linked to the physical behavior that is dominant in each region.
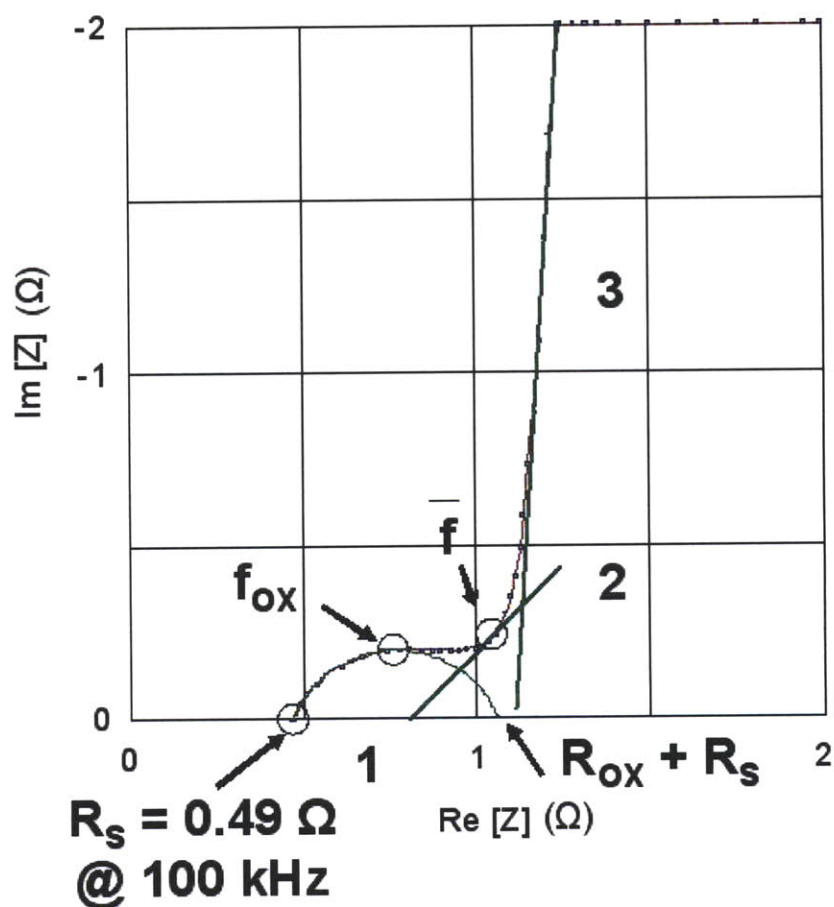
Figure 6.8: Impedance spectrum of a cell made with 18 μm thick carbon nanotube electrodes having the dimensions described by Cell B in Table 6.2.

6.3.1   Overview of the CNT Electrode Impedance

Figure 6.8 shows the Nyquist plot of the impedance of a cell made with carbon nanotube-based electrodes in which the nanotube film has a thickness of 18 μm. The impedance plot is measured at a bias of 0 V and over a frequency ranging from 1 mHz to 100 kHz. In Fig. 6.8, the high frequency intersect with the real axis is the sum of the resistances of the electrodes and the electrolyte in the separator. The resistance of the electrodes includes both the resistance of the carbon nanotube active layer and the resistance of the charge collector. The high frequency region in the spectrum is represented by an incomplete semicircle. This semicircle is due to a resistive layer which we believe is constituted by a thin non continuous layer of aluminum oxide between the tungsten charge collector and the carbon nanotube active layer, as shown in Fig. 6.8. This oxide layer introduces a resistance (due to the resistive path constituted by the oxide) in parallel with a capacitance (introduced by the oxide separating the aluminum from the nanotubes).

The next region of the plot is a line approaching a slope of 45°. For non-faradaic based ultracapacitors, this 45° line is due to the dynamics of ion transport in the pores. The third region can be linked to capacitive behavior and to the quasi-static behavior of the electrode. This region should ideally be vertical (perfect capacitive behavior) or slightly tilted (in the case of a leakage current).

6.3.2   Equivalent Circuit Model of the CNT Cell

The impedance spectrum of a carbon nanotube-based electrode cell can be simulated in the frequency range from 100 kHz to 10 mHz using the equivalent circuit model shown in Fig. 6.9. This models only uses two time constants to model the impedance spectrum. One time constant models the semi circle caused by the oxide layer and one time constant models the quasi static region of the double layer capacitor. The model does not include the two time constants that model the dynamic region of the double layer capacitor, as the activated carbon model does. This is because in the nanotube electrode measured this region is small due to the short length and low density of the nanotubes. The values of the parameters are determined by providing the impedance spectrum as an input to the software ZWiew from ScribnerAssociates, Inc. Different groups of parameters account for the different regions of the impedance spectrum and the particular structure of the model is chosen to explicitly link the regions of the impedance introduced in section 6.3.1 with the circuit parameters. The circuit element values are obtained by analyzing experimental data. The R_S is given by the intersection of the impedance with the real axis. The capacitance and resistance of the oxide layer are determined from the impedance spectrum. The resistance R_{OX} is given by the diameter of the high frequency impedance semicircle. The capacitance of the oxide layer has to satisfy the condition $1/(R_{OX} \cdot C_{OX}) = 2\pi f_{OX}$.

The high frequency semicircle is modeled by the parallel connection of the resistor R_{OX} and capacitor C_{OX}, which are in series with the equivalent series resistance R_S. From the value of C_{OX} the average thickness of the resistive aluminum oxide layer between the carbon

nanotube active layer and tungsten charge collector can be computed using

$$2 \cdot C_{OX} = \frac{\varepsilon_{OX} \cdot A}{t_{OX}} \tag{6.9}$$

for this cell $A = 1$ cm^2 and $\varepsilon_{OX} = 7.7 \cdot 10^{-13}$, yielding an average aluminum oxide thickness, t_{OX}, of 1.3 Å. We believe that the oxide layer thickness has to be considered as an average since some areas of the electrode present a thicker oxide layer and same other areas present a thinner oxide layer. Each electrode has an oxide capacitance that is twice the oxide capacitance of the cell, C_{OX}, and thus the factor of 2. The resistance R_{OX} of the oxide layer between the nanotubes and the charge collector is 0.59 Ω for the cell and thus $2 \cdot R_{OX}$ for each electrode. The capacitive behavior of the double layer is modeled by the parallel
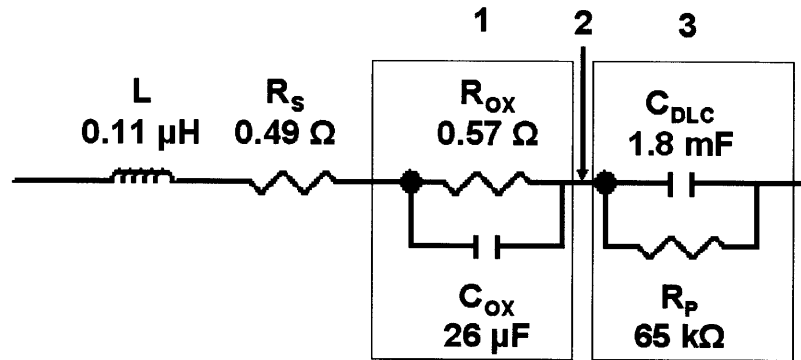
Figure 6.9: Equivalent circuit modeling the impedance spectrum of a cell assembled using 18 μm thick nanotube electrodes. The fit between the measured and the modeled impedance spectrums is shown in Fig. 6.10.

connection of the capacitor C_{DLC} and the parallel resistor, R_P. The parallel resistor R_P is responsible for the leakage current, which we believe is due to a faradaic reaction between the electrolyte and the stainless steel package of the cell. The capacitor C_{DLC} models

the double layer capacitor that forms at the interface between the electrolyte and each electrode active layer. This is the element accountable for the energy stored in the cell, and its value can be calculated using (6.10) and (6.11) with the parameters in Table 6.2 using the geometrical capacitance model proposed in section 3.3.

$$A_{DLC} = \rho \cdot \pi d t_C = 0.18 \text{ m}^2 \tag{6.10}$$

$$C_{DLC} = A_{DLC} \cdot C_D = 1.8 \text{ mF} \tag{6.11}$$

As shown in section 5.23, the calculated double layer capacitance matches the capacitance

	$t_C = l$ μm	d nm	D nm	r_{eq} nm	C_D μF/cm^2	k mS/cm	k_{eff} mS/cm	ε
Cell A	18	6.5	47	17	10	60	58	0.98
Cell B	33	6.5	47	17	10	60	58	0.98

Table 6.2: Morphological parameters of the two types of electrodes measured.

measured for the electrode. L is the parasitic inductance of the cell. Figure 6.10 shows the impedance spectrum for the cell simulated by the circuit in Fig. 6.10. The measured data is represented by the red curve and the simulated green curve is generated by the equivalent circuit model at a bias of 0 V for frequencies ranging from 10 mHz to 100 kHz.

The electrodes used for this cell present a thin nanotube film (18 μm) and a low density of the nanotubes leading to a dynamic region in which the $-45°$ phase angle does not extend over a wide frequency range. Therefore, the equivalent circuit used to simulate the measured impedance spectrum does not need to include an additional time constant to simulate the
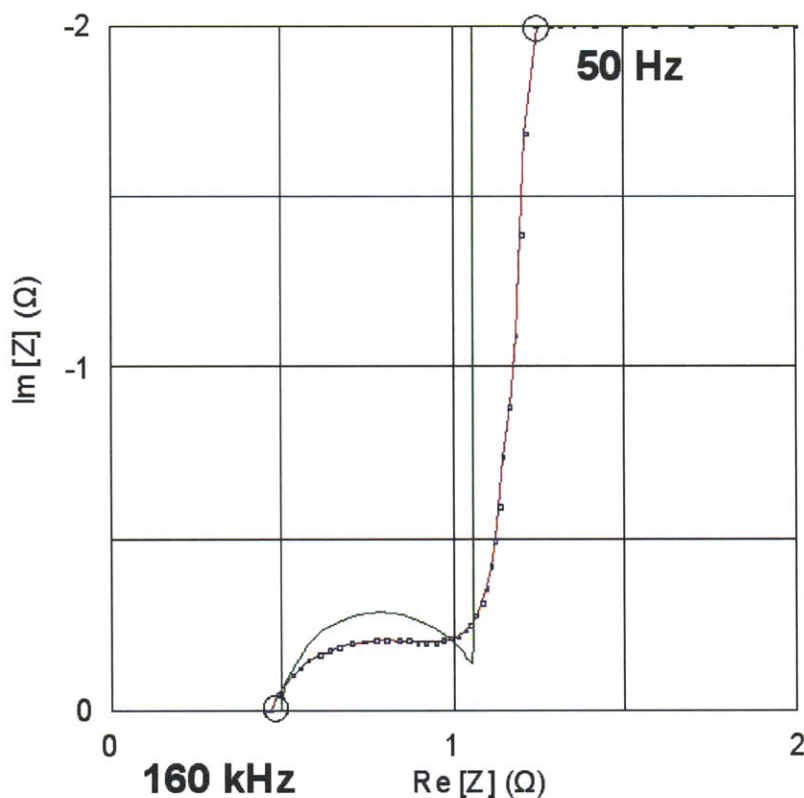
Figure 6.10: Impedance spectrum showing the fit between the measured curve (red) and the simulated curve (green) generated by the model in Fig. 6.10 between the frequencies of 60 Hz and 100 kHz.

dynamic region. If the $-45°$ region did extend over a wider frequency range, as for the case of the activated carbon electrode shown in Fig. 6.5, the equivalent circuit modeling the impedance spectrum would need to include additional time constants to represent the dynamic region. Figure 6.12 shows an example of an equivalent circuit in which in addition to the series resistance (R_S) to the oxide components (R_{OX} and C_{OX}) there are two time constants, $\tau_1 = (R_S + R_{OX}) \cdot C_1$ and $\tau_2 = (R_S + R_{OX} + R_2) \cdot C_2$, that represent the dynamic region. The time constant $\tau_3 = (R_S + R_{OX} + R_2 + R_3) \cdot C_3$ is then representative of the quasi-static region ideally approaching a $-45°$ slope.
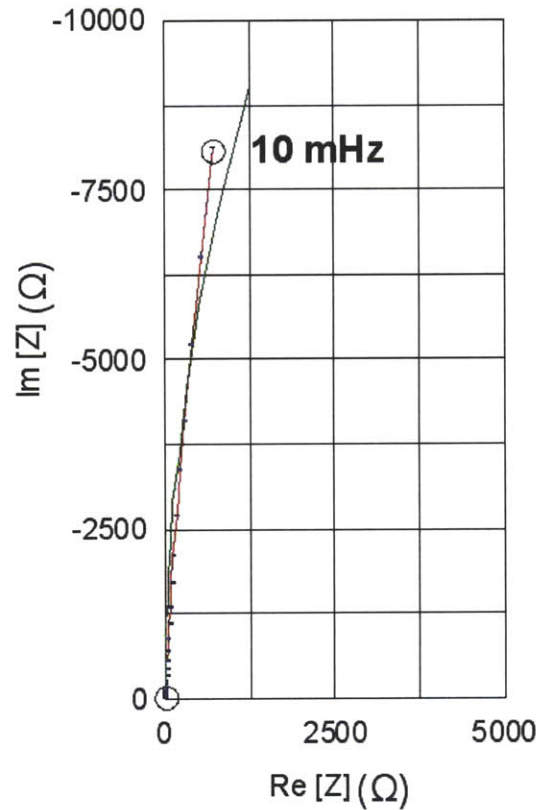
Figure 6.11: Impedance spectrum showing the fit between the measured curve (red line) and the simulated curve (green line) generated by the model in Fig. 6.10 zooming in the low frequency range down to 10 mHz.

6.3.3   Analysis of the Dynamic Region of CNT DLC Behavior

Important observations can be made about the frequency $\overline{f}$ at which the impedance behavior as a function of frequency transitions from dynamic to quasi-static. The modeling of this region can in fact lead to predictions of the cell time constant, power density, and efficiency. The shape of the impedance spectrum in the dynamic region is characterized by a 45° line, which is modeled by the distributed resistance and capacitance of the electrolyte within the pores. The Keiser model described in section 6.1.2 predicts that the transition from
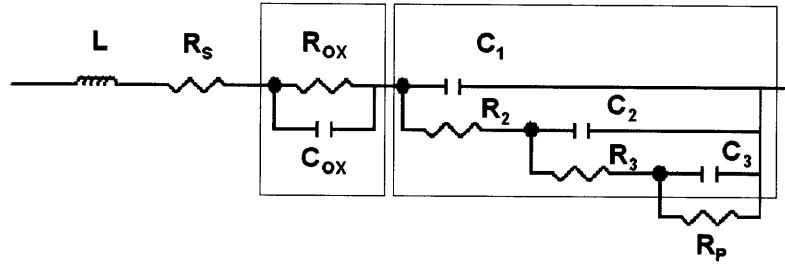
Figure 6.12: Equivalent circuit modeling the impedance spectrum of carbon nanotube electrodes based cells in which the dynamic region of the impedance is present.

dynamic to quasi-static behavior takes place at approximately $l/\lambda = 3$ where $l = t_C$ is the length of the pore and λ is a normalization variable, given by (6.12), which is a function of the electrolyte and electrode parameters as well as frequency. In order to encompass the case of nanotube electrodes, we extend the cylindrical pore model and idealize the volume between nanotubes as the volume of an equivalent cylindrical pore. In the case of nanotube electrodes, the pores are characterized by the spacing between nanotubes, as shown in Fig. 6.13. The area A_P defines the equivalent opening area of the cylindrical pore used to model the spacing between nanotubes. In 6.12 the radius used for the equivalent cylindrical pore between nanotubes is given by $r_{eq} = \sqrt{A_P/\pi}$ and

$$\lambda = \sqrt{\frac{r_{eq}k_{eff}}{8\pi f C_D}} \qquad (6.12)$$

The triangular area defined by three nanotubes, which are here idealized by straight pillars that have a spacing D_C and a diameter d_C, is

$$A_P = \frac{\sqrt{3}}{4}D_C^2 - \frac{\pi}{4}d_C^2 \qquad (6.13)$$
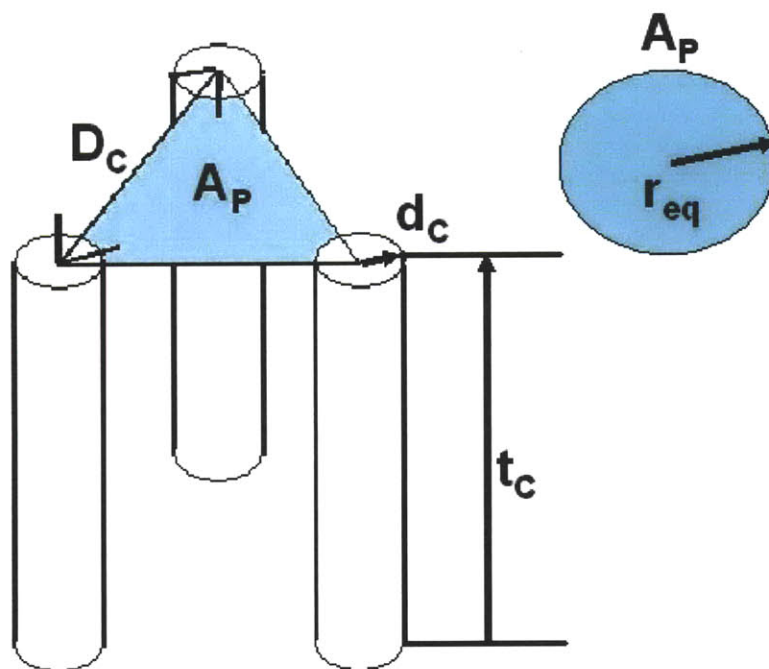
Figure 6.13: Modeling of the equivalent radius of the pore defined by the space in between adjacent nanotubes.

The parameter k_{eff} is the electrolyte conductivity within the spaces between nanotubes. As discussed by [21] the effective electrolyte conductivity, k_{eff}, within an electrode is given by

$$k_{eff} = k \cdot \varepsilon^x \tag{6.14}$$

where k is the bulk conductivity, ε is the ratio of void volume to electrode volume, and x is an exponent ranging from 1 to 1.8 taking into account the degree of electrode torturousity, which depends on the shape of the electrode particles. In the case of idealized straight nanotubes, this exponent should be 1 since the tubes provide longitudinal continuous pathways to the migration of the electrolyte solvated ions. The void ratio, as discussed in section 3.3,

is given by $\varepsilon = 1 - \pi/4(\frac{d_C}{D_C})^2$.

6.4 Performance Prediction

In this section we propose a procedure to predict the impedance spectrum of a cell based on

symmetric carbon nanotube electrodes given their electrode structural parameters and the

model described in section 6.3.3. From the predicted cell impedance spectrum, important

parameters such as the cell time constant[4], or the cell bandwidth[5] are estimated. Table 6.3

shows the assumed structural parameters for three electrode examples, and for each case

the transition frequency $\bar{f}$ at which $l/\lambda = 3$ is calculated. For each electrode in Table 6.3

	t_C μm	d_C nm	D_C nm	r_{eq} nm	C_D μF/cm^2	k mS/cm	k_{eff} mS/cm	ε	ρ_C cm^{-2}
Target 1	150	6.5	10	2.9	30	60	40	0.67	10^{12}
Target 2	150	6.5	10	2.9	50	60	40	0.67	10^{12}
Target 3	100	6.5	10	2.9	50	60	40	0.67	10^{12}

Table 6.3: Description of the morphological parameters for the three examples of electrodes.

the impedance spectrum can be calculated according to the procedure that follows in this

section. Figure 6.14 shows the impedance spectrum extrapolated for a cell made with

electrodes having the structure described as Target 2. The resistances and reactances used

to construct the impedance spectrum shown by Fig. 6.14 are summarized in Table 6.4.

---

[4]The cell time constant is indicative of the charge and discharge time of the cell. Shorter time constants lead to faster charge and recharge ability.

[5]The cell bandwidth is indicative of the frequency, f_{3dB}, at which the impedance phase angle is $-45°$, thus limiting the usable frequency range of the device to frequencies $f < f_{3dB}$.
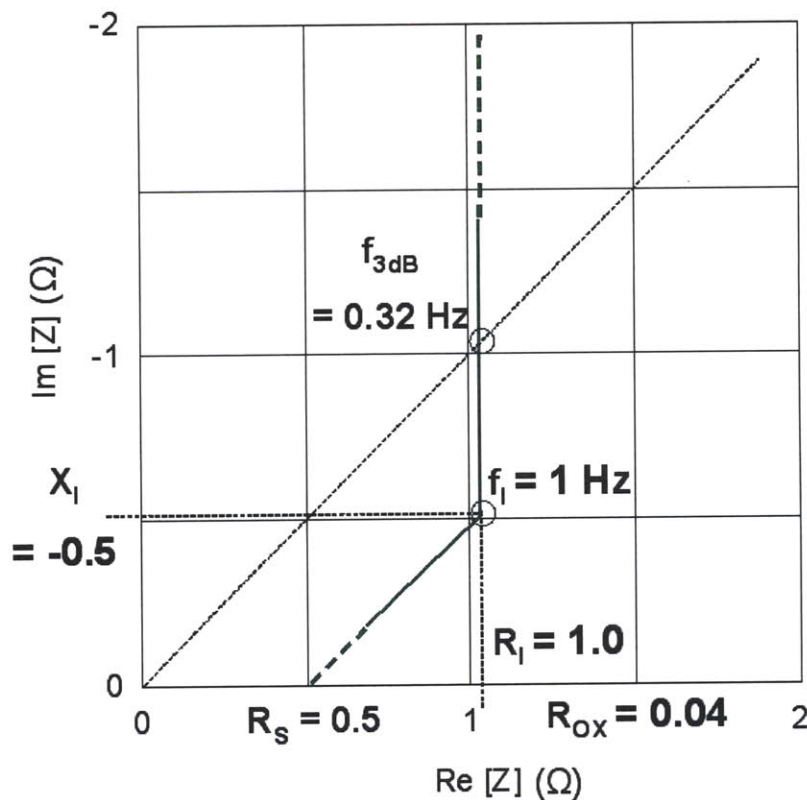
Figure 6.14: Calculated impedance spectrum of a cell made with nanotubes having the dimensions described by "Target 2" in Table 6.3. The intersection between the dotted line (which has a slope of 45°) and the impedance identifies the 3 dB attenuation point of the impedance and its frequency.

6.4.1 Determination of the Oxide Layer Influence

As discussed previously the oxide layer is constituted by a non continuous layer of aluminum oxide between the carbon nanotubes and the electrode charge collector. This oxide layer introduces the cell components R_{OX} and C_{OX}. We predict that increasing the density of carbon nanotubes will linearly reduce the oxide resistance and linearly increase the oxide capacitance. The resistance reduction is due to the fact that a greater density of carbon nanotubes results in more parallel paths for the current flow from the nanotubes through the

	f_I Hz	$\bar{f}$ Hz	C_{DLC} F	C_{OX} F	R_S Ω	R_{OX} Ω	X_I Ω	R_I Ω	τ s	E_V Wh/l
Target 1	0.47	0.85	0.459	30	0.5	0.04	0.74	1.24	0.41	18
Target 2	0.28	0.5	0.766	30	0.5	0.04	0.74	1.24	0.69	30
Target 3	0.63	1.15	0.51	30	0.5	0.04	0.49	0.99	0.39	27

Table 6.4: Description of the impedance parameters for the electrodes in Table 6.3.

oxide layer to the charge collector. Similarly, the linear increase in capacitance with the nanotube density is due to the increased parallel capacitive connections between the nanotubes and the charge collector. The oxide resistance and capacitance parameters $R_{OX} = 0.57$ Ω and $C_{OX} = 26$ μF are for electrodes having a nanotube density of $7 \cdot 10^{10}$ cm^{-2}. Thus extrapolating these parameters to electrodes having a nanotube density of 10^{12} cm^{-2} results in a $R_{OX} = 0.04$ Ω and $C_{OX} = 371$ μF. This reduces the size of the high frequency semicircle in the Nyquist plot of Fig. 6.8. In this case in fact the resistance introduced by the semicircle is only $R_{OX} = 0.04$ Ω and thus is much smaller than the equivalent series resistance.

The main observation that enables the calculation of the impedance spectrum is that independent of the electrode structure, when the quasi-static and dynamic curves are extended with straight lines, they intersect at $l/\lambda = 2.6$. as shown in section 6.2.1 for the case of activated carbon. From this condition one can compute the frequency f_I at which the intersection takes place using

$$f_I = \frac{r_{eq}k_{eff}}{8\pi \cdot 2.6^2 C_D} \tag{6.15}$$

At the frequency f_I the reactance introduced by the quasi-static region, $X_{DLC} = 1/(2\pi f_I C_{DLC})$,

equals the reactance introduced by the dynamic region X_I and thus $X_I = X_{DLC} = 1/(2\pi f_I C_{DLC})$. Since the dynamic region is a 45° sloped line, the resistance that it introduces equals the reactance that it introduces and thus $R_{dyn} = X_I = X_{DLC} = 1/(2\pi f_I C_{DLC})$.

Ultimately, the resistance corresponding to the intersection between the dynamic and the quasi static region is given by

$$R_I = R_S + R_{OX} + R_{dyn} \tag{6.16}$$

From the resistance R_I the time constant of the cell can be calculated as $\tau = R_I \cdot C_{DLC}$. Moreover, under the assumption that $R_I \cong R_{3dB} = X_{3dB}$ the cell bandwidth can be calculated as

$$f_{3dB} = \frac{1}{2\pi R_I \cdot C_{DLC}} \tag{6.17}$$

6.5 Power Density, Energy Density and Efficiency Extrapolation

This section predicts the power density, efficiency, and energy density achievable for a cell packaged with our carbon nanotube electrodes. The section starts by describing how to correlate frequency response data regarding a 1 cm^2 cell to frequency response data regarding a packaged cell. Thereafter, the analysis is performed to predict the frequency response of carbon nanotube electrode based cells and that is used to estimate the efficiency and the power performance of the cell. The same analysis is performed for an activated

carbon electrode D-size cell as well and the power performance of the two type of cells are compared.

6.5.1 Power Density and Efficiency for a Carbon Nanotube based D-size Cell

Assuming the use of carbon nanotube electrodes having the specifications for Target 3 described in Table 6.3 and in Table 6.4, in which the nanotube density is 10^{12} cm^{-2}, Fig. 6.15 presents the sizes of the solid components necessary for each centimeter square of electrode cell. As Fig. 6.15 shows, a 1 cm^2 cell involves two 100 μm thick active layers one 25 μm
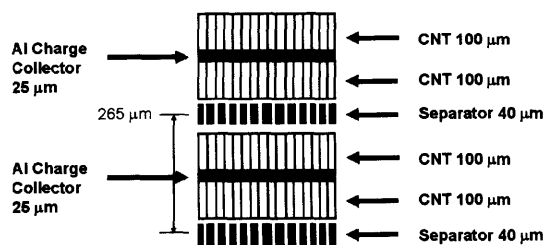
Figure 6.15: 1 cm^2 stack of a nanotube electrode that presents active layers on both sides of the charge collector and separators.

thick aluminum charge collector, and one 40 μm thick separator. All these components have a 1 cm^2 Euclidean area. The overall thickness of this stack is 265 μm and its overall volume (V_{ST}) is 0.0265 cm^3.

A D-size cell has a diameter of 32.5 mm and a body length of 65 mm and thus a volume V_D of 53.8 cm^3. By assuming a packaging volume which is 20 % of the total cell volume, the inner cell volume (V_{IC}) is 80 % of the total cell volume, that is, 43.1 cm^3. The equivalent

number of stacks, N_{ST}, rolled into a D-size cell is therefore

$$N_{ST} = V_{IC}/V_{ST} = 1625 \tag{6.18}$$

The number of stacks contained in a cell is the number of parallel 1 cm^2 capacitors inside the cell. Given the capacitance C_{DLC}, and resistances R_S and R_{3dB} of a 1 cm^2 cell, the overall packaged cell capacitance $C_{(D)}$, and resistances $R_{S(D)}$ and $R_{3dB(D)}$ are given by

$$C_{(D)} = C_{DLC} \cdot N_{ST} = 830 \text{ F} \tag{6.19}$$

$$R_{S(D)} = \frac{R_S}{N_{ST}} \cdot 1.2 = 0.369 \text{ m}\Omega \tag{6.20}$$

$$R_{3dB(D)} = \frac{R_{3dB}}{N_{ST}} \cdot 1.2 = 0.735 \text{ m}\Omega \tag{6.21}$$

The factor of 1.2 used in the calculation of the resistances takes into account the added resistance due to contacts and connections within the cell, similar to the case of a cell packaged with activated carbon electrodes.

With the cell resistances, volume, and capacitance the overall performance of the D size cell can be predicted. Given the target rated voltage of 3.5 V, the volumetric energy density of the cell is

$$E_{V(D)} = \frac{C_{(D)} \cdot V_M^2}{2 \cdot 3.6 V_D} = 26 \text{ Wh/l} \tag{6.22}$$

where 3.6 is the conversion factor from kJ to Wh. The maximum peak volumetric power

that can be extracted from the D-size cell is given by

$$P_{V(D)} = \frac{V_M^2}{4 \cdot R_S \cdot V_D} = 154 \text{ kW/l} \tag{6.23}$$

The resulting peak power is 154 kW/l, compared to ac cell of 10 kW/l.

An important parameter for applications is the average power density and round trip efficiency for different constant charging and discharging currents. $R_{3dB(D)}$ is the cell low frequency resistance associated with the capacitive (quasi-static) cell behavior calculated using (6.21), I is the charging and discharging constant currents, P_V^J and P_V^{AVG} are, respectively, the volumetric power dissipation associated with the constant current operation, and the average volumetric delivered power density. The volumetric average power is calculated for charging the device from 0 V up to $V_M = 3.5$ V and by using a constant charging current.

$$P_V^J = \frac{R_{3dB(D)} \cdot I^2}{V_D} \tag{6.24}$$

$$P_V^{AVG} = \frac{V_M \cdot I}{2 \cdot V_D} \tag{6.25}$$

V_M is the maximum rated potential, η_{RTE} is the round trip efficiency, which is approximated by,

$$\eta_{RTE} = [\frac{(P_V^{AVG} - P_V^J)}{P_V^{AVG}}]^2 \tag{6.26}$$

and t is the time required to fully charge the device,

$$t = \frac{C_{(D)} \cdot V_M}{I} \tag{6.27}$$

For the calculation of t, the cell capacitance is assumed to be constant over the voltage range.

6.5.2   Power Density and Efficiency for an Activated Carbon D-Size Cell

Figures 6.16 and 6.17 show the measured frequency response at a bias of 0 V (represented by a Nyquist and Bode plots) of a D-size cell[6] packaged with the activated carbon electrodes presented in section 5.2. Figure 6.16 shows that the cell resistance at the 3 dB frequency point $R_{3dB(D)}$ is approximately equal to the cell resistance at the transition frequency $R_{I(D)}$ and is $R_{3dB(D)} \sim R_{I(D)} = 3$ mΩ. The high frequency equivalent series resistance is $R_{S(D)} = 1.7$ mΩ. The cell rated capacitance and voltage are 350 F and 2.5 V and the cell volume is $V_D = 51$ cm^3.

From these data the cell volumetric energy density, power density and efficiency at different charging currents can be calculated as for the case of the carbon nanotube electrodes. The peak power that can be extracted from the activated carbon cell is approximately 10 kW/l, which is ten times lower than that projected for a cell packaged with nanotube electrodes.

---

[6]The D-size cell is a Boostcap manufactured by Maxwell Technologies® P/N: BCAP0350 E01.
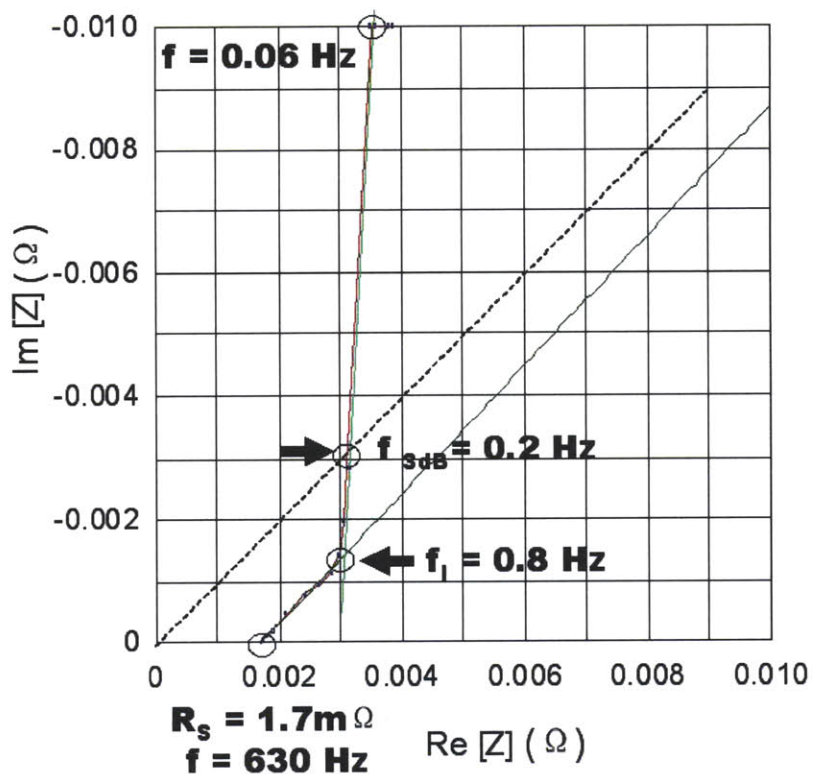
Figure 6.16: D-size cell frequency response spectrum at a bias of 0 V represented with a Nyquist plot. The intersection between the dotted line (which has a slope of 45°) and the impedance identifies the 3 dB attenuation point of the impedance and its frequency.

6.5.3   Power Density Comparison Between an Activated Carbon and a Nanotube D-Size Cell

Tables 6.5 and 6.6 list the cell resistance at the 3 dB point, the charging and discharging currents, the average power density and efficiency for a D-size cell packaged with Target 3 nanotube electrodes and activated carbon electrodes, respectively.

For the same round trip efficiency a cell packaged with nanotube electrodes shows approximately 2 to 5 times higher charging and discharging currents as well as 4 to 7 times higher
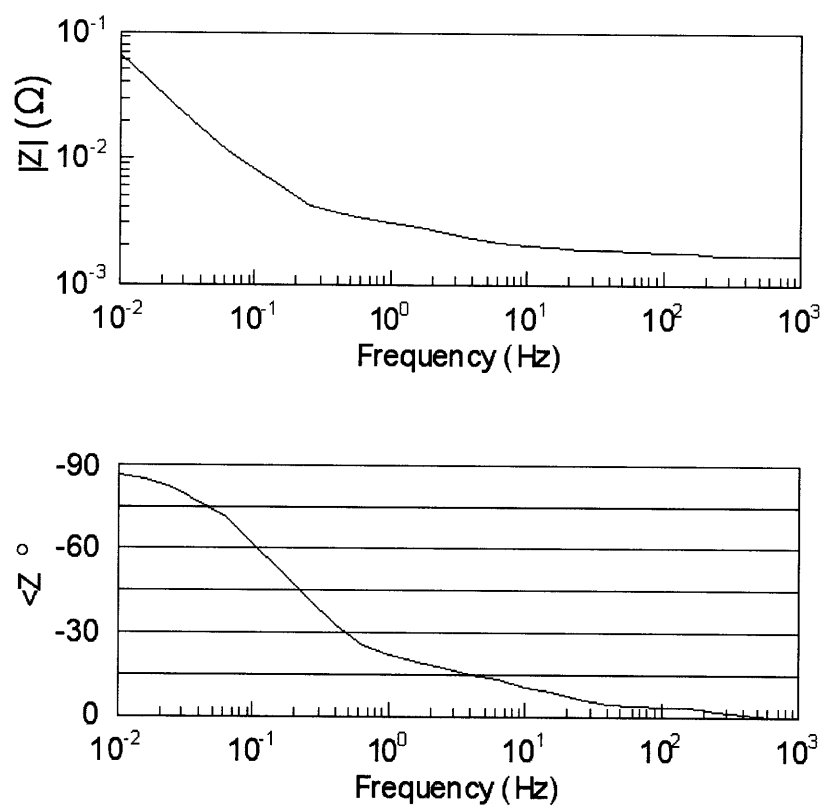
Figure 6.17: D-size cell frequency response spectrum at a bias of 0 V represented with a Bode plot.

power capability.

$R_{3dB(D)}$ mΩ	I A	P_V^J W/l	P_V^{AVG} kW/l	V_M V	η_{RTE} %	t s	E_V Wh/l
0.735	40	22	1.3	3.5	97	73	26.2
0.735	60	49	2.0	3.5	95	49	26.2
0.735	120	197	3.9	3.5	90	24	26.2
0.735	240	786	7.8	3.5	80	12	26.2

Table 6.5: Power density and round trip efficiency at constant charging and discharging current.

$R_{3dB(D)}$ mΩ	I A	P_V^J W/l	P_V^{AVG} kW/l	V_M V	η_{RTE} %	t s	E_V Wh/l
3	15	13	0.363	2.5	97	29	5.9
3	20	23	0.484	2.5	95	22	5.9
3	25	36	0.605	2.5	90	17	5.9
3	45	118	1.088	2.5	80	9.7	5.9

Table 6.6: Power density and round trip efficiency at constant charging and discharging current.

6.6 Chapter Summary

This chapter reviews the modellings developed by de Levie and Kaiser to predict the response of porous materials in electrolytic solutions to a sinusoidal excitation. The chapter discusses our extension to these modelling to analyze the case of vertical carbon nanotube electrodes. In this chapter we show the equivalent circuit models that we created to model the impedance spectrum of carbon nanotube and activated carbon-based electrodes. We show the link between the equivalent circuit parameter values and physical processes that take place within the cell. Finally, we show a procedure to predict the power density of a D-size cell from the impedance spectrum of a 1 cm^2 cell for activated carbon and nanotube. Our prediction shows that a D-size cell packaged with carbon nanotube-based electrodes could achieve a power density four to seven times higher than that of an activated carbon-based cell. The next chapter reviews the major contributions of this research and discusses the work that remains to be done to achieve our target performance.

Recommendations and future Research

This thesis shows how the carbon nanotube-based double layer capacitor electrodes that we designed might lead to significant improvements over activated carbon electrodes. A nanotube-based ultracapacitor might achieve energy densities up to seven times higher than an ultracapacitor packaged with today's activated carbon electrodes. Our analysis also shows that our nanotube-based ultracapacitor might lead to power densities which are four to seven times higher than that of activated carbon devices.

In this concluding chapter we summarize the advancement in the understanding of nanotube-based ultracapacitor that our research has made possible, along with the progress in the device fabrication. Finally, we present our future milestones toward the development of these high energy and power density ultracapacitors.

7.1 Contributions of this Research

This thesis has enabled us to make contributions to the fabrication of carbon nanotube electrodes and to the development and understanding of carbon nanotube-based double

layer capacitors. With respect to the fabrication of carbon nanotube electrodes to be used with double layer capacitors:

- We designed and built a low pressure chemical vapor deposition system to fabricate vertical carbon nanotube electrodes on thin conducting substrates of tungsten and aluminum.

- We defined and validated a process that yields the growth of vertical carbon nanotubes on thin conducting substrates of tungsten and aluminum. The resulting nanotubes within the active layers have a length and a diameter that meet our target. In addition, our process currently yield vertical nanotubes having a density of approximately $3 \cdot 10^{11}$ cm^{-2}, which is ten times higher than our initial results, but still three times lower than our target nanotube density.

With respect to enhancement of the understanding and to the development of carbon nanotube-based ultracapacitors:

- We adopted the Gouy-Chapman-Stern theory to analyze the double layer structure of carbon nanotube electrodes and we predicted a differential capacitance that is close to the measured one.

- We designed a carbon nonotube electrode structure that might achieve up to five to seven times higher energy density than that of a devices packaged with conventional activated carbon electrodes.

- We developed a model, which from geometrical consideration of the nanotube surface, predicts the capacitance and thus the energy density of carbon nanotube electrode based

devices. This model optimizes the device energy density with respect to morphological electrode features given currently available electrolyte molarities.

• We extended the frequency response modeling for porous electrodes to the case of carbon nanotube electrodes. From this new modeling we predict the frequency response of vertical carbon nanotube electrodes of a given morphology. From the frequency response of vertical carbon nanotube electrodes we can predict the power density of a packaged ultracapacitor using such electrodes. We experimentally validated these prediction for an activated carbon-based cell.

• Our electrochemical measurements demonstrate the validity of our capacitance and frequency response modelling based on the structure of our vertical nanotube electrodes.

7.2   Future Investigations and Development

The research that we led on this topic raised interesting questions that still need to be answered to further enhance our understanding of the behavior of carbon nanotube as double layer capacitor electrodes.

• First, the model that we developed idealizes nanotubes as straight and free of amorphous carbon. A refinement of this model could be to consider the amorphous carbon content and the presence of defects in the nanotube surface. Also, the effects of nanotube bundling could be studied. This could lead to refinement in the understanding of the double layer effect and thus of the differential capacitance of non-ideal nanotube

electrodes. Moreover, this could lead to a refinement in the already-good capacitance modeling of nanotube electrodes.

- During this research we successfully fabricated vertical nanotube electrodes on conductive tungsten and aluminum films. We are especially pleased with our success with aluminum. The relatively low cost of this material and the wide familiarity of the existing capacitor industry with this material both suggest relatively easy industrial acceptance. Nevertheless, more substrate materials could be considered leading to a spectrum of options for a variety of applications.

- The electrolyte that we used so far for the electrode measurement was acetonitrile. We intend to explore the use of ionic liquids to develop ultracapacitors that can operate at higher voltage.

- Currently, the superficial density of nanotubes in the electrodes is still lower than our target by a factor of three and part of our future endeavor will be to improve the electrode density.

- Similarly, the differential capacitance of our electrodes is lower than our target, which was based on differential capacitance previously achieved by An [5]. We will investigate suitable surface treatment processes to achieve that value of differential capacitance with our electrodes.

References

[1] S. Braunauer, P. H. Emmett, and E. Teller. Gas adsorption in multimolecular layers. *Journal of the American Chemical Society*, 60(2):309–319, November 21, 1996.

[2] K. Ikeda, K. Hiratsuka, K. Sotoh, and M. Noguchi. Material development of electric double layer capacitor for fuel cell electric vehicle and the newly developed electric double layer capacitor cell. In *The 13th International Seminar on Double Layer Capacitors and Hybrid Energy Storage Devices*, pages 189–202, Deerfield Beach, Florida, Decemer 8, 2003.

[3] M. Okamura and H. Nakamura. Ecass - 2: Capacitor improvements and discussion. In *The 13th International Seminar on Double Layer Capacitors and Hybrid Energy Storage Devices*, pages 215–225, Deerfield Beach, Florida, December 8, 2003.

[4] C. Niu, E.K. Sichel, R. Hoch, D. Moy, and H. Tennent. High power electrochemical capacitors based on carbon nanotube electtrodes. *Applied Physics Letters*, 70(11):1480–1482, November 21, 1996.

[5] K.H. An, W.S. Kim, Y.S. Park, J.M. Moon, D.J. Bae, S.C. Lim, Y.S. Lee, and Y.H. Lee.

Electrochemical properties of high-power supercapacitors using single-walled carbon nanotube electrodes. *Advanced Functional Materials*, 11(5):387–392, October 2001.

[6] B.J. Yoon, S.H. Jeong, K.H. Lee, H.S.Kim, C.G. Park, and J.H. Han. Electrical properties of electrical double layer capacitors with integrated carbon nanotube electrodes. *Chemical Physics Letter*, 388:170174, March 2004.

[7] C. Du, J. Yeh, and N. Pan. High power density supercapacitors using locally aligned carbon nanotube electrodes. *Nanotechnology*, 16:350353, February 2005.

[8] A. Kumar, V. Pushparaj, S. Kar, O. Nalamasu, P. Ajayan, and R. Baskarana. Contact transfer of aligned carbon nanotube arrays onto conducting substrates. *Applied Physics Letters*, 89:163120, August 2006.

[9] D. Futaba, K. Hata, T. Yamada, T. Hiraoka, Y. Hayamizu, Y. Kakudate, O. Tanaike, H. Hatori, M. Yumura, and S. Iijima. Shape-engineerable and highly densely packed single-walled carbon nanotubes and their application as super-capacitor electrodes. *Nature Materials*, 5:987–994, Decemer, 2006.

[10] K. Tamamitsu, S. Suematsu, K. Machida, and H. Hatori. Recent progress in development of cnt capacitor. In *The 18th International Seminar on Double Layer Capacitors and Hybrid Energy Storage Devices*, pages 113–123, Deerfield Beach, Florida, December 8, 2008.

[11] Allen J. Bard and Lerry R. Faulkner. *Electrochemical Methods: Fundamentals and Applications*. Wiley and Sons, 2001.

[12] H. von Helmholtz. Uber einige gesetze der vertheilung elektrischer strome in korper-
lichen leitern mit anwendung auf die thierish-elektrischen versuche. *Anneal Physik und
Chemie*, 89:211–233, 1853.

[13] G. Gouy. Sur la constitution de la charge electrique a la surface dun electrolyte. *Le
Journal de Physique et le Radium*, 9:457–468, 1910.

[14] D. Chapman. A contribution to the theory of electrocapillarity. *Philosophical Magazine*,
25:475–481, 1913.

[15] O. Stern. The theory of the electrolytic double layer. *Zeitschrift fur Elektrochemie*,
30:508–516, 1924.

[16] M.L. Colaianni, P.J. Chen, and Jr. J.T. Yates. Spectroscopic studies of the thermal
modification of the Fe/Al_2O_3 interface. *Surface Science*, 238:13–24, June, 1990.

[17] L.C. van Laake, A.J. Hart, and A.H. Slocum. A suspended heated silicon platform
for rapid thermal control of surface reactions with application to carbon nanotube
synthesis. *Review of Scientific Instruments*, 78:083901, August, 2007.

[18] R. de Levie. On porous electrodes in electrolyte solutions. *Electrochimica Acta*, 8:751–
780, 1963.

[19] H. Keiser, K. Beccu, and D. Gutjahr. Abschätzung der porenstruktur poröser elektro-
den aus impedanzmessungen. *Electrochimica Acta*, 21:539–543, 1976.

[20] Brian E. Conway. *Electrochemical Supercapacitors: Scientific Fundamentals and Tech-
nological Applications*. Kluwer Acadeemic/Plenum Publisher, 1999.

[21] J. Desilvestro, P.K. Kantilal, and J.M. Paulsen. Numerical simulation of porous networks in relation to battery electrodes and separators. *Journal of Power Sources*, 122:144–152, 2003.